Fermilab

FERMILAB-THESIS-1994-36

LBL–xxxxx

A Measurement of the Mass of the B_s^0 Meson in Proton–Antiproton Collisions at $\sqrt{s} = 1.8$ TeV

William Carl Wester, III
Ph.D. Thesis

Department of Physics
University of California, Berkeley, CA 94720
and
Lawrence Berkeley Laboratory
University of California, Berkeley, CA 94720

April 28, 1994

Abstract

The large b quark production cross section at the Fermilab Tevatron and the capabilities of the CDF experiment during the 1992–1993 $\overline{p}p$ collider running are exploited to fully recontructed B mesons and measure their masses. Signals of 139.9 ± 15.0 $B^- \to J/\psi\ K^-$ candidates, 56.5 ± 9.5 $B^0 \to J/\psi\ K^*$ candidates, and 32.9 ± 6.8 $B_s^0 \to J/\psi\ \phi$ candidates are used to measure the masses:

- $\mathrm{M}(B^-) = 5279.6 \pm 1.7\ (\mathrm{stat}) \pm 2.9\ (\mathrm{syst})\ \mathrm{MeV}/c^2$
- $\mathrm{M}(B^0) = 5279.9 \pm 2.5\ (\mathrm{stat}) \pm 3.7\ (\mathrm{syst})\ \mathrm{MeV}/c^2$
- $\mathrm{M}(B_s^0) = 5367.7 \pm 2.4\ (\mathrm{stat}) \pm 4.8\ (\mathrm{syst})\ \mathrm{MeV}/c^2$

This work was supported by the Director, Office of Energy Research, Office of High Energy and Nuclear Physics, Division of High Energy Physics, of the U.S. Department of Energy under contract DE-AC03-76SF00098.

A Measurement of the Mass of the B_s^0 Meson in Proton–Antiproton Collisions at $\sqrt{s} = 1.8$ TeV

Copyright © 1994

William Carl Wester, III

The United States Department of Energy has the right to use this thesis for any purpose whatsoever including the right to reproduce all or any part thereof.

Dedicated to my son Stephen

Acknowledgements

I would like to thank so many people who have helped me during my tenure as a graduate student. I have been very fortunate to have worked with so many talented and dedicated people. In the early days working on the readout electronics for the SVX, I received *in-the-trenches* help from Bob E., Olivier S., Stuart K., Tom M., Kaz, and Garth S. My primary responsibility, the port card, was built with the quality work of technicians at Promex: Jennifer, Randy, Kim, Kimmie, Glenn, and Phansu. Circuit boards built at Fermilab used the skill of Jim, Kevin, Frank, Bob, Mark, Dervin, and Steve.

I benefitted from useful discussions with many students and postdocs in the CDF Bottom Group. Special mention goes to Alan S., Hans W., Mark B., Carol A-W., Randy H., Intae Y., Jodi L., Troy D., Steve V., Chris B, Karen O., Tom L., Jonathan L., and Giorgio A. The conveners, Fritz D. and Jim M. were especially supportive.

Being a member of the Lawerence Berkeley Laboratory CDF group, I was among many of the very best particle physicists all of whom shaped me in some way. I always felt I could call on any of the senior LBL staff. The LBL postdocs especially Weiming and Young Kee helped while I was located at Fermilab.

Of course, life on the prairie would suffer from drudgery without our weekly basketball games. JJ, Brian, Les, Richard (on whom I could score at will), Vic, Randy, and Paul were some of the most *remarkable* fellow players.

The B_s^0 mass measurement became my thesis topic after an initial suggestion from Paul Tipton. Joel H. and Nigel L. helped the analysis to converge to the Physical Review Letters publication. Discussions with Aseet M. and Peter B. were particularly helpful. My analysis evolved working closely with Avi Yagil who kept the focus on the important aspects of the analysis. I learned a great deal from Avi and I matured quite a bit as a physicist working with him. He was very generous with me in his time.

I would like to thank my committee, Joseph Cerny, Kam-Biu Luk, and Marjorie Shapiro. My advisor, Marjorie Shapiro, provided guidance in a supportive way – she allowed me to make my own decisions and nudged me back on course when necessary. Her dedication to quality work and her unselfishness has been

very inspiring.

I would like to acknowledge and thank Carl Haber whom I consider to be my mentor. We worked together three years building electronics for the SVX. More than anyone, he has taught me how to be a particle physicist. He pushed me to work hard and I am better because of his encouragement. Thank you Carl.

Finally, I can't thank my family enough for the love and support they have given me. My parents have always encouraged me to achieve in academics. My wife, Barbara, has been especially supportive when I've had to take an extended trip or when I've had to work into the late hours. My cats, Mozart and Kira, haven't complained much when "Kitty-Dad" has been gone. My infant son, Stephen, *has* complained; but I think his crying so far is pretty normal.

The CDF Collaboration

F. Abe,[13] M. Albrow,[7] D. Amidei,[16] C. Anway-Wiese,[4] G. Apollinari,[26] H. Areti,[7] P. Auchincloss,[25] F. Azfar,[21] P. Azzi,[20] N. Bacchetta,[18] W. Badgett,[16] M. W. Bailey,[24] J. Bao,[33] P. de Barbaro,[25] A. Barbaro-Galtieri,[14] V. E. Barnes,[24] B. A. Barnett,[12] P. Bartalini,[23] G. Bauer,[15] T. Baumann,[9] F. Bedeschi,[23] S. Behrends,[2] S. Belforte,[23] G. Bellettini,[23] J. Bellinger,[32] D. Benjamin,[31] J. Benlloch,[15] D. Benton,[21] A. Beretvas,[7] J. P. Berge,[7] S. Bertolucci,[8] A. Bhatti,[26] K. Biery,[11] M. Binkley,[7] F. Bird,[28] D. Bisello,[20] R. E. Blair,[1] C. Blocker,[28] A. Bodek,[25] V. Bolognesi,[23] D. Bortoletto,[24] C. Boswell,[12] T. Boulos,[14] G. Brandenburg,[9] E. Buckley-Geer,[7] H. S. Budd,[25] K. Burkett,[16] G. Busetto,[20] A. Byon-Wagner,[7] K. L. Byrum,[1] C. Campagnari,[7] M. Campbell,[16] A. Caner,[7] W. Carithers,[14] D. Carlsmith,[32] A. Castro,[20] Y. Cen,[21] F. Cervelli,[23] J. Chapman,[16] G. Chiarelli,[8] T. Chikamatsu,[30] S. Cihangir,[7] A. G. Clark,[23] M. Cobal,[23] M. Contreras,[5] J. Conway,[27] J. Cooper,[7] M. Cordelli,[8] D. P. Coupal,[28] D. Crane,[7] J. D. Cunningham,[2] T. Daniels,[15] F. DeJongh,[7] S. Delchamps,[7] S. Dell'Agnello,[23] M. Dell'Orso,[23] L. Demortier,[26] B. Denby,[7] M. Deninno,[3] P. F. Derwent,[16] T. Devlin,[27] M. Dickson,[25] S. Donati,[23] R. B. Drucker,[14] A. Dunn,[16] K. Einsweiler,[14] J. E. Elias,[7] R. Ely,[14] E. Engels, Jr.,[22] S. Eno,[5] D. Errede,[10] S. Errede,[10] A. Etchegoyen,[7a] Q. Fan,[25] B. Farhat,[15] I. Fiori,[3] B. Flaugher,[7] G. W. Foster,[7] M. Franklin,[9] M. Frautschi,[18] J. Freeman,[7] J. Friedman,[15] H. Frisch,[5] A. Fry,[28] T. A. Fuess,[28] Y. Fukui,[13] S. Funaki,[30] G. Gagliardi,[23] M. Gallinaro,[20] A. F. Garfinkel,[24] S. Geer,[7] D. W. Gerdes,[16] P. Giannetti,[23] N. Giokaris,[26] P. Giromini,[8] L. Gladney,[21] D. Glenzinski,[12] M. Gold,[18] J. Gonzalez,[21] A. Gordon,[9] A. T. Goshaw,[6] K. Goulianos,[26] H. Grassmann,[28] A. Grewal,[21] G. Grieco,[23] L. Groer,[27] C. Grosso-Pilcher,[5] C. Haber,[14] S. R. Hahn,[7] R. Hamilton,[9] R. Handler,[32] R. M. Hans,[33] K. Hara,[30] B. Harral,[21] R. M. Harris,[7] S. A. Hauger,[6] J. Hauser,[4] C. Hawk,[27] J. Heinrich,[21] D. Hennessy,[6] R. Hollebeek,[21] L. Holloway,[10] A. Hölscher,[11] S. Hong,[16] G. Houk,[21] P. Hu,[22] B. T. Huffman,[22] R. Hughes,[25] P. Hurst,[9] J. Huston,[17] J. Huth,[7] J. Hylen,[7] M. Incagli,[23] J. Incandela,[7] H. Iso,[30] H. Jensen,[7] C. P. Jessop,[9] U. Joshi,[7] R. W. Kadel,[14] E. Kajfasz,[7] T. Kamon,[29] T. Kaneko,[30] D. A. Kardelis,[10] H. Kasha,[33] Y. Kato,[19] L. Keeble,[29] R. D. Kennedy,[27] R. Kephart,[7] P. Kesten,[14] D. Kestenbaum,[9] R. M. Keup,[10] H. Keutelian,[7] F. Keyvan,[4] D. H. Kim,[7] H. S. Kim,[11] S. B. Kim,[16] S. H. Kim,[30] Y. K. Kim,[14] L. Kirsch,[2] P. Koehn,[25] K. Kondo,[30] J. Konigsberg,[9] S. Kopp,[5] K. Kordas,[11] W. Koska,[7] E. Kovacs,[7a] W Kowald,[6] M. Krasberg,[16] J. Kroll,[7] M. Kruse,[24] S. E. Kuhlmann,[1] E. Kuns,[27] A. T. Laasanen,[24] S. Lammel,[4] J. I. Lamoureux,[32] T. LeCompte,[10] S. Leone,[23] J. D. Lewis,[7] P. Limon,[7] M. Lindgren,[4] T. M. Liss,[10] N. Lockyer,[21] O. Long,[21] M. Loreti,[20] E. H. Low,[21] J. Lu,[29] D. Lucchesi,[23] C. B. Luchini,[10] P. Lukens,[7] P. Maas,[32] K. Maeshima,[7] A. Maghakian,[26] P. Maksimovic,[15] M. Mangano,[23]

J. Mansour,[17] M. Mariotti,[23] J. P. Marriner,[7] A. Martin,[10] J. A. J. Matthews,[18] R. Mattingly,[2] P. McIntyre,[29] P. Melese,[26] A. Menzione,[23] E. Meschi,[23] G. Michail,[9] S. Mikamo,[13] M. Miller,[5] T. Mimashi,[30] S. Miscetti,[8] M. Mishina,[13] H. Mitsushio,[30] S. Miyashita,[30] Y. Morita,[13] S. Moulding,[26] J. Mueller,[27] A. Mukherjee,[7] T. Muller,[4] P. Musgrave,[11] L. F. Nakae,[28] I. Nakano,[30] C. Nelson,[7] D. Neuberger,[4] C. Newman-Holmes,[7] L. Nodulman,[1] S. Ogawa,[30] S. Oh,[6] K. E. Ohl,[33] R. Oishi,[30] T. Okusawa,[19] C. Pagliarone,[23] R. Paoletti,[23] V. Papadimitriou,[7] S. Park,[7] J. Patrick,[7] G. Pauletta,[23] L. Pescara,[20] M. D. Peters,[14] T. J. Phillips,[6] G. Piacentino,[3] M. Pillai,[25] R. Plunkett,[7] L. Pondrom,[32] N. Produit,[14] J. Proudfoot,[1] F. Ptohos,[9] G. Punzi,[23] K. Ragan,[11] F. Rimondi,[3] L. Ristori,[23] M. Roach-Bellino,[31] W. J. Robertson,[6] T. Rodrigo,[7] J. Romano,[5] L. Rosenson,[15] W. K. Sakumoto,[25] D. Saltzberg,[5] A. Sansoni,[8] V. Scarpine,[29] A. Schindler,[14] P. Schlabach,[9] E. E. Schmidt,[7] M. P. Schmidt,[33] O. Schneider,[14] G. F. Sciacca,[23] A. Scribano,[23] S. Segler,[7] S. Seidel,[18] Y. Seiya,[30] G. Sganos,[11] M. Shapiro,[14] N. M. Shaw,[24] Q. Shen,[24] P. F. Shepard,[22] M. Shimojima,[30] M. Shochet,[5] J. Siegrist,[28] A. Sill,[7a] P. Sinervo,[11] P. Singh,[22] J. Skarha,[12] K. Sliwa,[31] D. A. Smith,[23] F. D. Snider,[12] A. Sgolacchia,[3] L. Song,[7] T. Song,[16] J. Spalding,[7] L. Spiegel,[7] P. Sphicas,[15] A. Spies,[12] L. Stanco,[20] J. Steele,[32] A. Stefanini,[23] K. Strahl,[11] J. Strait,[7] D. Stuart,[7] G. Sullivan,[5] K. Sumorok,[15] R. L. Swartz, Jr.,[10] T. Takahashi,[19] K. Takikawa,[30] F. Tartarelli,[23] Y. Teramoto,[19] S. Tether,[15] D. Theriot,[7] J. Thomas,[28] R. Thun,[16] M. Timko,[31] P. Tipton,[25] A. Titov,[26] S. Tkaczyk,[7] K. Tollefson,[25] A. Tollestrup,[7] J. Tonnison,[24] J. F. de Troconiz,[9] J. Tseng,[12] M. Turcotte,[28] N. Turini,[3] N. Uemura,[30] F. Ukegawa,[21] G. Unal,[21] S. van den Brink,[22] S. Vejcik, III,[16] R. Vidal,[7] M. Vondracek,[10] R. G. Wagner,[1] R. L. Wagner,[7] N. Wainer,[7] R. C. Walker,[25] J. Wang,[5] Q. F. Wang,[26] A. Warburton,[11] G. Watts,[25] T. Watts,[27] R. Webb,[29] C. Wendt,[32] H. Wenzel,[14] W. C. Wester, III,[14] T. Westhusing,[10] A. B. Wicklund,[1] E. Wicklund,[7] R. Wilkinson,[21] H. H. Williams,[21] P. Wilson,[5] B. L. Winer,[25] J. Wolinski,[29] D. Y. Wu,[16] X. Wu,[23] J. Wyss,[20] A. Yagil,[7] W. Yao,[14] K. Yasuoka,[30] Y. Ye,[11] G. P. Yeh,[7] M. Yin,[6] J. Yoh,[7] T. Yoshida,[19] D. Yovanovitch,[7] I. Yu,[33] J. C. Yun,[7] A. Zanetti,[23] F. Zetti,[23] S. Zhang,[15] W. Zhang,[21] and S. Zucchelli[3]

(CDF Collaboration)

[1] *Argonne National Laboratory, Argonne, Illinois 60439*

[2] *Brandeis University, Waltham, Massachusetts 02254*

[3] *Istituto Nazionale di Fisica Nucleare, University of Bologna, I-40126 Bologna, Italy*

[4] *University of California at Los Angeles, Los Angeles, California 90024*

[5] *University of Chicago, Chicago, Illinois 60637*

[6] *Duke University, Durham, North Carolina 27708*

[7] *Fermi National Accelerator Laboratory, Batavia, Illinois 60510*

[8] *Laboratori Nazionali di Frascati, Istituto Nazionale di Fisica Nucleare, I-00044 Frascati, Italy*
[9] *Harvard University, Cambridge, Massachusetts 02138*
[10] *University of Illinois, Urbana, Illinois 61801*
[11] *Institute of Particle Physics, McGill University, Montreal H3A 2T8, and University of Toronto, Toronto M5S 1A7, Canada*
[12] *The Johns Hopkins University, Baltimore, Maryland 21218*
[13] *National Laboratory for High Energy Physics (KEK), Tsukuba, Ibaraki 305, Japan*
[14] *Lawrence Berkeley Laboratory, Berkeley, California 94720*
[15] *Massachusetts Institute of Technology, Cambridge, Massachusetts 02139*
[16] *University of Michigan, Ann Arbor, Michigan 48109*
[17] *Michigan State University, East Lansing, Michigan 48824*
[18] *University of New Mexico, Albuquerque, New Mexico 87131*
[19] *Osaka City University, Osaka 588, Japan*
[20] *Universita di Padova, Instituto Nazionale di Fisica Nucleare, Sezione di Padova, I-35131 Padova, Italy*
[21] *University of Pennsylvania, Philadelphia, Pennsylvania 19104*
[22] *University of Pittsburgh, Pittsburgh, Pennsylvania 15260*
[23] *Istituto Nazionale di Fisica Nucleare, University and Scuola Normale Superiore of Pisa, I-56100 Pisa, Italy*
[24] *Purdue University, West Lafayette, Indiana 47907*
[25] *University of Rochester, Rochester, New York 14627*
[26] *Rockefeller University, New York, New York 10021*
[27] *Rutgers University, Piscataway, New Jersey 08854*
[28] *Superconducting Super Collider Laboratory, Dallas, Texas 75237*
[29] *Texas A&M University, College Station, Texas 77843*
[30] *University of Tsukuba, Tsukuba, Ibaraki 305, Japan*
[31] *Tufts University, Medford, Massachusetts 02155*
[32] *University of Wisconsin, Madison, Wisconsin 53706*
[33] *Yale University, New Haven, Connecticut 06511*

This work was supported by the Director, Office of Energy Research, Office of High Energy and Nuclear Physics, Division of High Energy Physics, of the U.S. Department of Energy under contract DE-AC03-76SF00098.

Contents

Acknowledgements **iv**

1 Introduction **1**

1.1 Standard Model 1

1.2 History 3

1.3 B Physics at a Hadron Collider 6

1.4 Outline of the Analysis 8

2 Theory **11**

2.1 b Quark Production in $\overline{p}p$ Collisions 11

2.2 b Quark Fragmentation 14

2.2.1 Peterson Model 14

2.2.2 B Hadron Production 14

2.3 B Hadron Decay 15

2.3.1 Weak Decays 15

2.3.2 Hadronic $B \to J/\psi\ X$ Decays 16

2.4 Meson Mass 17

2.5 Current Evidence for B_s^0 and its Mass 19

3 CDF Detector **22**

3.1 Fermi National Accelerator Laboratory 22

3.1.1 Tevatron 23

3.1.2 B0 Interaction Region 24

3.2 CDF Detector 24

3.2.1 Tracking 24

3.2.2 Muon Systems 33

3.2.3 Calorimetry 36
3.3 Trigger System 37
3.3.1 Data Acquisition 37
3.3.2 Level 1 37
3.3.3 Level 2 38
3.3.4 Level 3 41
3.3.5 Stream 2 41

4 Data Set **42**
4.1 Statistics of the 1992–1993 Run 42
4.2 Express Production 42
4.3 J/ψ Sample 44
4.3.1 Approach 44
4.3.2 Trigger Requirements on Processed Events 46
4.3.3 Muon Characteristics 46
4.4 Muon Selection 50
4.5 J/ψ Mass Window Requirement 53

5 Analysis **55**
5.1 Track selection 55
5.2 Daughter Meson 57
5.3 Constrained Fits 57
5.3.1 Unconstrained Mass Window Requirements 60
5.3.2 Primary Vertex 63
5.3.3 Constrained Fit and Secondary Vertex 65
5.4 Preserving Signal 65
5.4.1 Kinematics of $B \to J/\psi\ X$ 68
5.4.2 Expected $c\tau$ Distribution for Signal 68
5.4.3 Expected CL(χ^2) Distribution for Signal 71
5.5 Combinatoric Background Reduction 71
5.5.1 Kinematics for Background 73
5.5.2 $c\tau$ for Background 73
5.5.3 CL(χ^2) for Background 76
5.5.4 Correlations between the Selection Criteria 79

6 Reconstruction of Exclusive B Decays into J/ψ **82**
6.1 P_T Scale Correction 82
6.2 Selection Criteria 83
6.2.1 B Reconstruction 86
6.2.2 Daughter Meson Mass Window 91
6.2.3 Kinematics for Signal 91
6.2.4 $c\tau$ for Signal 97
6.2.5 CL(χ^2) for Signal 97
6.3 The Reconstruction of $B_s^0 \to J/\psi\ \phi$ 100
6.4 Mass Measurement 100
6.4.1 Fitting 100
6.4.2 Results 104

7 Systematic Uncertainties **108**
7.1 Selection Criteria 108
7.2 Fitting Procedure 109
7.3 Constrained Fits 109
7.4 Pt Scale 109
7.5 Covariance Matrix 114
7.6 False Curvature 119
7.7 $\Delta\cot\theta$ 119
7.8 Summary and Conclusions 131

8 Conclusions **132**

Bibliography **134**

List of Tables

1.1 Fundamental particles of the Standard Model 2

2.1 Theoretical predictions of the mass of the B_s^0 meson 20

3.1 Characteristics of each SVX layer 29
3.2 CTC mechanical parameters 33

4.1 Gaussian fits of muon matching distributions 50
4.2 Muon sections requirements 53

5.1 Fit results of J/ψ candidates under various constraints 58
5.2 Fit results of $J/\psi\ K^-$ mass under various constraints 60
5.3 Minimal selection requirements for $B \to J/\psi\ X$ candidates 73
5.4 Efficiency of P_T cuts on combinatoric background 73
5.5 Efficiency of $c\tau$ cut on combinatoric background 76
5.6 Efficiency of CL(χ^2) cut on combinatoric background 76

6.1 Final selection criteria for $B \to J/\psi\ X$ reconstruction 87
6.2 Efficiency of P_T cuts on B candidates in the data 95
6.3 Efficiency of $c\tau$ cuts on B candidates in the data 97
6.4 Efficiency of CL(χ^2) cuts on B candidates in the data 100
6.5 Fit results of reconstructed B mesons 104

7.1 Fit results of B^- and B^0 mesons under different selection 110
7.2 Fit results of B_s^0 mesons under different selection 111
7.3 B meson results using different fitting procedures 112
7.4 Fit results of B mesons in regions of $\Delta\cot\theta$ 123
7.5 Summary of systematic uncertainties 131

List of Figures

1.1 Mass of $B^- \to J/\psi\ K^-$ candidates 10

2.1 Feynman diagrams of $b\overline{b}$ production 12
2.2 Cross section for b quark production 13
2.3 Peterson fragmentation function 14
2.4 Feynman diagrams of spectator two-body Weak decay 16

3.1 Layout of Fermilab 23
3.2 Side view representation of the CDF detector 25
3.3 Representation of the CDF detector 25
3.4 SVX barrel 27
3.5 SVX ladder 28
3.6 CTC end plate 32
3.7 Central muon chambers within a calorimeter 34
3.8 Centrual muon chamber tower 35
3.9 Level 1 dimuon trigger efficiency 39
3.10 Level 2 dimuon trigger efficiency 40

4.1 Dimuon mass of events which pass the Stream 2 trigger 43
4.2 J/ψ mass versus the maximum muon η 45
4.3 Muon type of J/ψ and sideband dimuons 48
4.4 P_T of muons of J/ψ and sideband muons 49
4.5 Muon matching distributions 51
4.6 Hadron energy of J/ψ and sideband dimuons 52
4.7 Dimuon mass of events failing muon cuts 54

5.1 Number of axial and stereo wires of J/ψ and sideband dimuons . 56
5.2 Dimuon mass under various constraints 59

5.3 $J/\psi\ K^-$ mass with and without dE/dx corrections 61
5.4 $J/\psi\ K^-$ mass with and without a pointing constraint 62
5.5 $J/\psi\ K^-$ mass from unconstrained and constrained reconstruction 64
5.6 Beam profile at CDF 66
5.7 Difference in z_0 of the dimuon vertex and primary vertex 67
5.8 Monte Carlo P_T distributions of mesons in $B \to J/\psi\ X$ decays . . 69
5.9 Monte Carlo P_T distributions and cut efficiencies 70
5.10 CL(χ^2) distribution of J/ψ and sideband dimuons 72
5.11 K^* and ϕ candidate mass distributions 74
5.12 Efficiency of P_T cuts on combinatoric background 75
5.13 Efficiency of $c\tau$ cut on combinatoric background 77
5.14 Efficiency of CL(χ^2) cut on combinatoric background 78
5.15 Correlations between P_T cuts with $c\tau$ or CL(χ^2) cuts 80
5.16 Correlations between $c\tau$ with CL(χ^2) cuts 81

6.1 J/ψ mass before and after P_T scale corrections 84
6.2 Υ masses before and after P_T scale corrections 85
6.3 $J/\psi\ K^-$ mass with successive applications of the cuts 88
6.4 $J/\psi\ K^*$ mass with successive applications of the cuts 89
6.5 $J/\psi\ \phi$ mass with successive applications of the cuts 90
6.6 P_T distribution of daughter mesons from reconstructed B mesons 92
6.7 P_T distribution of reconstructed B mesons 93
6.8 Efficiency of P_T cuts on B candidates in the data 94
6.9 Example of calculating the efficiency of a cut 96
6.10 $c\tau$ distribution of reconstructed B mesons 98
6.11 Efficiency of $c\tau$ cuts on B candidates in the data 99
6.12 CL(χ^2) distributions of reconstructed B mesons 101
6.13 Efficiency of CL(χ^2) cuts on B candidates in the data 102
6.14 $J/\psi\ \phi$ and K^+K^- mass of B_s^0 candidates 103
6.15 $B^- \to J/\psi\ K^-$ mass 105
6.16 $B^0 \to J/\psi\ K^*$ mass 106
6.17 $B_s^0 \to J/\psi\ \phi$ mass 107

7.1 B meson mass difference for different constraints 113

7.2 B meson mass difference for B field uncertainty 115
7.3 B meson mass difference for material scale uncertainty 116
7.4 B meson mass difference for global covariance matrix uncertainty 117
7.5 B meson mass difference for covariance matrix uncertainty 118
7.6 J/ψ mass versus P_T of each muon 120
7.7 B meson mass difference for false curvature effect 121
7.8 J/ψ K^- mass separated between K^+ and K^- 122
7.9 J/ψ mass versus $\Delta\cot\theta$ between the muons 124
7.10 B meson mass difference for $\Delta\cot\theta$ effect 125
7.11 B^- mass in regions of $\Delta\cot\theta_{J/\psi\ K}$ 126
7.12 B^0 mass in regions of $\Delta\cot\theta_{J/\psi\ K^*}$ 127
7.13 B_s^0 mass in regions of $\Delta\cot\theta_{J/\psi\ \phi}$ 128
7.14 B^0 mass in regions of $\Delta\cot\theta_{K\pi}$ 129
7.15 B_s^0 mass in regions of $\Delta\cot\theta_{K^+K^-}$ 130

Chapter 1

Introduction

The Quark Model predicts the existence of the B_s^0 meson, a bound state of a bottom and strange quark/antiquark pair. The model does not directly predict its mass. This dissertation describes the full reconstruction of the B_s^0 meson through the decay chain $B_s^0 \rightarrow J/\psi\ \phi$, $J/\psi \rightarrow \mu^+\ \mu^-$, $\phi \rightarrow K^+\ K^-$ using data obtained at the Collider Detector at Fermilab (CDF). The mass of the B_s^0 meson is determined by analyzing the final state decay particles. The B^- and B^0 mesons are also reconstructed using the kinematically similar decays $B^- \rightarrow J/\psi\ K^-$ and $B^0 \rightarrow J/\psi\ K^*$.

In this chapter, a description of the Standard Model will be followed by a brief history of B physics. Next, the environment of a hadron collider and the unique capabilities of CDF will be discussed and compared with other experiments doing B physics. The chapter ends by outlining the analysis of the mass measurement of the B_s^0 meson. The following chapter will present the theoretical motivation for the mass measurement along with further theoretical discussion.

1.1 Standard Model

The Standard Model of particle physics describes the fundamental particles and the interactions between them. Table 1.1 shows these fundamental particles[1] arranged in a way to highlight several aspects of the theory. The fundamental particles are fermions and force-carrying bosons – having spin angular momentum of odd half-integer and integer respectively. The fermions include six quarks – particles which can interact via the strong force. The strong force is transmitted by the exchange of gluons. Quantum Chromodynamics [1] (QCD) describes the strong interaction using the property of color SU(3) group symmetry. Quarks

[1]Unless otherwise noted, references to a specific charge state should be implied to pertain also to the charge conjugate state

and gluons carry the color property. The quarks are arranged in three families of doublets with a charge $+2/3$ quark matched with a charged $-1/3$ quark. This grouping of doublets is relevant to the description of electroweak interactions transmitted by the exchange of W, Z^0, and γ. For W exchange between a u-like quark and a d-like quark, the convention is that the d-like quarks mix to allow each u-like quark to couple to any of the d-like quarks. This mixing will be described in greater detail below. Electroweak theory [2] involves the $SU(2)_L \otimes U(1)_Y$ group. Fermions can exist in a state of being left-handed (the "L") or right-handed (except for neutrinos which are only left-handed in the Standard Model). The hypercharge, Y, of the fermions is related to the electromagnetic charge, Q, and z-component of the Weak force isospin, T_z, which the fermions possess:

$$Y = 2 \times (Q - T_z) \tag{1.1}$$

Leptons do not interact via the strong force but do interact with the electroweak force and hence are arranged in a similar doublet structure. The Higgs boson [3], which couples to the mass of particles, has not been experimentally observed and is used in the Standard Model to explain the unification of electromagnetism and the weak force.

Fermions								Bosons
Quarks			Q($\|e\|$)	Leptons			Q($\|e\|$)	$W^{\pm}$,Z^o,γ,
up	*charm*	*top* [4]	+2/3	ν_e	ν_μ	ν_τ	0	gluons (g),
down	*strange*	*bottom*	-1/3	e	μ	τ	-1	(Higgs Φ)
Fermions have antiparticle counterparts								
Quarks come in 3 colors (R,G,B)								
Gluons come in 8 colors								
Neutrinos, γ, and gluons are massless								

Table 1.1: Fundamental particles of the Standard Model

Leptons are directly observable in nature. Quarks, however, are not directly observed in that they do not appear to exist by themselves as free particles. The theoretical model describes quarks bound in objects which are color singlets. A colored quark can be bound with an antiquark with corresponding anticolor to form a meson. Three quarks of different color can be bound to form a baryon. Mesons and baryons are collectively called hadrons to be distinguished from the leptons and field bosons as the "particles" which can be directly measured. Matter which is most abundant in nature is composed of the first family of fundamental particles. In the lepton sector, electrons appear along with its neutrino. In the hadron sector, protons and neutrons are made of u and d quarks. The most

abundant meson is the pion which is also made of u and d quarks. At high energy accelerators such as the Fermi National Accelerator Laboratory (FNAL), collisions take place which can cause the production of fundamental particles in the second and third families. In this dissertation, the B_s^0 meson ($b\overline{s}$) consisting of a bottom and strange, quark/antiquark pair is studied and its mass is measured. Other B mesons include the charged B^- containing a b and u quark/antiquark pair and the neutral B^0 containing a b and d quark/antiquark pair. Though the study of hadrons containing the bottom quark has been on going for over a decade, the B_s^0 has been elusive in terms of direct observation.

1.2 History

In November of 1974, a "revolution" took place in the field of elementary particle physics with the simultaneous discovery of a narrow resonance at 3.1 GeV/c^2 by experiments conducted at two national laboratories. One focused on hadroproduction and the other on e^+e^- collisions. This particle was observed both at the Brookhaven National Laboratory (BNL) [5] where the particle was named the J and at the Stanford Linear Accelerator Center (SLAC) [6] where the particle was named the ψ. At BNL, protons incident on a Beryllium target were used to search for a resonance decaying into e^+e^-. At SLAC, electrons and positrons were annihilated and a measurement of the total cross section at various energies indicated the presence of the resonance. The particle, now called J/ψ, is known as being a bound state of a charm and anticharm quark/antiquark pair.

Until 1974, the electron, muon, and their neutrinos were known to exist along with a number of hadrons. The hadrons known in 1974 fit into a theoretical model which contained only 3 quarks (*up*, *down*, and *strange*) and their antiquarks. In the three quark model, weak decays involved the left-handed doublet ($u_L, d_L^{/} = d\cos\Theta_C + s\sin\Theta_C$) and the singlet $s_L^{/} = s\cos\Theta_C - d\sin\Theta_C$ where Θ_C is the Cabibbo angle [7] – a measure of the $d - s$ quark mixing. In this model, one would expect to observe neutral strangeness-changing decays such as $K_L^0 \to \mu^+\mu^-$ which has a rate proportional to $+\cos\Theta_C \sin\Theta_C$. Such decays were not observed at the expected rate. A theoretical explanation for the nonobservation was given in 1970 [8]. This "GIM mechanism" requires a fourth quark to form a second doublet, ($c_L, s_L^{/}$), allowing for $K_L^0 \to \mu^+\mu^-$ to decay proportional to $-\cos\Theta_C \sin\Theta_C$ which cancels the contribution from the first doublet (assuming the u and c masses are identical). The experimental discovery of the J/ψ provided proof for the existence of the forth quark, charm.

Before the experimental discovery of the charm quark, the doublet structure of the weak interactions was extended to allow for a third family [9]. In this theory,

the quark mixing is given by the Cabibbo-Kobayashi-Maskawa (CKM) matrix:

$$\begin{pmatrix} d' \\ s' \\ b' \end{pmatrix} = \begin{pmatrix} V_{ud} & V_{us} & V_{ub} \\ V_{cd} & V_{cs} & V_{cb} \\ V_{td} & V_{ts} & V_{tb} \end{pmatrix} \begin{pmatrix} d \\ s \\ b \end{pmatrix} \tag{1.2}$$

The elements V_{ij} of the matrix represent the coupling between an u-like quark with the corresponding d-like quark. The elements V_{ud} and V_{us} represent $\cos\Theta_C$ and $\sin\Theta_C$ respectively (neglecting the small contribution of the third family). The CKM matrix can be parameterized [10] as follows:

$$V \sim \begin{pmatrix} 1-\lambda^2/2 & \lambda & A\lambda^3(\rho - i\eta) \\ -\lambda & 1-\lambda^2/2 & A\lambda^2 \\ A\lambda^3(1-\rho-i\eta) & -A\lambda^2 & 1 \end{pmatrix} \tag{1.3}$$

where the parameters have been determined to be λ=0.22 [10], $A = 0.90 \pm 0.12$ [11], and $\sqrt{\rho^2+\eta^2} = 0.39 \pm 0.07$ [11]. Of particular interest is the fact that the matrix contains a complex phase, η. The imaginary component in the quark mixing matrix occurs when there are at least three families of doublets. Furthermore, it is the imaginary component which can account for CP violation which had been observed in the neutral kaon system [12]. Theory suggested that a third family should exist. The tau lepton was discovered in 1975 [13] supporting the existence of a fifth and sixth quark.

The search began for observing the fifth quark, the bottom or *beauty* quark. The first experimental observation of bottom production came in 1977 by studying 400 GeV/c protons incident on a variety of targets. The experiment observed of a resonance of $\mu^+\ \mu^-$at a mass of 9.5 GeV/c^2 [14]. In the following year, the resonance was confirmed by an experiment studying e^+e^- annihilation [15]. This resonance known as the upsilon, Υ, is understood as being a bound state of a bottom and antibottom quark/antiquark pair. Two additional narrow resonances of higher masses were also observed, the Υ(2S) and Υ(3S).

The study of hadrons consisting of one bottom quark began in 1980 at the Cornell Electron Storage Ring (CESR) [16] in e^+e^- collisions where a higher energy and broad Υ resonance was observed. The broad width of the Υ(4S) state indicated that it was above the mass threshold for decaying into mesons containing a bottom quark as opposed to the lower lying Υ states which decayed via the annihilation of the bottom quark and bottom antiquark (and hence were very narrow). A series of measurements of inclusive decays of bottom mesons where the meson was not fully reconstructed[2] thus began. By tuning the e^+e^-

[2] A *reconstructible* decay mode is one where all the final state particles can be identified and measured. Usually this implies that there are only a few final state particles which are all charged.

collision energy to precisely the mass of the $\Upsilon(4S)$, B mesons could be produced copiously and their inclusive decays could be studied. Further experimentation at the PEP and Petra colliders was performed above the $\Upsilon(4S)$ resonance where the e^+e^- could annihilate into pairs of B mesons. All of these studies began to shed light on the weak decays of the bottom quark.

Studies of exclusive decays of bottom mesons where the meson was fully reconstructed began three years later in 1983 [17] at CESR where both a charged and neutral B meson were observed by identifying all of the decay products. Since the B meson is heavy, it can decay into a large number of final states which often involve difficult-to-identify neutral particles or particles with very low momenta. Thus, the probability of observing a fully reconstructed B meson is low ($\sim 10^{-4}$). Since 1983, e^+e^- experiments both at CESR and at the DORIS (located in Hamburg, Germany) storage rings began to study B meson decays both inclusively and exclusively. Upgrades to the experiments involved trying to accumulate as much data as possible in order to reduce the statistical error on their measurements. In the 10 years of experimentation dedicated to measurements of the B meson system, of order of 1000 fully reconstructed B mesons have been observed [18]. These B mesons include the charged B^- and B^0 but not the B_s^0 meson because it is too massive to be a decay product of the $\Upsilon(4S)$. Higher state $\Upsilon(5S)$, which is expected to decay into B_s^0 mesons, have not been produced in large enough numbers (due to the relatively small production cross section) for B_s^0 to be fully reconstructed.

The neutral intermediate vector boson, Z^0, decays into bottom quarks approximately 15% of the time [19]. These b quarks combine with other quarks to form b hadrons. Experiments of e^+e^- collisions at the mass of the Z^0 at the Large Electron Positron collider (LEP) and the Stanford Linear Collider (SLC), where large numbers of Z^0s are produced, also study both inclusive and exclusive b hadron decays. The number of fully reconstructed b hadron decays at LEP and SLC is smaller than at the machines tuned on the $\Upsilon(4S)$ due to the smaller integrated luminosity and smaller cross section times branching ratio for $Z^0 \rightarrow bX$ decays. However, since the Z^0 is so much heavier than the b quark, the b hadrons which are produced at LEP and SLC can be any species including the B_s^0 meson as well as B baryons. In addition, b hadrons decay through weak interactions with a lifetime of approximately a picosecond. At the $\Upsilon(4S)$, the B mesons are produced nearly at rest so that they do not travel far in the laboratory before they decay. At SLC and LEP, the b hadrons are produced with large momentum so that with their lifetime, they will travel a measurable distance before decaying. This fact is used to help in selecting those Z^0 decays which have b hadron final states.

The early history of the experimental study of b hadrons has been described for several reasons. First, the observation of heavy flavors including b hadrons provided strong evidence supporting the Standard Model. Second, because of

the unique properties of the b quark such as its being a member of the third family, its heavy mass, and its picosecond lifetime, important measurements of fundamental parameters of the Standard Model as well as measurements of more subtle effects which the theory predicts are able to be made. Finally, the early history of the study of b hadrons shows that there are many approaches toward making measurements – hadroproduction, e^+e^- collisions at the $\Upsilon(4S)$ and at higher energies including at the Z^0. Each of these approaches has made unique contributions in this field of B physics. Each approach has certain advantages and disadvantages. Another approach is to study B decays in a hadron collider environment. Inclusive B measurements have been performed at hadrons colliders both by the UA1 and CDF experiments. This thesis is the first example of an exclusive B meson measurement which is best done in a hadron collider at this time.

1.3 B Physics at a Hadron Collider

Hadron colliders have several aspects which make them a good place to do measurements in B physics. At a hadron collider, large numbers of b hadrons are produced due to a large integrated luminosity times cross section for b quark production. The production cross section is very large relative to e^+e^- experiments. The total cross section for $b\bar{b}$ production at the Tevatron is approximately 50 μb and approximately 12 μb [20] for b quarks and antiquarks produced with rapidity $|\mathrm{y}| < 1$ and $P_T > 7.5$ GeV/c. Rapidity is defined in terms of energy, E, and z-component of momentum, P_z, by the relation:

$$\mathrm{y} = \frac{1}{2}\log\left(\frac{\mathrm{E}+P_z}{\mathrm{E}-P_z}\right) \tag{1.4}$$

This dissertation is based on 19.3 pb^{-1} of data collected during the 1992–1993 (Run IA) year of collider operation. The experiment produced approximately 1×10^8 $b\bar{b}$ pairs with $|\mathrm{y}| < 1$. Not all of the $b\bar{b}$ pairs are useable for measurements and that will be discussed below. The $b\bar{b}$ cross section in $\bar{p}p$ collisions can be compared to the 1.1 nb cross section for an $\Upsilon(4S)$ decaying into a B mesons. At the Z^0, the cross section of b quark production is 6.7 nb. Assuming operation at 10^7 seconds at a luminosity of $10^{32}\mathrm{cm}^2\mathrm{s}^{-1}$, an experiment at CESR could hope to produce close to 10^6 $b\bar{b}$ pairs from $\Upsilon(4S)$ decay. At LEP, producing four million Z^0s a year would yield approximately 6×10^5 $b\bar{b}$ produced per year.

There are advantages and disadvantages of doing B physics at CESR and LEP. At CESR, there is an additional benefit of sitting at the $\Upsilon(4S)$ which is a known initial state in terms of its mass and quantum numbers. In addition, the $\Upsilon(4S)$ decays into $B\overline{B}$ mesons with a branching ratio of nearly 100%. Finally, the ratio of the cross section for $b\bar{b}$ to the total cross section (which includes the

continuum e^+e^- spectrum) is approximately 1:3 which is quite large. However, because the B mesons are produced from a $J^{PC} = 1^{--}$ state, the resultant B mesons are restricted in terms of what states are allowed. At CESR, the b hadrons have very little momentum since the decay is very near threshold. Thus, direct measurements of a particular B meson lifetime cannot be easily made. Also, only B^- and B^0 mesons are able to be produced since the decay is below the threshold for the production of the more massive B_s^0 state. At LEP, the initial state is also known and $\sigma_{b\bar{b}}/\sigma_{\rm TOT}$ is a rather large 15%. The b hadrons are boosted as the Z^0 mass is much larger than any B hadron mass. At LEP, production of all species of b hadrons is theoretically possible. The main disadvantage is the relatively low b production cross section which must be combined with the low branching ratio ($\sim 10^{-4}$) for exclusive b hadron decays. Thus, in a typical year, LEP may record roughly 100 fully reconstructed b hadron decays.

The environment of a hadron collider also has advantages and disadvantages for making B physics measurements. While the cross section for $b\bar{b}$ is large compared to that at e^+e^- experiments, the cross section is small compared with the total cross section in $\bar{p}p$ collisions: $\sigma_{b\bar{b}}/\sigma_{\rm TOT} \sim 6 \times 10^{-4}$. The challenge of doing B physics at a hadron collider is to efficiently trigger on events with a high likelihood of being B enriched relative to other events. Practically this is accomplished by triggering on high-P_T leptons or by triggering on dimuons consistent with $J/\psi \to \mu^+ \mu^-$ decays. High-P_T leptons arise from the semileptonic decay of the B hadron. Backgrounds at very high-P_T from W and Z^0 decays are easily removed. Backgrounds at lower-P_T come mainly from semileptonic decays of charmed hadrons, photon conversions, decays-in-flight, and other *fakes* such as hadronic punch through – which are more difficult to remove. Nevertheless, semileptonic decays are the subject of B physics studies in hadron colliders. Measurements of the production cross section, mixing, and lifetimes are possible. However, since the neutrino from semileptonic decays is not identifiable, full reconstruction of b hadrons is not possible.

By triggering on dimuons which could be coming from J/ψ decays, one is able to obtain a sample of events which is enriched in reconstructible B hadrons. b hadrons decay into J/ψ particles with a branching ratio of 1.12% [21]. Many of these decays involve only a couple of additional charged tracks which can be combined with the J/ψ for complete reconstruction. With approximately 10^8 B mesons produced in a year at a hadron machine (in the central region of the detector) and a reconstruction efficiency of 1% for several modes, hundreds of reconstructed b hadrons per year are expected. Dimuons are used because the trigger is easier to implement with lower background rates than the dielectron events. In short, the $J/\psi \to \mu^+ \mu^-$ trigger allows one to obtain a sample of events enriched in b hadrons which can be fully reconstructed.

Obtaining large numbers of reconstructed b hadrons is difficult in other experimental environments because the cross section times branching ratio is small. There are several B physics measurements which require full reconstruction and the hadron collider environment *is* competitive in doing these measurements. The mass determination of the B_s^0 meson is one specific example and is the subject of this analysis.

1.4 Outline of the Analysis

The analysis to determine the mass of the B_s^0 meson is outlined here. To begin, events are used which pass the CDF dimuon J/ψ trigger. From these events, selections are made to remove background to obtain a relatively pure sample of J/ψ dimuons. In this first stage, efficiency is emphasized over background rejection since the J/ψ signal is large compared with the background. From these J/ψ events, candidates of the following decays are reconstructed.

- $B^- \rightarrow J/\psi\ K^-$
- $B^0 \rightarrow J/\psi\ K^*$
- $B_s^0 \rightarrow J/\psi\ \phi$

These decays are reconstructed by combining selected tracks with the J/ψ and applying a further set of selection criteria to reduce combinatoric background. The reconstruction begins by imposing track quality requirements in order to insure that the tracks are well measured. In order to improve the mass resolution, the tracks which are combined are subject to constraints that they all originate from a common vertex and that the dimuons have an invariant mass equal to the world average J/ψ mass and that the resultant system points back to the determined primary event vertex in the r-ϕ plane. The combinatoric background is extremely large compared with the expected signals. This background is reduced relative to the signal by applying cuts on kinematic variables such as the P_T of the mesons in the decay. Cuts are also applied on the lifetime of the reconstructed B meson. A further requirement is made on the CL(χ^2) of the constrained fit. As an example, Fig. 1.1 shows the mass distribution of $B^- \rightarrow J/\psi\ K^-$ candidates with the following requirements:

- $|\text{Mass}(\mu^+\mu^-) - \text{Mass}(J/\psi)\ | < 100\ \text{MeV}/c^2$
- $P_T(K) > 2\ \text{GeV}/c$
- $P_T(B^-) > 8\ \text{GeV}/c$

- $c\tau > 100\mu$m
- CL(χ^2) > 1%

Each of the selection requirements are studied in terms of their efficiency for preserving signal and for their ability to reject background. Care is taken to insure that cuts used to reconstruct $B_s^0 \to J/\psi\ \phi$ have not been tuned on the data where the possibility exists of enhancing a background fluctuation. The mass determination is studied and corrections are applied based on studying systematic effects in track reconstruction. The mass distributions of the resultant decays are fitted to obtain the number of candidate events with a mass and statistical uncertainty. The reconstruction of B^- and B^0 gives confidence in the methodology used to reconstruct B_s^0. In addition, the reconstruction of the lighter B mesons can be used to help in determining the systematic uncertainty of the measurement. In addition to this determination of uncertainty, other sources are evaluated. The conclusion of this analysis is the direct demonstration of the existence of the B_s^0 meson, a precision measurement of its mass, and a demonstration that exclusive B physics can be done at a hadron collider.

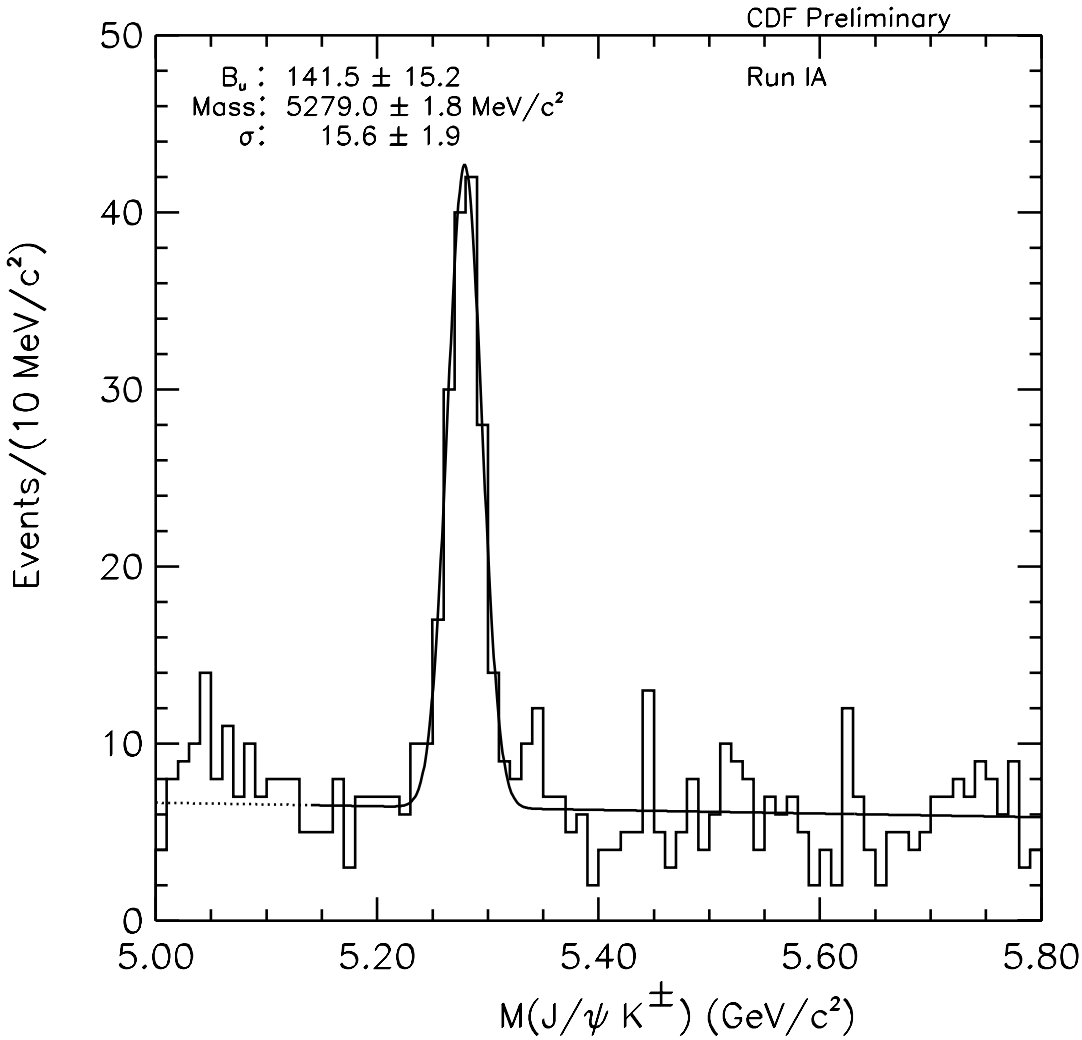

Figure 1.1: Mass distribution of $B^- \to J/\psi\ K^-$ candidates.

Chapter 2

Theory

This chapter will introduce important theoretical concepts which play a large role in the physics behind this thesis topic. The mass measurement of the B_s^0 meson is possible because b quarks are produced in $\overline{p}p$ collisions. The b quarks fragment into B mesons carrying on average a large fraction of the original momentum of the b quark. Also, a certain fraction of the time, a B_s^0 meson will result from the fragmentation process. b hadrons are not stable and decay by means of the Weak force. In the case where such decay is into all hadrons, QCD can play an important role. The theory describes some of the effects QCD plays in B decays including the specific $B \rightarrow J/\psi\ X$ decays. The theory uses models to predict the masses of meson states. These models often involve a parameterization of the QCD potential in a non-relativistic approximation expected to be valid for mesons composed of heavy flavor quarks. Recent calculations using techniques of QCD lattice gauge calculations also carry predictive power on what the B_s^0 meson mass is expected to be. The chapter concludes by describing the current experimental evidence for the existence of the B_s^0 meson and its mass determination.

2.1 b Quark Production in $\overline{p}p$ Collisions

The production of b quarks in $\overline{p}p$ collisions is understood in the context of a QCD process. Incoming u and d quarks and gluons from the proton and antiproton interact producing a $b\overline{b}$ quark/antiquark pair. In Fig. 2.1, several Feynman diagrams of this process are shown. A QCD calculation (NDE) of these processes and all others to next-to-leading order has been performed [22]. Using a set of parton distribution functions which have been shown to match CDF data [23], one can calculate the theoretical expectation of the cross section for b quark production as a function of the P_T of the quark. Figure 2.2 shows this theoretical prediction along with a number of measurements using other CDF data.

Figure 2.1: Feynman diagrams which contribute to $b\bar{b}$ production in hadron collisions.

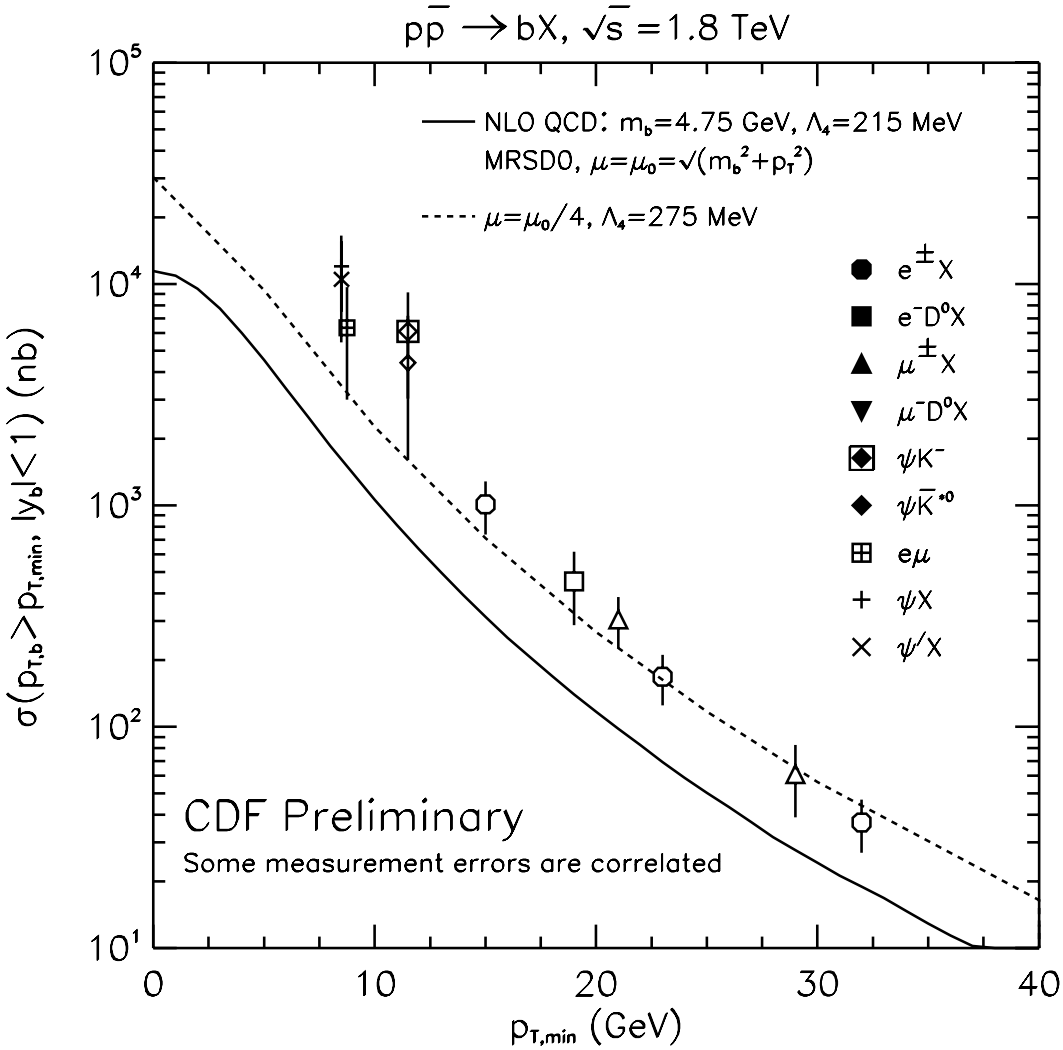

Figure 2.2: Cross section for b quark production showing both experimental data points from CDF and a range of theoretical predictions.

2.2 b Quark Fragmentation

2.2.1 Peterson Model

Once b quarks are produced, they *fragment* into b hadrons. The fragmentation process involves the theoretical prediction of the fraction of the momentum the b hadron carries relative to that of the original b quark. The Peterson model [24] uses arguments based on kinematics to derive Equation 2.1:

$$\mathrm{D}_{\mathrm{q}}^{\mathrm{H}}(\mathrm{z}) = \mathrm{K}\mathrm{z}^{-1}\left(1 - \frac{1}{\mathrm{z}} - \frac{\epsilon_{\mathrm{q}}}{1-\mathrm{z}}\right)^{-2} \tag{2.1}$$

where $\mathrm{D}_{\mathrm{q}}^{\mathrm{H}}$ is the fragmentation function for the quark q to fragment into the hadron H, z is the fraction of the b quark momentum carried by the b hadron, K is a constant, and ϵ_b is the Peterson parameter determined to be 0.006 ± 0.002 for the b quark and $0.06^{+0.03}_{-0.02}$ for the lighter c quark [25]. Figure 2.3 shows the fragmentation function for b quarks. Note that there is a large peaking towards high z. This implies that on average, most of the momentum of the original b quark is carried by the B meson. For c quarks, the fragmentation function peaks at a lower value around 0.7.

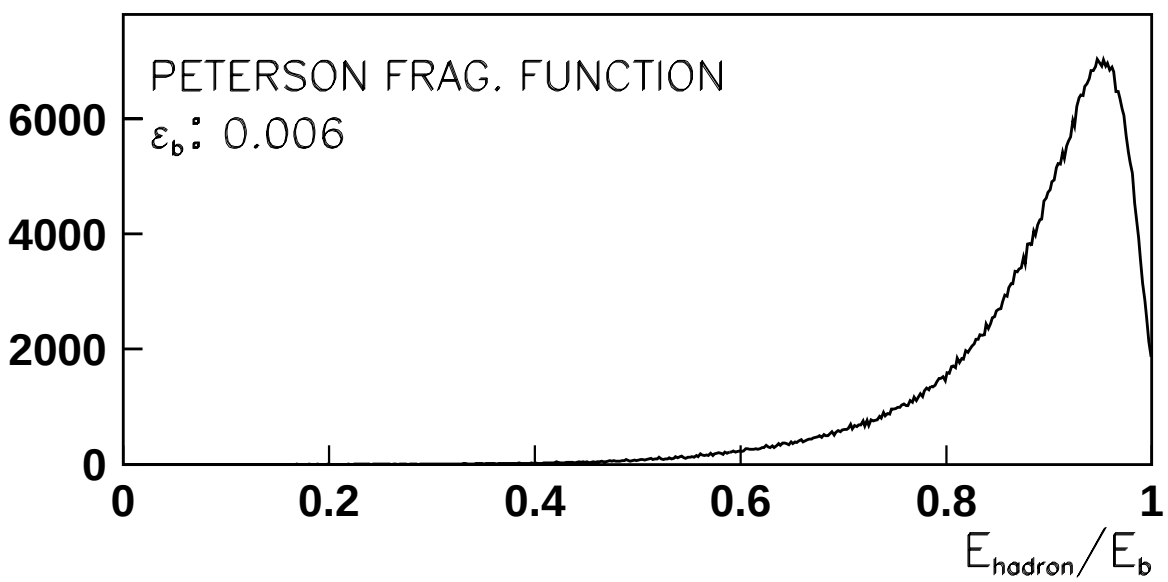

Figure 2.3: Peterson fragmentation function for bottom quarks.

2.2.2 B Hadron Production

A second issue described by the fragmentation process is the expected species of the b hadron. Since the s quark is heavier than the u and d quarks, it is less

likely to be created during the hadronization process. Baryon production is also expected to be suppressed. Based on measurements of the relative production of pions to kaons to protons, an estimate can be made for producing the different species of b hadrons: B^-:B^0:B_s^0:$B_{baryons}$ = 37.5%:37.5%:15%:10%. The relatively lower production of B_s^0 to the lighter B mesons is one factor which makes looking for the B_s^0 more difficult. Besides the relative rates of production for the different species of B mesons, the relative number of each type expected to be reconstructed also depends on the branching ratio into the particular final state as described below.

2.3 B Hadron Decay

b hadrons are not stable – they decay. It is through their decay products that they can be identified. The Weak force is responsible for b hadron decays although QCD plays a non-negligible role.

2.3.1 Weak Decays

The spectator model for a two-body weak decay of a B meson is illustrated by the Feynman diagrams in Fig. 2.4. In the spectator model, the light quark appears both in the initial and final state particles. The bottom diagram is relevant for $B \to J/\psi\ X$ two-body decays. This same basic diagram applies to the calculation of $B^- \to J/\psi\ K^-$, $B^0 \to J/\psi\ K^*$, and $B_s^0 \to J/\psi\ \phi$ depending on whether the "spectator" quark is a u, d, or s. The decay width for a b quark decaying into a lighter quark is given by Eq. 2.2:

$$, _{sl}(b \to q) = \frac{G_F^2 m_b^5}{192\pi^3} \cdot |V_{qb}|^2 \cdot F(\epsilon) \tag{2.2}$$

where $G_F = 1.17 \times 10^{-5} GeV^{-2}$ is the Fermi coupling constant of the weak decay, V_{qb} is the element of the CKM [7, 9] matrix for the $b \to q$ transition, m_b is the mass of the b quark, and F(ϵ) [26] can be written as the product of a phase space term and a QCD correction factor term:

$$F(\epsilon) = \phi_{PS}(\epsilon) \times \phi_{QCD}(\epsilon) \tag{2.3}$$

where $\epsilon = m_q/m_b$ and

$$\phi_{PS}(\epsilon) = 1 - 8\epsilon^2 + 8\epsilon^6 - \epsilon^8 - 24\epsilon^4 \log \epsilon \tag{2.4}$$

Studies of two-body weak decays of B mesons shed light on the Standard Model parameters (V_{qb}, α_s, etc.) as well as subtle QCD effects which will be discussed

Figure 2.4: Feynman diagrams of the spectator model for the Weak two-body decay of a B meson. The bottom diagram shows the color-suppressed B decay into a J/ψ.

2.3.2 Hadronic $B \to J/\psi\ X$ Decays

The lower diagram in Fig. 2.4 is an example of a color-suppressed spectator diagram. The spectator quark in the decay begins by having the anticolor of the $\overline{b}$ quark. The virtual W is a color singlet and the diagram is possible only if the c and $\overline{s}$ from the W are such that their color matches to form a color singlet

J/ψ and daughter mesons. In the non-suppressed diagram (the top diagram in Fig. 2.4), the $\overline{c}$ would combine with the spectator quark and the virtual W would give rise to a set of mesons or leptons. The color suppression factor is expected to be $1/N_c^2 = \frac{1}{9}$ where $N_c = 3$ is the number of colors; however, soft gluon exchange mitigates the suppression.

Because of the non-purturbative nature of QCD in the soft regime which is present in B decays, calculations rely on models and approximations. The BSW model [27] makes a factorization assumption in which the soft processes can be absorbed into a hadronic interaction and hard processes can be incorporated into the weak decay and the hadronic component is the product of two currents. This model includes QCD coefficients and the effective color suppression factor into two parameters, a_1 (relevant for non-color suppressed decays) and a_2 (relevant for color suppressed decays). The numeric value of these decays can be obtained by fitting different two-body decays of B^- and B^0 [18] to obtain:

$$|a_1| = 1.15 \pm 0.04 \pm 0.05 \pm 0.09 \tag{2.5}$$

$$|a_2| = 0.26 \pm 0.01 \pm 0.01 \pm 0.02 \tag{2.6}$$

$$a_2/a_1 > 0 \tag{2.7}$$

Theoretical predictions [28] based on the BSW model and based on the experimental determination of a_1 and a_2 give values of the branching ratio of $B \to J/\psi\ X$ decays:

$$\mathrm{BR}(B^- \to J/\psi\ K^-) = (1.1 \pm 0.6) \times 10^{-3} \tag{2.8}$$

$$\mathrm{BR}(B^0 \to J/\psi\ K^*) = (1.6 \pm 0.5) \times 10^{-3} \tag{2.9}$$

$$\mathrm{BR}(B_s^0 \to J/\psi\ \phi) = (1.4 \pm 0.4) \times 10^{-3} \tag{2.10}$$

$$\tag{2.11}$$

In the reconstruction of B^0, the K^* is expected to decay into $K^\pm\pi^\mp$ roughly 66% of the time. In reconstructing B_s^0, the ϕ is expected to decay into K^+K^- 50% of the time.

In short, neglecting differences in acceptance and efficiency for reconstructing the various B mesons (the subject of future work) and assuming the branching ratios of the decays are equal, one would expect to find roughly 2/3 the number of B^0 relative to B^- (because of the K^* decay branching ratio) and to find roughly 1/5 the number of B_s^0 to B^- (because of the fragmentation differences and the branching ratio of the ϕ).

2.4 Meson Mass

The masses of B mesons are of interest because they are composed of a heavy (the b) and a light (the u, d, or s) quark/antiquark pair. The heavy-light system

allows calculations that use a nonrelativistic approximation for the heavy quark and a fully relativistic approximations for the light quark. In the heavy-light system, study of the meson mass sheds light about the form of the QCD potential which binds the heavy and light quark together. A simple approach for predicting the mass of the B_s^0 comes from adding the mass difference between the D_s and D mesons to the B^- mass. Deviations of the true mass from this first approximation depend upon how parameters of the Quark Model scale from the charm system to the bottom system.

In the short-distance approximation, the QCD potential takes the following form in analogy with quantum electrodynamics (the factor $\frac{4}{3}$ is a color factor):

$$\mathrm{V(r)} = -\frac{4}{3}\frac{\alpha_\mathrm{s}(\mathrm{r})}{\mathrm{r}} \tag{2.12}$$

The two quarks can exist with states of zero angular momentum (pseudoscalar) or one unit of angular momentum (vector). A hyperfine splitting term giving the energy difference between these states [29] can be written as:

$$\mathrm{E_{HFS}} = \frac{8\pi}{3}\frac{3\alpha_\mathrm{s}}{3}\frac{|\Psi(0)|^2}{m_b m_q} < \mathrm{S}_b \cdot \mathrm{S}_q > \tag{2.13}$$

where $|\Psi(0)|^2$ is the square of the wave function at the origin, m_q is the mass of the quark, and $< \mathrm{S}_b \cdot \mathrm{S}_q >$ is equal to 1 (3) for pseudoscalar (vector) mesons. The mass of a B meson can thus be written as:

$$m_{bq} = m_b + m_q + \epsilon + \mathrm{E_{HFS}} \tag{2.14}$$

where ϵ represents the binding energy. Thus, measurements of the meson masses give insight into the constituent quark masses, the binding energy term, the QCD potential, the wave function at the origin, etc. The binding energy and the wave function at the origin are expected to scale with the reduced mass of the heavy and light quarks. Nominal quark masses are $m_u \sim m_d \sim 0.3$ GeV/c^2, $m_s \sim 0.5$ and $m_b \sim 5.0$ GeV/c^2.

Quark Model

The Quark Model allows for phenomenological predictions of the B_s^0 meson mass. One paper [30] uses three approaches to estimate the B_s^0 mass. In the first, the vector meson mass is equal to the sum of the two quark masses plus a term consisting of a parameterized expression (two parameterization are used) in reduced mass, μ:

$$\text{(a) } \mathrm{E}(\mu) = \mathrm{A} + \mathrm{B}\mu + \mathrm{C}\mu^2 \tag{2.15}$$

$$\text{(b) } \mathrm{E}(\mu) = (\mathrm{A} + \mathrm{B}\mu)/(1 + \mathrm{C}\mu) \tag{2.16}$$

Known vector meson masses (ρ, K^*, D^*, D_s^*, J/ψ, B^*, and Υ) are used to fit for the B and C parameters for given values of the A parameter. Minima for the fit parameters are found which give the best agreement for the known vector meson masses. This approach predicts a B_s^{0*} (vector state of a B_s^0 meson) with a spread of 15 MeV/c^2. A second approach uses a specific form of the QCD potential:

$$\mathrm{V(r)} = \mathrm{C} \log \left(\frac{\mathrm{r}}{\mathrm{r}_0} \right) \tag{2.17}$$

Fitting to the known masses gives a value for C of 824^{+176}_{-124} MeV/c^2 which provides an estimate of the B_s^{0*} to within 10 MeV/c^2. In the third approach, the Feynman-Hellmann theorem [31] is used to make a prediction also at the 10 MeV/c^2 level. All three approaches give a mass estimate for B_s^{0*} of approximately 5410 MeV/c^2. Assuming the hyperfine splitting for the B_s^0 mesons to be between 45 and 55 MeV/c^2, the predicted value of the B_s^0 mass is between 5345 and 5388 MeV/c^2. Other Quark Model based predictions [32] predict similar masses as summarized in Table 2.1.

Lattice QCD

Calculations involving lattice QCD are performed numerically. In the case of a heavy-light quark/antiquark system, the approximation of a fixed b quark bound to a relativistic light quark provides many tests of the model. In particular, lattice calculations have been shown to agree very well with those of a nonrelativistic Quark Model applicable to the study of mesons where both quarks are heavy. Current agreement with results in heavy-light systems suggest that the QCD potential in the Quark Model can be used reliably in lattice calculations. However, in the lattice calculations, systematic uncertainties arise due to the geometry of the lattice used in the calculation. Recent methods which involve a multistate smearing technique [33] to smooth out aspects of the discreteness of the lattice allow for greater confidence in the lattice calculation of the mass difference between the B^- and B_s^0 masses. The results are included in Tab. 2.1. The spread in the theoretical predictions 40 MeV/c^2 which sets the scale for this thesis in terms of making a useful measurement.

2.5 Current Evidence for B_s^0 and its Mass

Indirect evidence of the existence of the B_s^0 meson is obtained by observing a non-B^0 component in studies where a neutral B meson undergoes a mixing transition and becomes an anti-B [34]. Further evidence comes from the observation of correlated D_s with high-P_T leptons (the expected semileptonic decay of a B_s^0

Theoretical Model	M(B_s^0) (MeV/c^2) Prediction
M(B^-) + M(D_s) - M(D)	5378
Kwong and Rosner	5345 - 5388
Godfrey and Isgur	5360
Martin	5354 - 5374
Duncan, Eichten, *et al.*	5348 - 5367 (assuming M(B) = 5280)

Table 2.1: Summary of theoretical predictions of the mass of the B_s^0 meson.

meson) [35]. These indirect observations involve semileptonic decays with a missing neutrino such that a mass determination of the B_s^0 is difficult. The first experimental attempt at a B_s^0 mass determination involved measuring the energy spectra of photons emitted from an admixture of $B_{u,d}^*$ and B_s^{0*} decays at the Υ(5S) [36]. The component of the photon spectra coming from B_s^{0*} is expected to be more energetic and to undergo larger Doppler broadening than the lighter B mesons. In a multidimensional fit of B_s^0 meson mass and fraction of B_s^0 relative to the lighter B mesons, two solutions are found for M(B_s^0): 5363 $\pm$ 3 MeV/c^2 or 5401 $\pm$ 9 MeV/c^2 (assuming M(B)=5280 MeV/c^2). At LEP, a handful of fully reconstructed B_s^0 [37, 38] candidates have recently been found in modes involving D_s or J/ψ. The most precise determination of the B_s^0 mass at LEP comes from two candidates [38] of which one of the type $B_s^0 \to \psi(2S)\ \phi$ dominates the measurement: 5368.4 $\pm$ 5.6 $\pm$ 1.5 MeV/c^2. CDF published a B_s^0 mass measurement [39] of 5383.3 $\pm$ 4.5 $\pm$ 5.0 MeV/c^2 based on a sample of 14.0 $\pm$ 4.7 events reconstructed using 11 pb^{-1} of data. This thesis updates the CDF measurement using the entire 19.3 pb^{-1} of data. For this analysis the data has been reprocessed using better determined calibration constants and track reconstruction algorithms.

Chapter 3

CDF Detector

This chapter will describe the experiment used to obtain the data for this analysis. This description includes the steps involved in producing $\overline{p}p$ collisions at energy $\sqrt{s} = 1.8$ TeV. The CDF detector will be described with particular emphasis on those subcomponents most relevant for this analysis. This includes the tracking system and muon systems. An important section is a description of the dimuon J/ψ trigger which allows an enriched sample of events containing $J/\psi \rightarrow \mu^+ \mu^-$ decays to be recorded. It is these events which are used to select the final data sample for this analysis as described in the next chapter.

3.1 Fermi National Accelerator Laboratory

The Fermi National Accelerator Laboratory (FNAL) provides proton-antiproton collisions at a center of mass energy of 1.8 TeV. The process of producing these collisions begins by ionizing hydrogen gas and accelerating the H^- ions to 750 KeV in an electrostatic accelerator, the Cockcroft-Walton. From here the negative hydrogen ions are accelerated to 200 MeV in a linear accelerator. At the end of the linear accelerator, the ions pass through a carbon foil which strips the outer electrons leaving only protons. These protons are stored in the Booster Ring, a synchrotron accelerator, that raises the energy to 8 GeV. In the booster, proton bunches are collected and injected into the Main Ring which is also a synchrotron. The Main Ring consists of four miles of alternating sections of dipole bending and quadrupole focusing magnets. A section of the ring contains RF cavities which boosts the proton energy to 150 GeV. The Main Ring can then send these high energy protons to fixed target experimental areas or to the Fermilab Tevatron. During $\overline{p}p$ collider activity, protons are removed from the Main Ring and focused on a long beryllium target which produces many secondary particles including antiprotons. The antiprotons are selected by magnets and stored in the Accumulator ring. After sufficient numbers of antiprotons are stored, they

are reinjected first into the Main Ring and then into the Tevatron where they are accelerated and then collide with protons. Figure 3.1 shows a schematic representation of the layout at Fermilab.

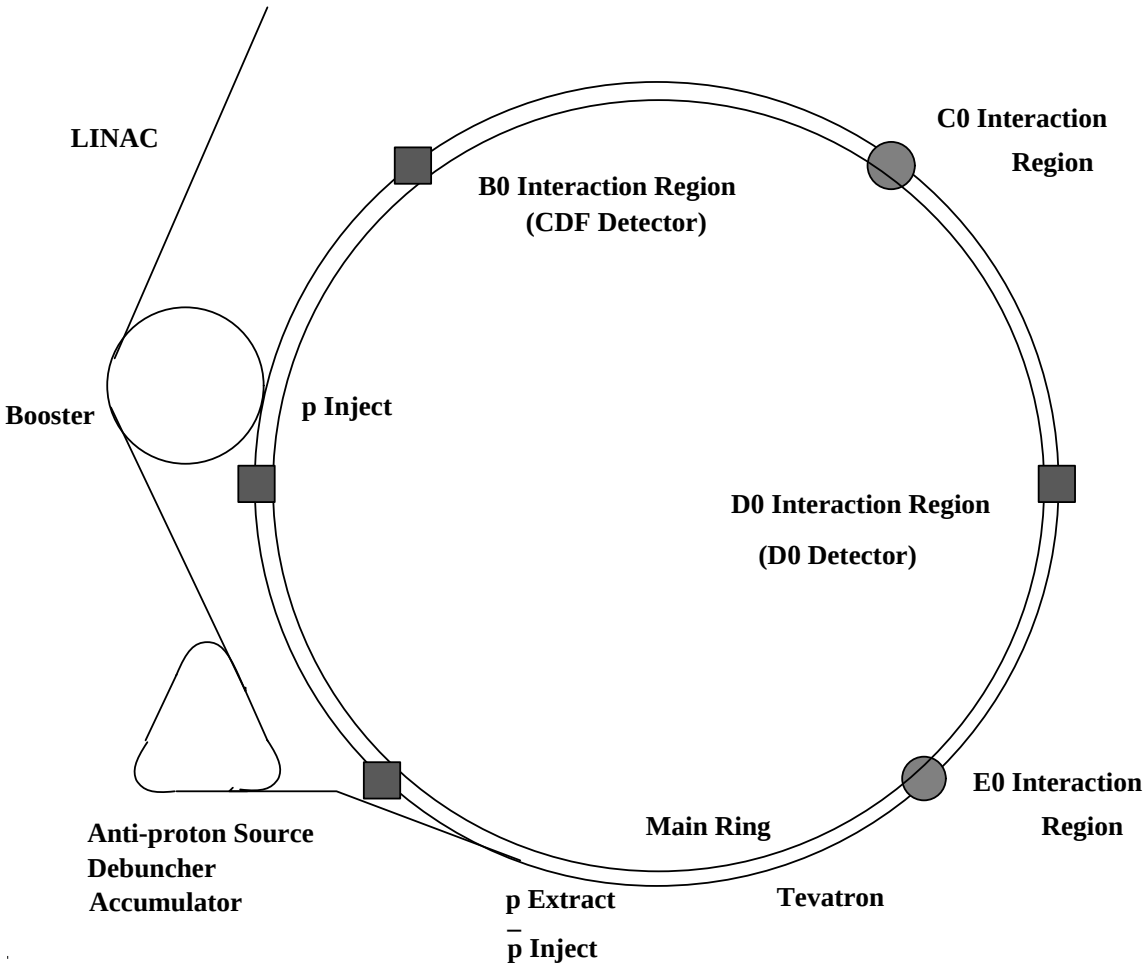

Figure 3.1: Layout of Fermilab

3.1.1 Tevatron

The Tevatron is an accelerator ring which sits beneath the Main Ring. It consists of superconducting magnets. Normal operation of the Tevatron is to accelerate protons and antiprotons to 900 GeV. In fixed target operation, the protons are sent to the fixed target experimental areas. In collider operation, protons and antiprotons are accelerated simultaneously and collide at regions where strong focusing magnets exist.

3.1.2 B0 Interaction Region

The instantaneous luminosity of the Tevatron during $\overline{p}p$ collisions can be calculated using Eq. 3.1:

$$\mathcal{L} = \frac{\mathrm{N_p N_{\overline{p}} f}}{\triangle \pi \sigma_{\S} \sigma_{\dagger}} \tag{3.1}$$

where N_p and $\mathrm{N}_{\overline{p}}$ are the number of protons and antiprotons in a bunch, f is the collision frequency, and σ_x and σ_y are the major and minor axis of the elliptical cross section of the beam profile at the interaction point. The interaction region for the CDF experiment is at B0 (see Fig. 3.1). Quadrupole magnets focus the beam so that its shape at the center of the CDF detector is roughly circular in cross section with a radius defined by one σ of 40 μm. The longitudinal extent of the interaction region is approximately Gaussian with a width of 30 cm. In a typical store, six bunches of 12×10^{10} protons collide with six bunches of 3×10^{10} antiprotons every 3.5 μs. Filling in these typical numbers into Eq. 3.1, one derives a typical instantaneous luminosity of 5×10^{30} cm^{2}s^{-1} at CDF.

3.2 CDF Detector

Centered about the B0 interaction region of the Tevatron is the CDF detector. CDF is a multipurpose detector consisting of tracking, calorimetry and muon subsystems. Tracking is restricted to the central part of the detector. The CDF tracking system achieves excellent resolution due to a high solenoidal magnetic field of 14.1 KG and large volume. The muon system consists of drift chambers to record position information for charged particles which are not absorbed in the calorimeters. The calorimetry systems consist of towers of alternating absorber and scintillator which point back to the nominal interaction vertex for energy measurements of both electromagnetic and hadronic showers. Figure 3.2 shows the representation of the CDF detector and its coordinate system [40]. The CDF coordinate system has the z-axis along the proton beam direction, the x-axis pointing away from the center of the Tevatron, and the y-axis pointing up. A useful geometric parameter is the pseudorapidity defined as $\eta = -\ln[\tan(\theta/2)]$ because particle production is roughly uniform in pseudorapidity. Figure 3.3 is another representation of the CDF detector giving a full 3D perspective.

3.2.1 Tracking

The tracking system is used to provide position information of charged particles along their helical trajectories in the solenoidal magnetic field. In addition, the absence of a track matched to an electromagnetic calorimeter cluster aids in the identification of photons. The primary components of the tracking system include

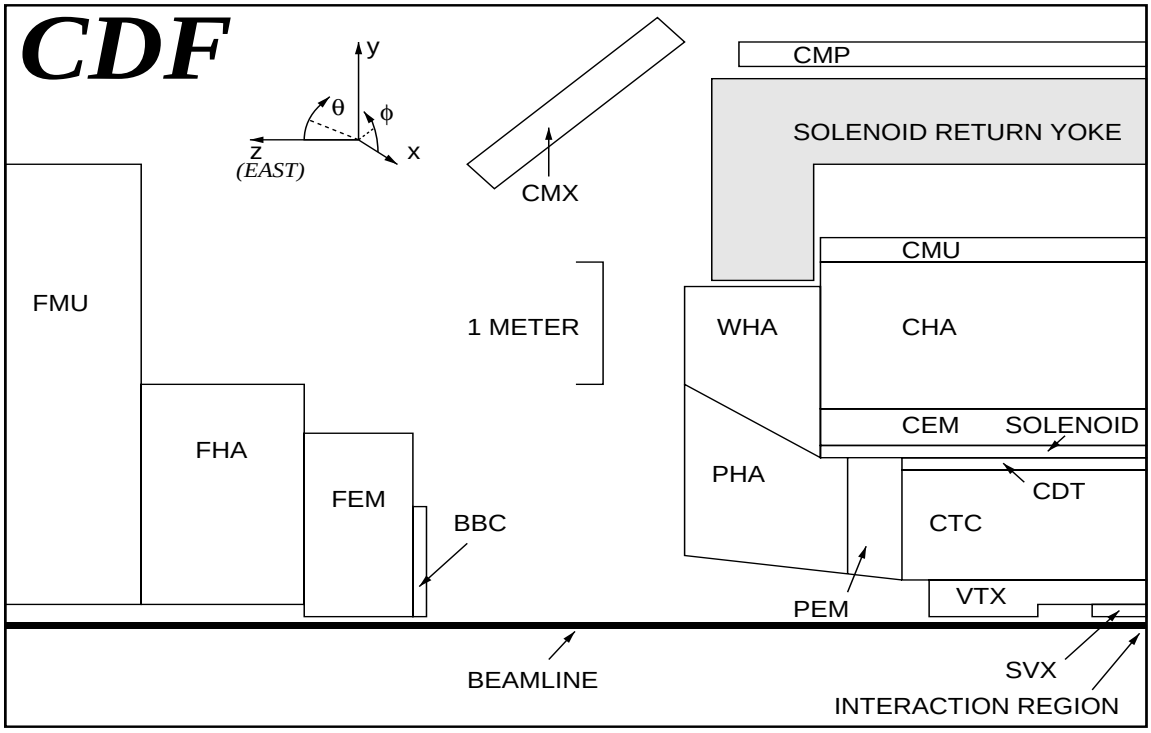

Figure 3.2: Side view representation of the CDF detector used in the 1992–1993 run.

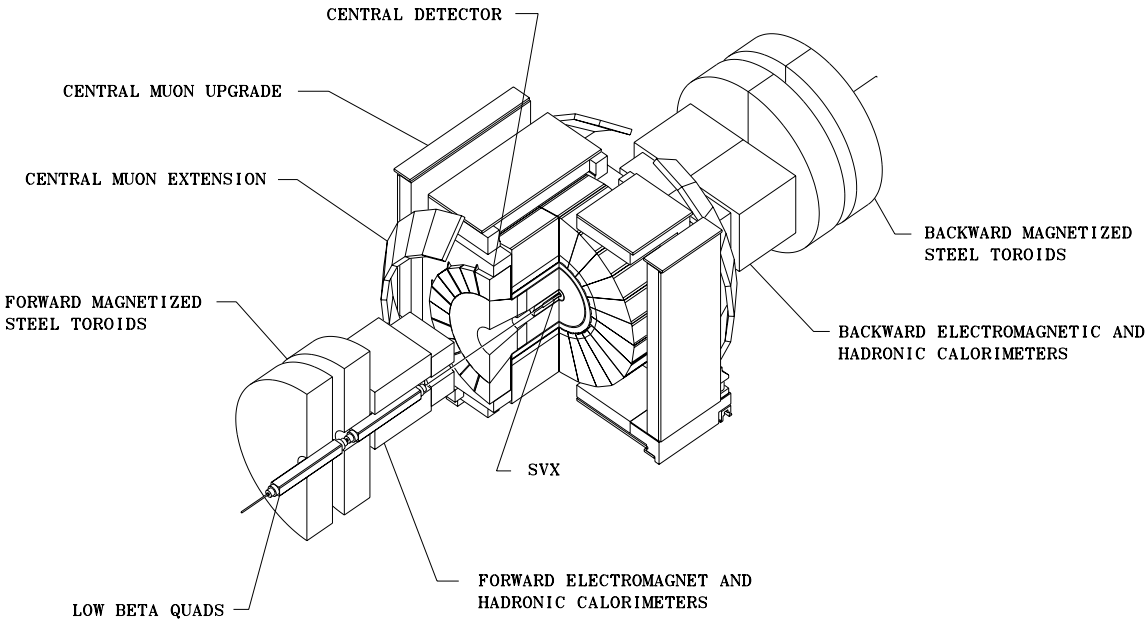

Figure 3.3: Representation of the CDF detector used in the 1992–1993 run.

the solenoid, a silicon microstrip vertex detector (SVX), a vertex time projection chamber (VTX), and the central tracking chamber (CTC). Each of these subsystems is discussed below.

Solenoid

The CDF solenoid magnet coil provides an axial magnetic field within a volume of 3 m in diameter and 4.5 m in length. The magnet consists of NbTi/Cu superconductor. During normal operation, a current of 4650 amps flows resulting in a magnetic field of 14.1 KG in the tracking volume. The magnetic field flux is returned through a steel yoke which supports the calorimeters. A precision mapping of the field has been performed [41]. For this analysis, the high axial field improves the momentum and hence mass resolution for reconstructing B decays. Some non-uniformities in the field do contribute to the systematic uncertainty of mass measurements as will be discussed later.

SVX

The silicon vertex detector, SVX [42], was installed in early 1992 as part of the upgrade for the data taking on which this dissertation is based. It is the innermost tracking element consisting of silicon microstrip detectors which surround the beam pipe and is surrounded by the VTX detector. It provides precise tracking in the r-ϕ plane in order to obtain a measurement of the impact parameter of traversing particles. The SVX is segmented into two halves, barrels, which sit side-by-side on either side of the nominal interaction region. Each barrel is composed of 12 wedges each of which cover 30 degrees in azimuth. Figure 3.4 shows schematically several features of the SVX barrel. Each end of each barrel has a precision machined beryllium bulkhead support structure. Beryllium is used to minimize radiation interaction lengths while providing support for the silicon detectors. Precision placement with an accuracy of 10 μm [43] in r-ϕ within a SVX wedge results in excellent internal alignment. Further improvement in alignment constants can be derived from physics data. Mounted to the readout end of the bulkhead which is closest to the nominal interaction region are cooling tubes through which chilled water flows to remove heat generated by the readout electronics. Typical operating temperature for the silicon is 20°C [42]. The ear cards and port cards are thick film multilayered hybrid circuit boards which are part of the readout system discussed below. In Fig. 3.4, the wedge structure of four layers of silicon detectors can be seen.

Each wedge consists of 4 layers of 280 μm thick silicon strip detectors. Each layer contains the fundamental detector unit called a ladder. Figure 3.5 shows a schematic representation of a ladder. A ladder consists of three 8.5 cm long rectangular silicon strip detectors laid end-to-end with wirebond connections joining

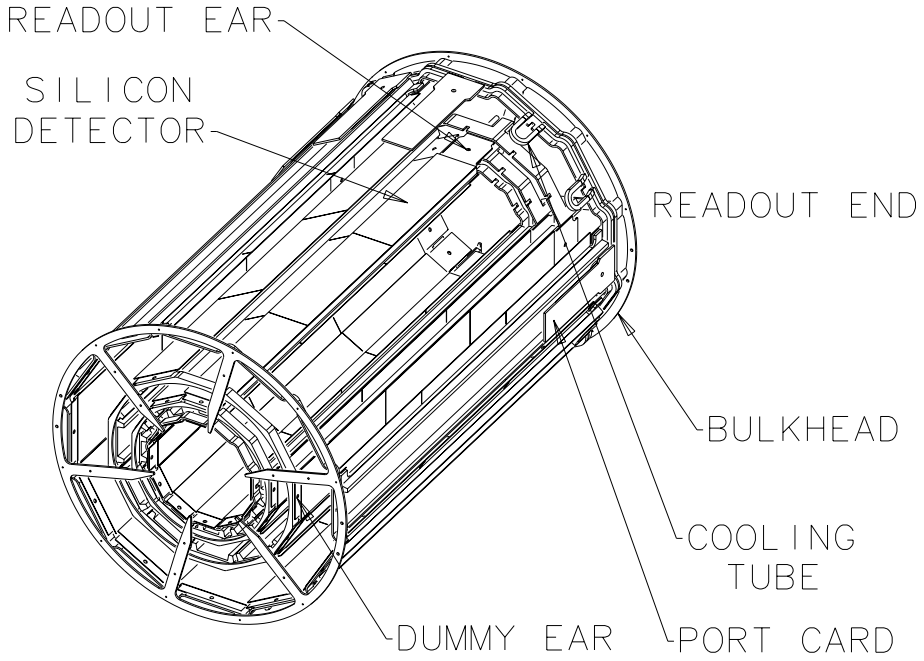

Figure 3.4: Schematic representation of a SVX barrel.

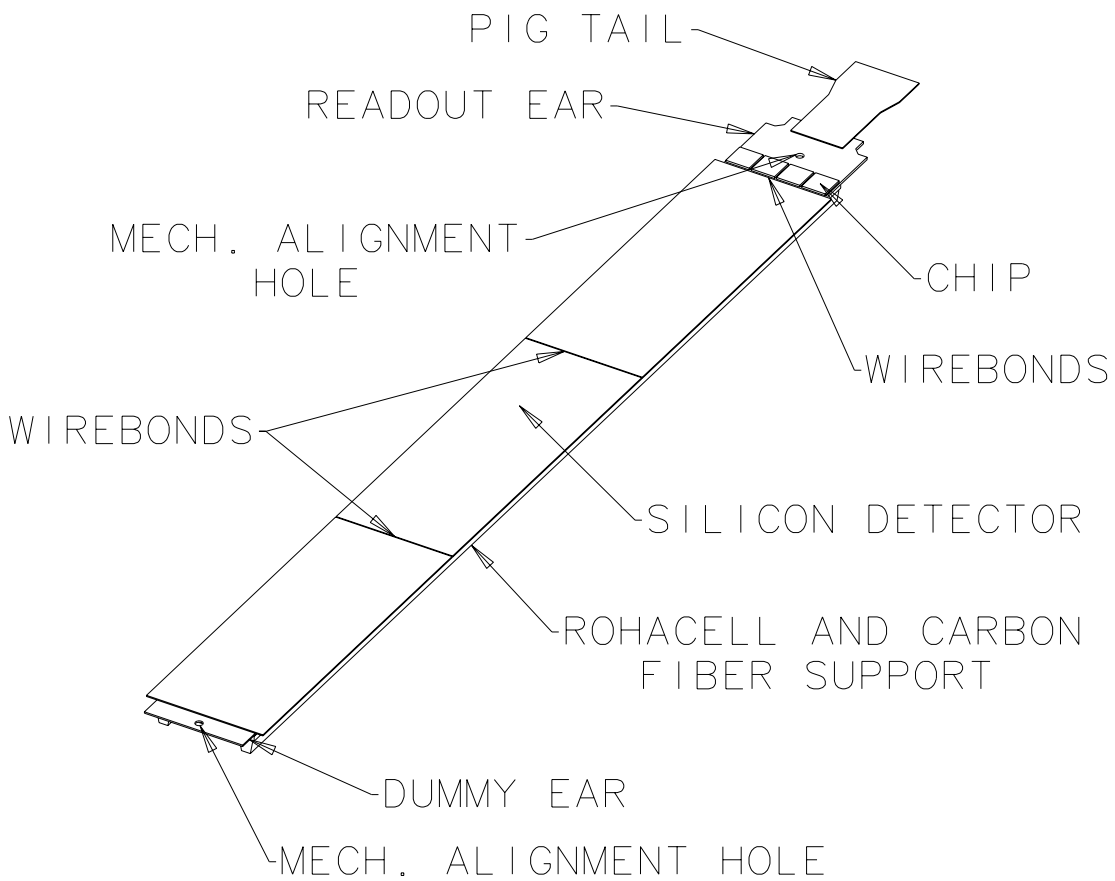

Figure 3.5: Schematic representation of a SVX ladder.

the corresponding strips of one detector to the next, resulting in strips with an effective length of 25 cm. Thus, both barrels of the SVX give an active length which subtends 50 cm along the beam axis. The strips are in turn wirebonded to the SVX readout chips which are mounted on the ear card. The silicon detectors and the ear cards are supported on lightweight rohacell with carbon fiber support. An optimization to minimize the amount of material used while providing rigid and stable support led to the choice of these materials. The dummy ear consists of a passive gold film electrically connected to ground to which unuseable strips with very high leakage currents can be connected to minimize the effect on neighboring strips [42]. Ladders of different layers have different characteristics as shown in Table 3.1. Layer 0 and Layer 3 have the active silicon facing towards the beam pipe while Layer 1 and Layer 2 face outward. This was done so as to make position measurements as close as possible to the beam pipe.

Layer	Face	Radius [cm]	Tot. Width [cm]	Act. Width [cm]	Pitch [μm]	Num Strips	Num Chips
0	IN	2.9899	1.6040	1.536	60	256	2
1	OUT	4.2710	2.3720	2.304	60	384	3
2	OUT	5.7022	3.1400	3.072	60	512	4
3	IN	7.8508	4.2925	4.224	55	768	6

Table 3.1: Characteristics of each SVX layer.

The SVX readout chip is the central component for converting charge deposited on a silicon strip to an electrical signal which can be recorded. Each SVX chip consists of 128 channels of amplifiers and storage capacitors. Each channel is connected to a calibration capacitor upon which a threshold charge can be stored. In "sparse" mode operation, only those channels with a signal charge exceeding the calibration threshold charge will be read out. Sparsification is critical to reading out the SVX within approximately 2 ms as required by the Level 2 trigger to be discussed later in this chapter. The SVX chip is also able to collect charge on each strip twice, once in time with the beam crossing and once out of time. In each charge integration, the analog level is sampled twice. This "quadrupole" sampling scheme allows for subtraction of charge collected by the chip due to leakage currents within the bulk of the silicon detectors. The chip responds to clocking control signals which reset various amplifier stages and storage capacitors. The SVX stores the leakage-current subtracted charge collected on those strips which are likely to have been hit by a traversing particle since the charge is above the noise threshold. By reading out the channel address and the analog charge information, the r-ϕ position of a charged particle passing through the SVX can be recorded and combined with information from the other layers. The impact parameter resolution of high P_T tracks is 17 μm and the r-ϕ position

resolution is 13 μm [42].

Each wedge functions as an independent readout unit consisting of 1920 channels. With 12 wedges per barrel and 2 barrels, the total channel count of the SVX detector is 46,080. During operation, typically 98% of the channels were functioning. The readout chips of a wedge are connected in series. Each ear card has a common bus for clocking control of the chips and for readout to the data acquisition system. This bus is present on the pig-tail copper-on-kapton cable connected to each ear card. Each of the four pig-tails from each layer is connected to another copper-on-kapton cable called the "mother cable". The mother cable connects the bus to the port card. The port card is a multilayered thick film circuit board which functions to drive the signals between the SVX chips and the data acquisition electronics. The port card suppresses noise by sending both analog and digital signals differentially. On board voltage regulators provide a stable power source for the SVX readout chip. Crates mounted on the outside of the CDF detector contain FASTBUS modules which communicate to the port card through small coaxial cable and copper-on-kapton cable. These Digitizer modules are responsible for digitizing the analog readout of the SVX chips and for passing the information between the port card and another FASTBUS module, the Sequencer. The Sequencer is a programmable module which generates the SVX clocking signals. It receives information from the Digitizers and passes that information to the CDF data acquisition system so that SVX information can be added to the data record.

The SVX has operated successfully in the hadron collider environment of CDF. This analysis makes use of SVX information when it is available for a given track. By combining SVX hit information with a given CTC track, improvements in the helical track parameters are obtained. In particular, the excellent impact parameter resolution obtained by using SVX information provides an additional and very valuable handle for studying particles which have a lifetime of order a picosecond. By adding precise tracking measurements close to the beam axis, the rejection power is enhanced when selecting candidate B mesons consisting of track combinations consistent with originating from a displaced secondary vertex. This enhancement will be quantified in later chapters. Further improvement is also made in the curvature and ϕ_0 measurements after adding SVX information.

VTX

The vertex time projection chamber, VTX, is a new addition to the upgraded CDF detector for the 1992–1993 run. It provides tracking information in the r-z plane. The chamber replaces a similar detector used in previous CDF data taking [44]. The VTX is divided into an east and a west half each surrounding a SVX barrel. Each half of the VTX is composed of 28 octagonal modules which cover out to 22 cm in radius and to $|\eta| < 3.25$. The 18 modules which surround the

SVX contain 16 sense wires strung in the r-ϕ plane perpendicular to a radial line extending from the origin. Ten additional modules with 24 sense wires are located at larger z. The drift gap in the argon-ethane atmosphere to the sense wires is 4 cm. Adjacent modules are rotated by 11.3° in ϕ so that CTC r-ϕ track segments can be better matched to the VTX segments.

For this analysis, the primary use of VTX information is to provide a measurement of the z coordinate of the primary event vertex to check the value obtained from r-z measurements using CTC information.

CTC

The central tracking chamber [45], CTC, is a cylindrical wire tracking chamber which extends from outside the VTX to inside the solenoidal magnet covering out to pseudorapidity of 1.1. Table 3.2 lists some of the mechanical parameters associated with the CTC. There are a total of 84 sense wire layers arranged in nine superlayers. Five of these superlayers have wires aligned parallel to the beam axis. Between each pair of these axial superlayers are a set of wires with a $\pm 3°$ tilt to the beam axis in order to provide stereo information. Figure 3.6 shows a view of the CTC end plate which highlights the superlayer arrangement. Hits on the CTC wires are matched to tracks and a fit is performed to measure the five helical track parameters. Within each layer, groups of sense wires and field shaping wires form cells which are tilted at 45° with respect to the radial direction. The tilt angle of 45° is used to compensate for the Lorentz angle so that the drift trajectories are axial and the time-to-distance relationship is linear. In addition, the compactification obtained with a 45° tilt is such that a particle with $P_T > 2.5$ GeV/c will pass close to at least one sense wire in each superlayer, resulting in a fast pulse to be used by the central fast tracker (CFT) in the trigger to be discussed below.

This analysis relies on the CTC measurements. Its performance will be described later by showing a number of known mass peaks and comparing fitted values with the corresponding world average measurements. Particle momenta are derived from the track parameters obtained using the CTC hit information. Excellent momentum resolution, as listed in Table 3.2, is achieved because both the tracking volume and the magnetic field strength are large. Constrained fits are used in this analysis to further improve the momentum resolution.

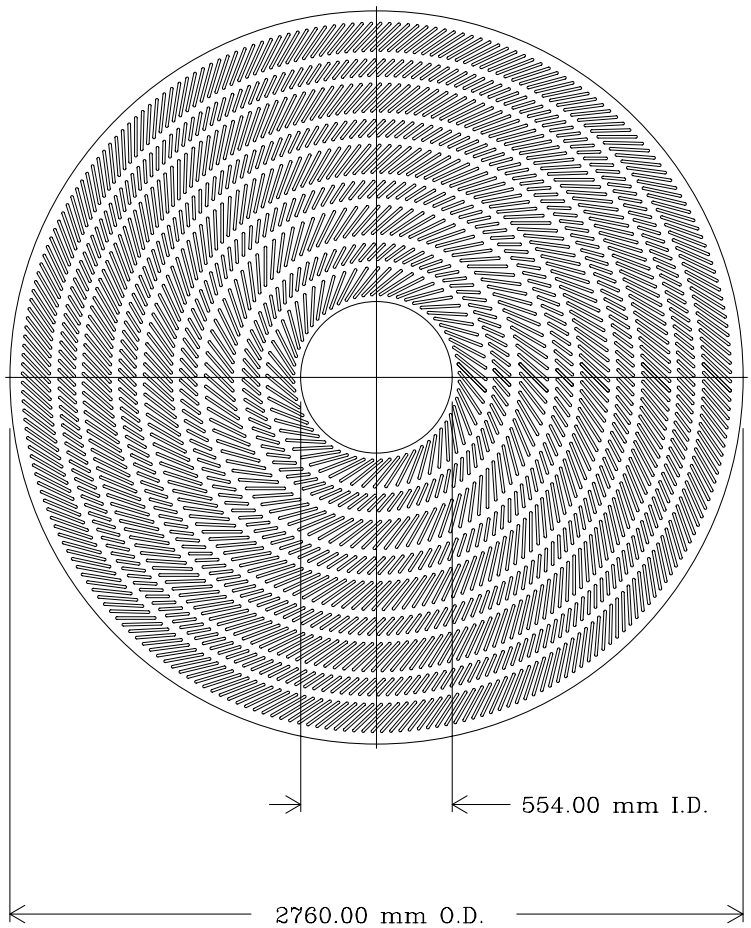

Figure 3.6: View of the CTC end plate showing the superlayer structure of the drift cells.

Number of layers	84
Number of superlayers	9
Stereo angle for each superlayer	0°, +3°, 0°, -3°, 0°, +3°, 0°, -3°, 0°
Number of super cells per layer	30, 42, 48, 60, 72, 84, 96, 108, 120
Number of sense wires per cell	12, 6, 12, 6, 12, 6, 12, 6, 12
Sense wire spacing	0.1 cm
Tilt angle	45°
Radius at innermost sense wire	30.9 cm
Radius at outermost sense wire	132.0 cm
Wire length	321.4 cm
Electric Field	1350 V/cm
Magnetic Field	14.1 KG
Nominal r-ϕspatial resolution	200 μm
Nominal r-$z$spatial resolution	.6 cm
Nominal $\delta P_T/P_T$	.002 $\times$ P_T(GeV/c)
Nominal $\delta P_T/P_T$(beam constrained)	.0011 $\times$ P_T(GeV/c)

Table 3.2: CTC mechanical parameters.

3.2.2 Muon Systems

The CDF muon system is instrumental in this analysis because it allows for the identification of muons in events containing J/$\psi \rightarrow \mu^+ \mu^-$ decay. The muon system also provides fast signals which can be used in the trigger system to distinguish J/ψ events from enormous backgrounds due to all other QCD processes. The CDF muon system consists of three different detector subsystems which are discussed below. Included are two subsystems which were part of the upgrade for the 1992–1993 run.

CMU

The central muon system [46], CMU, provides muon identification and measurement out to $|\eta|$ of 0.6. The CMU consists of wire chambers embedded in the CDF calorimeters after five absorption lengths. The thickness of the calorimeter makes it unlikely that a muon with P_T below 1.4 GeV/c would reach the muon chambers. The arrangement of the muon chambers within the calorimeter wedge is shown in Fig. 3.7 where three muon towers subtend 12.6° in ϕ in each 15° central calorimeter wedge. The total coverage in ϕ is 85%. The chambers extend 226.0 cm along the z-axis. Each tower consists of four layers as shown in Fig. 3.8. Sense wires in each cell are slightly staggered to allow chamber readout to be ganged together while allowing for unambiguous hit association. Timing information is

used in the trigger. The slope of the muon track segment is obtained by taking the larger of $t_4 - t_2$ and $t_3 - t_1$. This time difference gives an estimate of the P_T of the track which is used in the trigger decision. The timing information gives an r-ϕ position measurement and charge division provides an r-z position measurement. Both of these positions can be compared to the position obtained from extrapolating a track found in the CTC to the muon chambers. In this manner, muon track segments may be matched to CTC tracks resulting in a well measured and identified muon candidate.

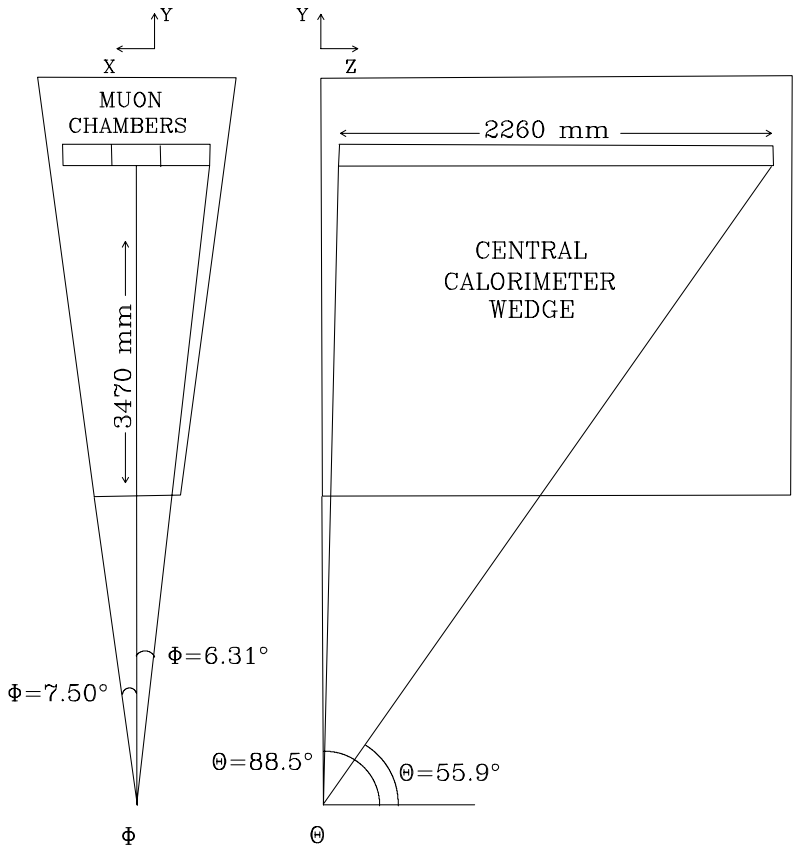

Figure 3.7: Arrangement of central muon chambers within a calorimeter wedge.

CMP

Since the calorimeters have only five absorption lengths of material, hadrons that do not shower in the calorimeter can "punch-through" and leave hits in the muon chambers. The central upgrade chamber, CMP, provides additional muon chambers behind steel shielding resulting in a total of 8 absorption lengths. Only muons with P_T above 2.5 GeV/c are expected to be able to reach the CMP chambers. The purity of real muons is larger when CMP confirmation is required for muon

Figure 3.8: Four layers of a central muon chamber tower.

candidates that leave hits only in the CMU system. Hadronic punch-through is unlikely to pass through roughly eight absorption lengths. The CMP covers the pseudorapidity range of $|\eta| < 0.6$ and covers 80% in ϕ. This analysis makes use of the small additional coverage of the CMP which is not covered by the CMU – notably the ϕ gaps between calorimeter wedges are sometimes covered only by CMP chambers. CMP confirmation of a CMU hit in the overlap region is not required since the muons from $J/\psi \rightarrow \mu^+ \mu^-$ decays have P_T often less than 2.5 GeV/c.

CMX

Another upgrade in the CDF muon system is the addition of the central extension chambers, CMX, which cover the $|\eta|$ range between 0.6 and 1. Coverage in ϕ during the 1992–1993 CDF run was 80% and the chambers were located behind $\sim$ 6 absorption lengths of calorimeter. During the early part of the run, noise hits from the scattering of particles off the beam pipe and forward calorimeter resulted in a rate which prevented full utilization of the CMX in the trigger. A new beam pipe with less material was inserted mid-run to reduce the noise hits and the trigger requirements for CMX muons were relaxed somewhat. Approximately 20% of the recorded J/ψs contained a CMX muon.

3.2.3 Calorimetry

Calorimetry information was not used directly in this analysis other than to aid in muon identification. The CDF calorimetery system consists of the central electromagnetic and hadronic calorimeters (CEM and CHA) which cover to $|\eta|$ of 0.8. The endwall (WHA) covers from $|\eta|$ of 0.6 to 1.3. These calorimeters consist of steel and scintillator. Plug calorimeters (PEM and PHA) and forward calorimeters (FEM and FHA) are gas calorimeters which provide coverage from $|\eta|$ between 1.3 and 2.4 and 2.4 to roughly 4 respectively. The CDF calorimeters are highly segmented into towers which point back to the nominal interaction point.

Since most muons are minimum ionizing, they are expected to deposit a small amount of energy within the calorimeter as it traverses. Muons from decays-in-flight (i.e. $K \rightarrow \mu\nu_\mu$) are likely to have the muon direction different from the K direction resulting in energy deposition in the calorimeter tower different from the one pointing to the muon hits. Muon backgrounds from hadronic punch-through are often accompanied by a large amount of energy in the calorimeter tower pointing to the hit muon chamber. Requirements on the energy deposition in the calorimeter tower can improve the purity of the muon sample as will be shown later.

3.3 Trigger System

This analysis and any B physics measurement in a hadron collider environment relies on the ability to trigger effectively on events which are of interest. At CDF, $\overline{p}p$ collisions take place every 3.5 μs or close to 300,000 collisions per second. Data is able to be recorded at a rate of 5 events per second. It is the job of the trigger system to reduce the total event rate to a rate at which events can be recorded while being efficient for the most interesting events. This analysis uses the dimuon trigger to select events with $J/\psi \rightarrow \mu^+ \mu^-$ decay. The CDF trigger system consists of three levels of triggering for filtering events. This section will first give an overview of the CDF data acquisition system followed by a description of the three trigger levels.

3.3.1 Data Acquisition

Detector elements are attached to front end electronics which send signals to digitization modules for assembly into a CDF event record. Some specifics of the data acquisition system for the SVX are discussed above. The front end electronics includes FASTBUS TDCs (Time to Digital Converter) to read out tracking and prompt muon data. These fast signals are used in the trigger decision. Other front end modules, RABBIT cards, are mounted on the detector and are used to read out calorimeter and the muon drift chamber information. These front end systems are connected to digitization modules SSPs and MX scanners which include some processing such as formatting and adding in header information. Data is then collected by an event builder which sorts data at a rate of $\sim$ 30 Hz. The average event size assembled by the event builder is $\sim$ 200 KB. After passing the Level 3 trigger, the events are logged onto 8 mm computer tape at a rate of $\sim$ 5 Hz.

3.3.2 Level 1

The Level 1 trigger functions to filter the incoming 300 KHz event rate to 1 kHz while retaining events which have large amount of energy in the calorimeter, single high-P_T electrons or muons, or two low-P_T electrons or muons. Large energy showers in the calorimeter potentially due to high-P_T electrons and photons are identified by single towers which have an energy typically above a threshold of 8 GeV/c. High-P_T muons are found by requiring hits in the muon chambers with P_T above 6 GeV/c. Lower-P_T thresholds are placed on electrons and muons when they occur in pairs: pairs of 4 GeV/c electrons or a 4 GeV/c electron with a 3.3 GeV/c muon.

The low-P_T dimuon trigger requires two muon track segments with P_T larger

than 3.3 GeV/c. For most of the run, one of the muon segments had to be a CMU type muon because backgrounds in the CMX chambers caused too high a rate in Level 1. Some of the later data did allow two CMX muons to initiate the Level 1 trigger. In Fig. 3.9 the efficiency of the Level 1 trigger as a function of muon P_T is shown. For this study [61], J/ψ candidates that passed single muon triggers were studied as to whether the appropriate Level 1 bit was set. The gradual turn-on in the efficiency below the nominal threshold of 3.3 GeV/c gives some indication of the P_T resolution using only timing information in the muon chambers. Remaining background to be removed includes events where one or both candidate muons are noise or background hits in the muon chambers.

3.3.3 Level 2

The Level 2 trigger filters events to a rate of 12 Hz before being fed into Level 3 by removing backgrounds which pass Level 1 and making requirements on better defined thresholds. For calorimeter triggers, clusters of energy are required to be above thresholds as opposed to single towers. Electrons and photons are required to have mostly electromagnetic energy deposition in the calorimeter tower. Muon triggers require a match between a muon track segment and a track found by the fast tracking hardware processor. Low-P_T dilepton triggers also require a CFT track to match the electromagnetic cluster or muon stub. Other Level 2 triggers are specific for events with large missing energy or those which satisfy neural network algorithms. The CFT has a momentum resolution of $\frac{\delta P_T}{P_T} \sim 0.035 \times P_T$ (GeV/c) and has an efficiency of $93.5 \pm 0.3\%$ for isolated tracks with P_T above 10 GeV/c.

For the low-P_T dimuon triggers, the Level 2 trigger requirement is that one of the two muon stubs be matched to a CFT found track. For much of the run, the requirement was that if the dimuon involved a CMX muon, it had to have the CFT track matched to it. In addition, for some parts of the run, hadronic energy deposition in the calorimeter tower towards which the muon track pointed was required to be larger than 0.5 GeV as expected for a minimum ionizing particle. Figure 3.10 shows the Level 2 trigger efficiency versus muon P_T. The efficiency was determined by studying how often the second muon leg was matched to a CFT track when the first leg was responsible for the trigger [57]. Notice that there is a gradual turn-on between 2.4 and 3.2 GeV/c. Only one leg of the dimuon is required to pass the CFT requirement. Often, one of the two muon legs has a P_T less than the nominal threshold of 3 GeV/c.

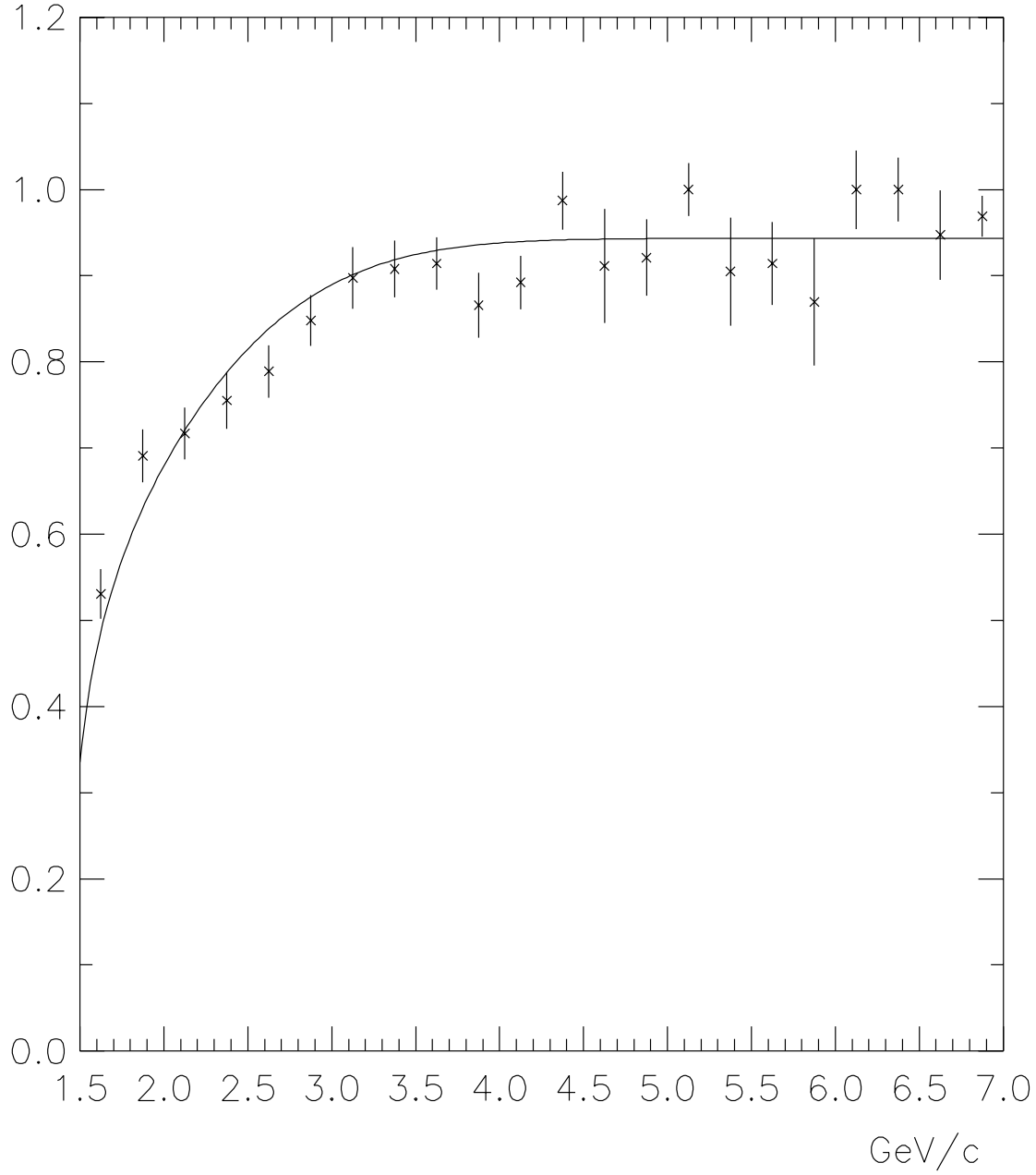

Figure 3.9: Level 1 dimuon trigger efficiency as a function of muon P_T.

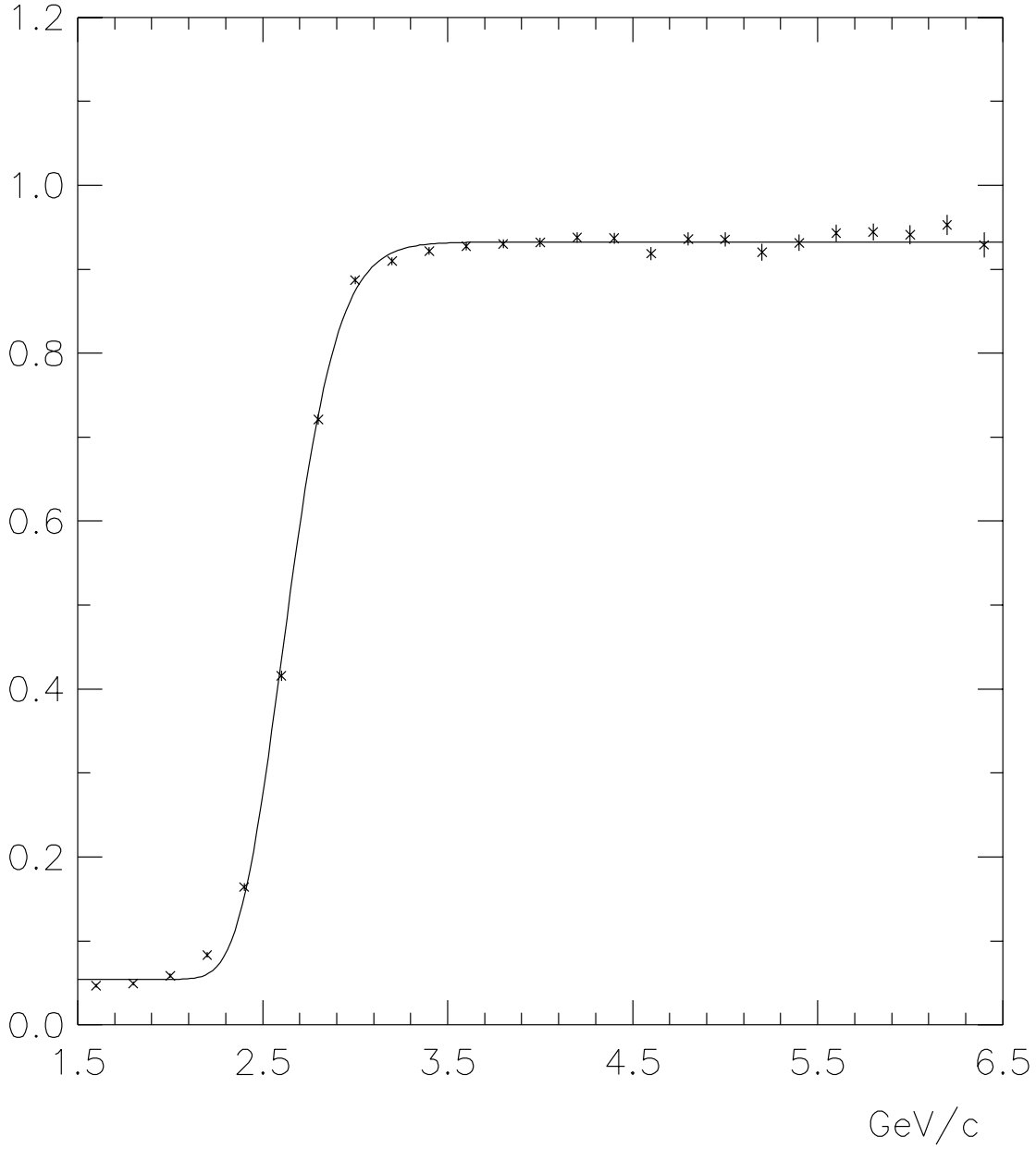

Figure 3.10: Level 2 dimuon trigger efficiency as a function of muon P_T.

3.3.4 Level 3

The Level 3 trigger reduces events to allow for 5 Hz data writing. In Level 3, full event reconstruction is performed in software and thresholds are much more sharply defined. Algorithms for clustering calorimetery energy are used to define jets which must pass certain transverse energy requirements. Photon candidates must pass low thresholds and be well isolated or pass higher thresholds and not necessarily be isolated. Muons must be well matched to a CTC track taking into account uncertainties in extrapolation due to multiple scattering. Electrons must have a track matched to the electromagnetic calorimeter cluster and must have a shower profile consistent with being an electron. Similar strategies are used for low-P_T electron and muon pairs. A number of other specialty triggers also exist in Level 3. The Level 3 dimuon J/ψ trigger passes a "Stream 2" trigger and is discussed below.

3.3.5 Stream 2

In Level 3, CDF separates approximately 10% of the most interesting events as defined by the different physics analysis groups into the Stream 2 path. These events were given priority in offline processing and data accessibility. The dimuon J/ψ trigger events were part of Stream 2.

In order to select events which pass the Level 2 dimuon trigger to include mostly $J/\psi \rightarrow \mu^+ \mu^-$candidates, the following requirements were made on the online processed events during the end of the run[1]:

- Two muon stubs of any type except CMP – CMX
- Two muons had opposite charge
- Invariant mass($\mu^+\mu^-$) between 2.8 and 3.4 GeV/c^2.
- Minimum muon P_T of 1.4 GeV/c.
- Matching between muons stubs and CTC tracks within 4 σ.

The Level 3 efficiency was derived from hand scanning events which were collected during the run where Level 3 was not required and from looking at dimuon candidates which passed other independent Level 3 triggers [48]. Both of these methods are consistent with a Level 3 efficiency of 97 $\pm$ 2 %.

Events which pass the dimuon J/ψ Stream 2 trigger are used as the data sample for this analysis. Specifics about this data sample are discussed in the next chapter.

[1]During the early part of the run, dimuons with a CMX muon had stricter requirements.

Chapter 4

Data Set

This chapter describes the data set which was used for this analysis. The data set is defined as the set of events which contains J/ψ candidates used to search for exclusive B meson decays. This data set is first put in the context of coming from a subset of the entire collection of events observed by CDF during the 1992–1993 run. A description of the offline event reconstruction follows. The emphasis of this chapter is on the final J/ψ selection.

4.1 Statistics of the 1992–1993 Run

The 1992–1993 CDF run recorded 19.3 pb^{-1} [49] of data to tape. The total cross section of $\overline{p}p$ collisions at $\sqrt{s} = 1.8$ TeV has been measured to be 80.03 ± 2.24 mb [50]. Thus, CDF "saw" a total of 2 quadrillion $\overline{p}p$ collisions. A total of 15.5 million events (approximately one out of every 100,000 collisions) passing a Level 3 trigger were recorded onto tape and were processed. From these events, a total of 1.7 million passed a Stream 2 trigger. All events which passed a Stream 2 trigger were processed using offline reconstruction code termed "Express Production" which is discussed in the next section. These Stream 2 events include 205,610 which passed the J/ψ Stream 2 triggers. Figure 4.1 shows the vertex constrained dimuon mass distribution for all dimuon combinations in events which pass the Stream 2 J/ψ trigger. The mass distribution is unscaled in that systematic corrections to dE/dx and the magnetic field which will be discussed in Chapter 7 have not been applied.

4.2 Express Production

The data acquisition system wrote raw event files of the Stream 2 events onto 8 mm tapes. These tapes were then mounted on a farm of IBM RS6000 computers

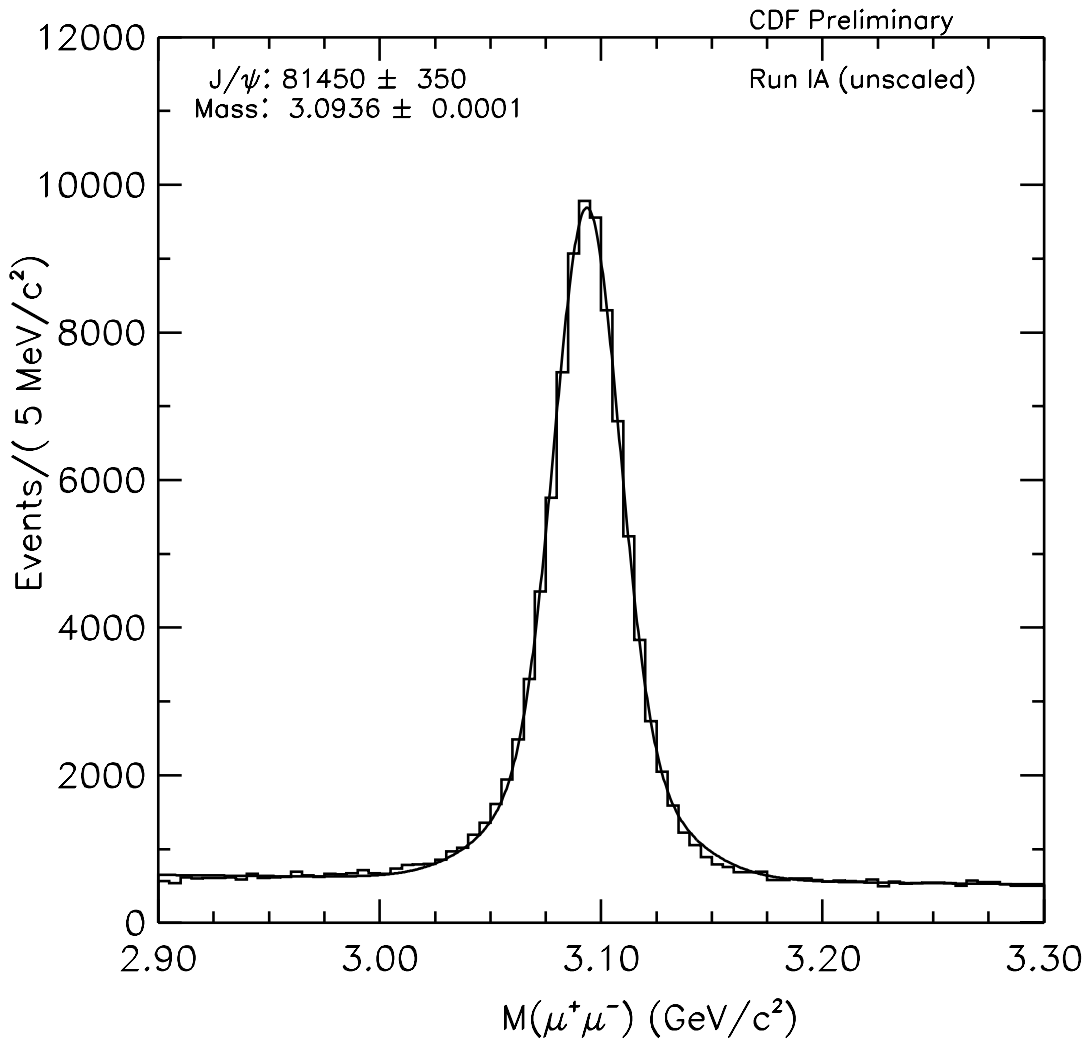

Figure 4.1: Dimuon mass distribution from events which pass online Stream 2 trigger requirements. All such mass distributions are made after constraining both muons to originate from a common vertex after partially correcting track parameters for energy loss and multiple Coloumb scattering. The distribution is shown before momentum scale corrections are applied. The fit is a linear background and a double Gaussian with a single mass parameter.

and were processed using a version of the offline production code (version 6.1). The result of the express production was that processed Stream 2 events were separated by specific Stream 2 trigger and were rapidly accessible on disk. For the data stored on disk, raw detector information and other lower level information was dropped from the event record.

The production of event files takes raw detector information and yields higher level quantities. For example, production will look at digitized wire hits in the tracking and muon systems to form a muon candidate. This muon candidate has calculated momenta, vertex, CTC–muon matching variables, etc. Pattern recognition of CTC hits is performed and fitting is done to calculate track parameters for identified tracks. The analysis uses these higher level quantities to calculate the physics quantities of interest and to make requirements to improve the signal-to-noise.

Further processing (termed "6.15") on the events was done to correct for several systematic effects present in the version 6.1 processing. First, the pattern recognition and fitting for SVX hits to CTC tracks was redone with a modified algorithm. The SVX performance worsened as the run progressed due to radiation damage. The modified algorithm removed a bias toward picking up SVX hits from the innermost layer where the radiation damage was greatest. A second modification was to correct the helical track parameters for effects due to the magnetic field not being uniform. These corrections were greatest for for tracks which passed near the outer edge of the CTC. Figure 4.2 shows the fitted J/ψ mass as a function of the largest pseudorapidity of the two muons before and after such field corrections are applied. The corrections clearly improve the performance of the CTC. Systematics which are still present in this data are discussed in Chap. 7.

4.3 J/ψ Sample

4.3.1 Approach

The approach used to select J/ψ events involves a relatively loose set of selection criteria emphasizing efficiency over background rejection. The signal-to-noise ratio of the J/ψ in the dimuon data set is large even at the trigger level. In Fig. 4.1, the signal-to-noise at the J/ψ mass is 15.7. Improvements to the signal-to-noise can be made without much loss of efficiency; that is done and will be discussed below. However, in the reconstruction of B mesons, further requirements on P_T, $c\tau$, and CL(χ^2) also improve the signal-to-noise of the J/ψ. Final plots of a reconstructed B mass do not look much different if, for example, a cut is placed on the matching between the muon hits and the CTC track at three or four standard deviations. In other words, the more important backgrounds to reduce in this analysis do not

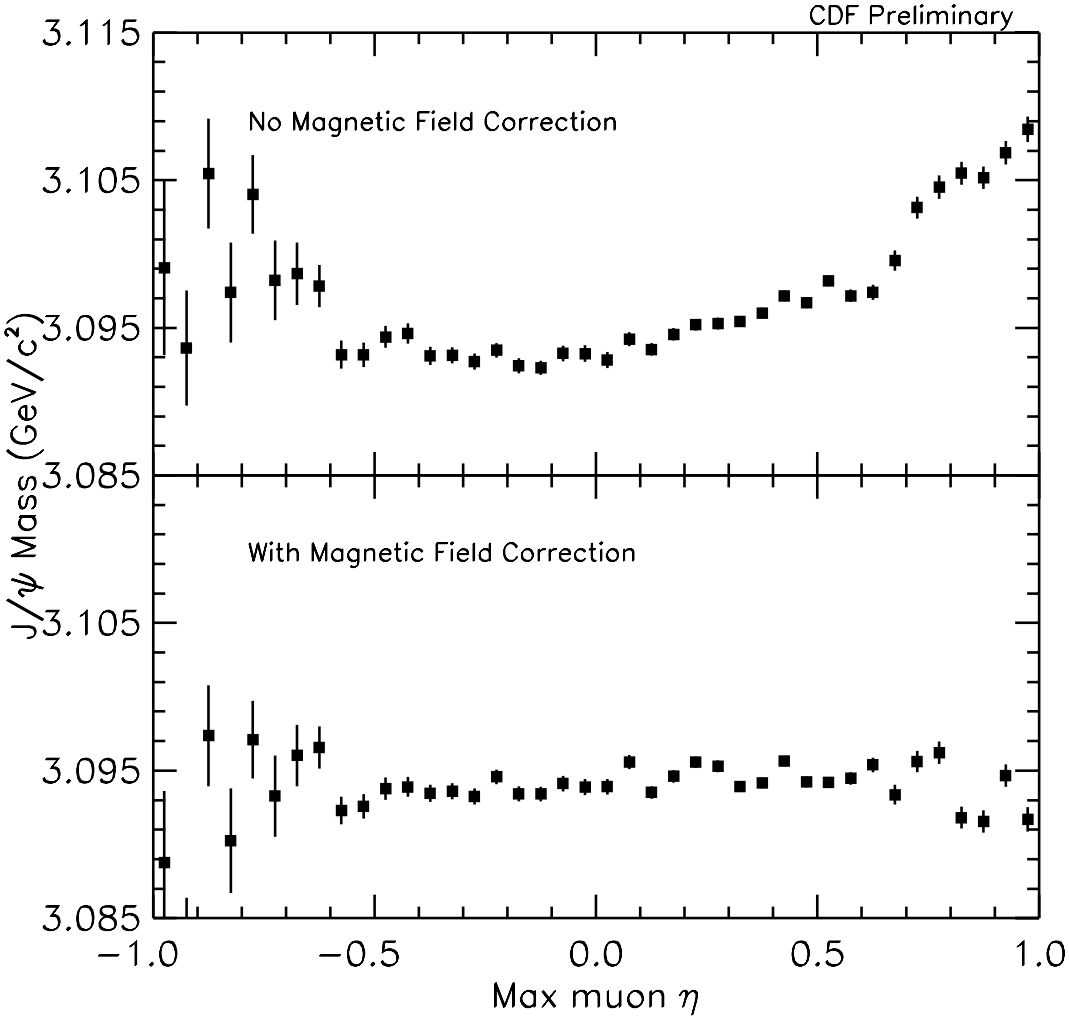

Figure 4.2: J/ψ mass distribution as a function of the maximum η of the two muons without and with corrections for non-uniformities in the magnetic field.

come from the background under the J/ψ; rather, they come from combinatorics associated with combining tracks with the dimuon.

4.3.2 Trigger Requirements on Processed Events

Events which satisfy the Stream 2 J/ψ trigger online are required to also pass the final Stream 2 trigger requirements calculated with the offline quantities. Since the online reconstruction cannot make use of calibration constants which are determined later from the data, it is expected that "better" reconstruction can be performed offline. Thus, this first requirement removes background events which in principle should not have passed the trigger. Out of the 205,610 events which pass Stream 2 J/ψ triggers, 150,738 events pass the final requirements on the offline banks. There is no discernable J/ψ signal in the mass distribution for the dimuon events removed by this requirement.

4.3.3 Muon Characteristics

Additional selection criteria on the muon candidates can be applied to the events in order to improve the signal-to-noise for the J/ψ signal. The improvement in signal-to-noise will be described for a set of minimal cuts, loose cuts, and tight cuts. This description should allow for a better understanding of the important characteristics present in the dimuon sample.

The additional criteria involve making requirements on the P_T of the muon candidate, matching between the CTC track and muon stub, and presence of energy deposition in the appropriate calorimeter tower. The requirements differ depending on which muon chambers are involved. Muon backgrounds arising from hadronic punch through, decays-in-flight (real μ), muon chamber noise, and back-scattered particles are less likely to have well-matched CTC tracks to the hits in the muon chambers compared to actual muons from J/ψ. These backgrounds also tend to have lower P_T tracks matched to the hits since there are more low-P_T tracks. A real muon should also leave a minimum ionizing signal in the calorimeter. Quantities on which requirements are to be made are studied by comparing the distribution of interest for sideband dimuons (mass between 2.9 and 3.0 GeV/c^2 or between 3.2 and 3.3 GeV/c^2) and for the sideband-subtracted J/ψ candidates (mass between 3.0 and 3.2 GeV/c^2). *Sideband-subtracted* refers to the distribution of the quantity of interest which has a bin-by-bin subtraction of the quantity observed in the sideband mass region. Based on these distributions, the values for the relevant selection criteria are determined. In the figures and discussion which follow, these distributions will be presented to justify the final set of requirements to be made for muon candidates.

Muon candidates can be classified on the basis of which muon detector subsystem had hits matched to a given track. A track may be matched to two muon subsystems. For example, a muon may cause hits in both the CMU and CMP which is often expected since these chambers overlap in coverage. A muon candidate which is matched to the CMU and CMX is probably better classified as being either a CMU or CMX since there is a small probability that a single muon could cause hits in both chambers. For this analysis, muons which have hits in two detector subsystems are reclassified if the Stream 2 matching requirements (For instance, $\chi^2_{\rm CMU} < 16$) are not satisfied for one of the subsystems. Thus, a CMU–CMX muon candidate with poor CMX matching would be reclassified as a CMU muon. The histogram in Fig. 4.3 shows the muon type for the signal (sideband-subtracted) and sideband regions. The ratio of the number CMU–CMP muons to the number of muons with CMU hits is larger for the J/ψ region. This feature is expected because real muons from J/ψ decays are more likely to have CMP confirmation than non-muon background present in the sideband region.

Figure 4.4 shows the transverse momentum of muon candidates for the sideband-subtracted J/ψ and sideband regions. The distributions are separated by the detector type (a single candidate can contribute to more than one plot). The edge which appears at 1.4 GeV/c is due to the reconstruction code which will not match muon hits to tracks with that low momentum. Muons with P_T below 1.4 GeV/c on average will not traverse five absorptions lengths of calorimeter. The edge which appears at 2.5 GeV/c is an artifact of the Level 2 trigger requirement which requires one of the muon legs (the CMX leg if present) to be found by the CFT which becomes efficient around 2.5 GeV/c. For the CMP, only muons with P_T larger than about 2.5 GeV/c would be expected to pass through the 8 absorption lengths of calorimeter. Any entries below 1.4 GeV/c are due to slight changes in the momentum after vertex constraining the muon pair.

Dimuon background under the J/ψ is reduced by applying selection criteria on the "*goodness*" of match between the hits in the muon chamber and the extrapolated track in the CTC. For real muons, the uncertainty in extrapolating the CTC track to the muon chambers is dominated by multiple scattering within the calorimeter through which the muon traverses. The multiple scattering uncertainty including energy loss is approximately given by Eq. 4.1 [51] which takes into account the CDF geometry:

$$\sigma_x = \frac{13.8\text{cm}}{P_T}\left[\frac{(0.59 + 0.41/\sin\theta)}{(1 - 0.71/P_T)}\right]^{\frac{1}{2}} \tag{4.1}$$

where P_T is the transverse momenta of the track in GeV/c. The typical uncertainty is such that a 3 GeV/c muon is expected to be extrapolated to within roughly 5 cm of the muon hits. A χ^2 is formed by dividing the extrapolation distance by the multiple scattering uncertainty. This is done only in the muon

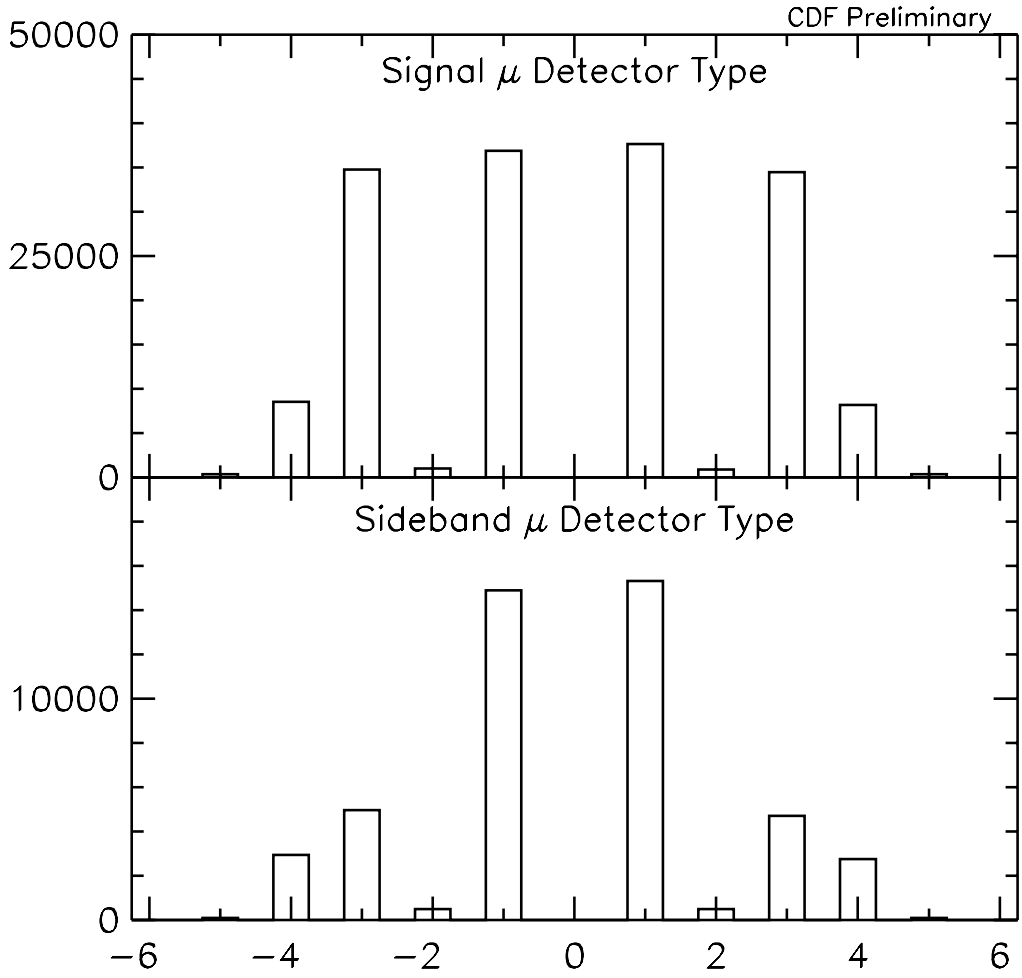

Figure 4.3: Distribution of muon types for dimuons bit encoded so 0=CMU, 1=CMP, and 2=CMX. Sign indicates muon charge. A negative muon candidate with hits in both the CMU and CMP would correspond to type -3. In the top plot, the distribution comes from the sideband-subtracted J/ψ region. In the bottom plot, the distribution comes from the sideband J/ψ region.

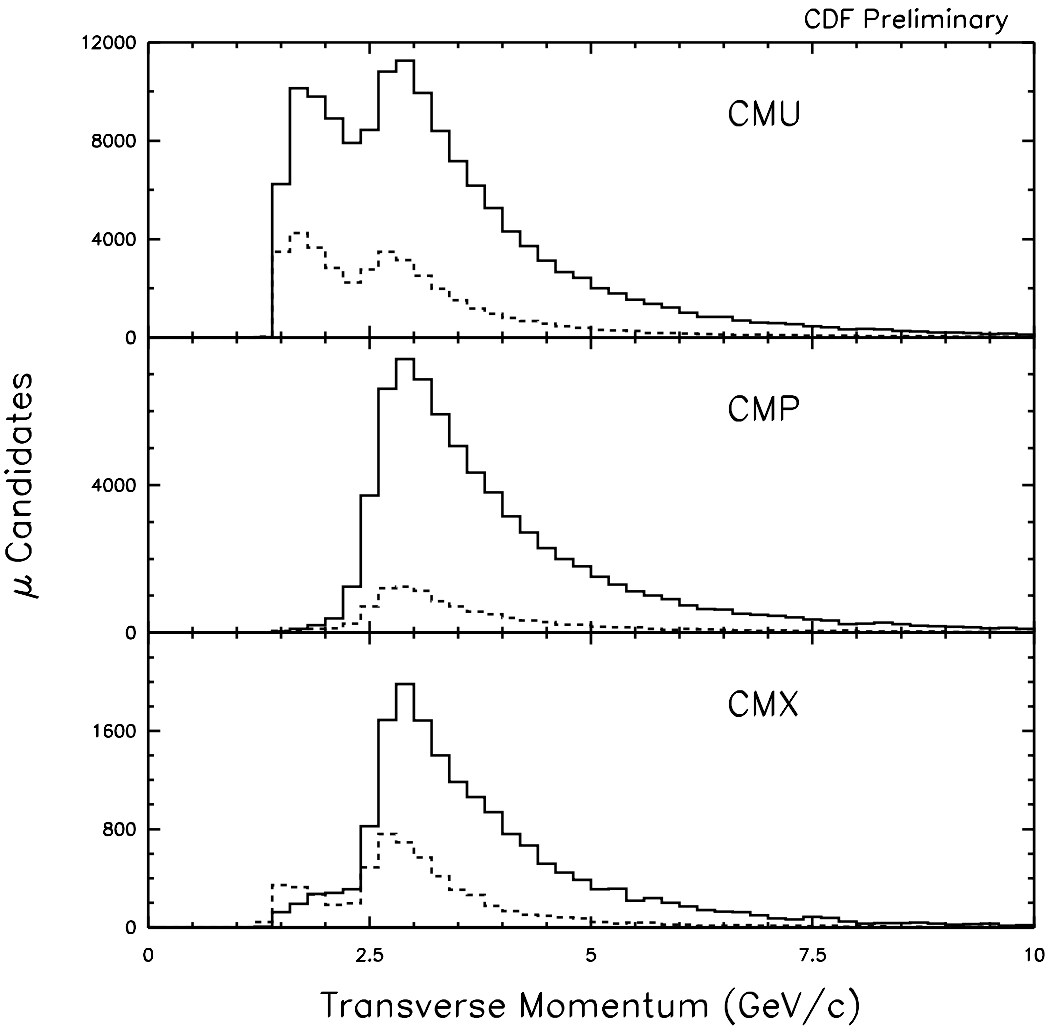

Figure 4.4: Transverse momentum of muon candidates for (solid) sideband-subtracted J/ψ and (dashed) sideband regions classified by the detector subsystem.

chamber local x coordinate except for the CMU where a χ^2 is formed also in the local z coordinate. These muon matching χ^2's are calculated during production and are accessible to the analysis program. The square root of these matching χ^2 are expected to be Gaussian distributed with a mean of zero and a width of one for real muons. The distribution is expected to be broader for muon background such as noise hits. Figure 4.5 shows these quantities for the sideband-subtracted signal and sideband regions. Table 4.1 shows the result of Gaussian fits to the distributions. From this table, one would expect improvement in signal-to-noise by requiring matching to within three standard deviations (except for the CMU z where 3.5 σ could be required to preserve signal).

	Sideband-subtracted		Sideband	
	Mean	Width	Mean	Width
CMU x	0.00	0.99	0.02	1.38
CMU z	0.00	1.13	0.02	1.47
CMP x	0.01	0.99	-0.01	1.14
CMX x	0.01	1.05	-0.03	1.57

Table 4.1: Fits to Gaussians for the muon matching distributions.

As mentioned previously, calorimeter information can be used to increase the signal-to-noise for the J/ψ by requiring non-zero energy deposition in the calorimeter tower towards of the muon candidate. If hits in the muon chamber were not caused by a particle from the interaction point, then zero energy deposition in the appropriate calorimeter tower would be more likely. Figure 4.6 shows the energy deposition of the muon for each of the three muon subsystems.

4.4 Muon Selection

In the previous section, a number of distributions are presented which show various characteristics of both muons from J/ψ decays and muon candidates present in the sideband region. From these distributions, we can consider making cuts based on these distributions in order to improve the signal-to-noise of the J/ψ. Beginning with the basic distribution shown in Fig. 4.1 with no additional cuts, we can consider a minimal, loose, and tight set of cuts in terms of efficiency and background rejection defined as:

- Minimal: μ matching $< 3\sigma$ for x and 3.5 σ for z.
- Loose: Require one μ (the CMX μ if present) to have $P_T >$ 2.5 GeV/c.
- Tight: Require energy in the appropriate calorimetery tower.

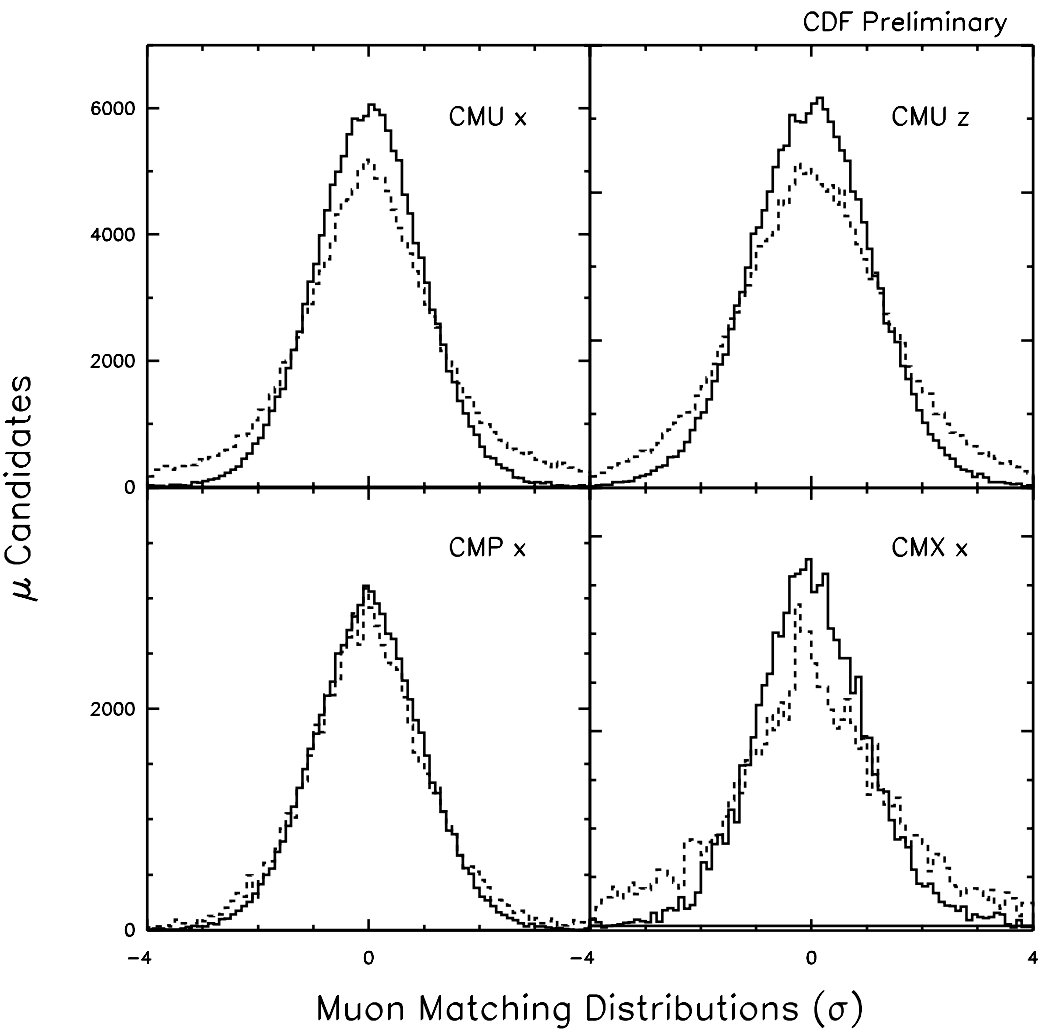

Figure 4.5: Muon matching distributions in units of standard deviation due to multiple scattering for (solid) sideband-subtracted J/ψ and (dashed) sideband regions. The sign indicates the muon charge. The dashed histograms are normalized to the solid histograms.

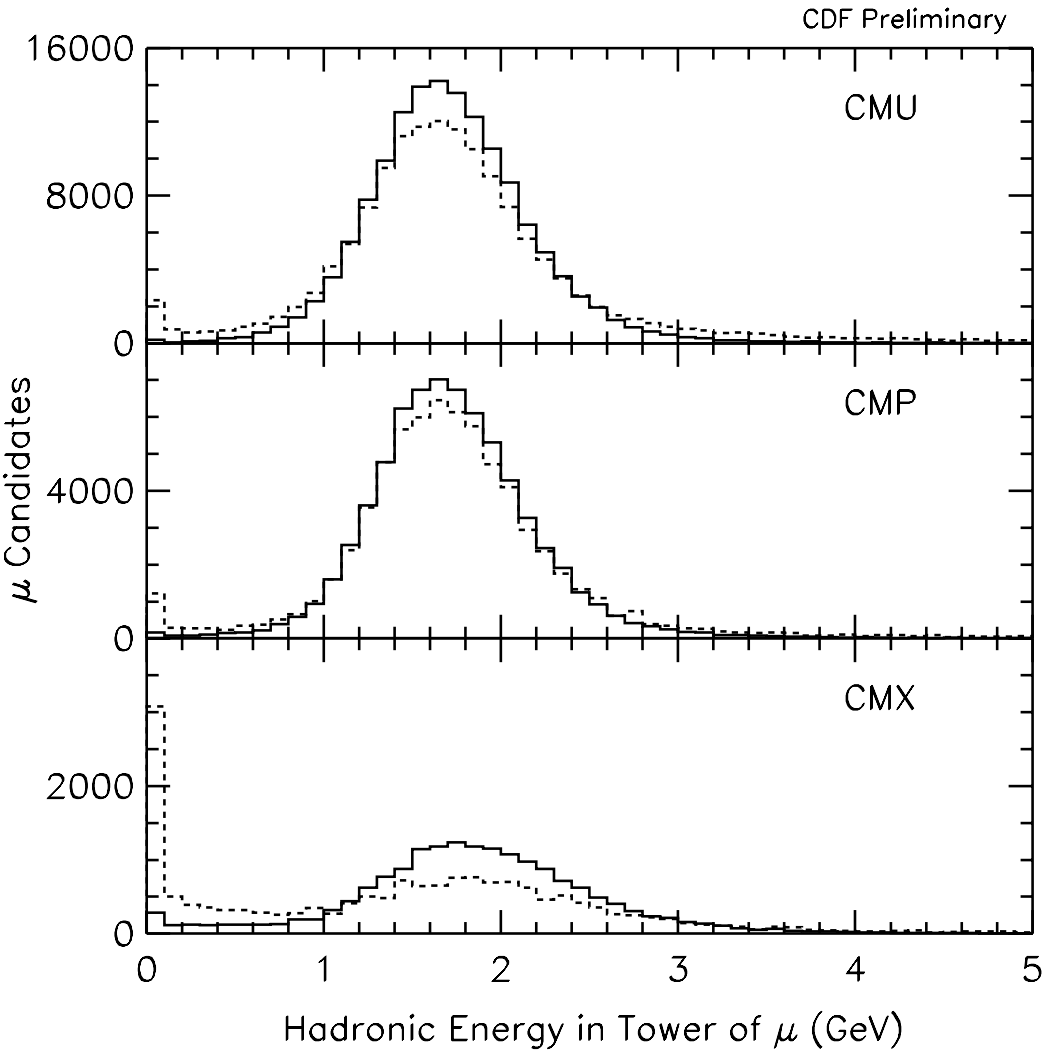

Figure 4.6: Hadronic energy in the tower of the μ candidate for (solid) sideband-subtracted and (dashed) sideband J/ψ regions. The dashed histograms are normalized to the solid histograms.

Figure 4.7 shows the dimuon mass distributions for events that fail each of the above cuts. Each of these distributions can be fit to a single Gaussian and linear background and compared with the fit of Fig. 4.1 to determine the efficiencies in Table 4.2.

Cut	J/ψs Lost	Background per 5 MeV/c^2	Eff. Signal	Eff. Background
None	–	587	1.000	1.0000
Minimal	686	523	0.991	0.891
Loose	2170	467	0.973	0.796
Tight	2425	449	0.970	0.765

Table 4.2: Muon selection requirements

In this analysis, the *minimal* [52] set of cuts are applied with a 1% inefficiency. We wish to remain as fully efficient as possible and do not apply additional cuts. The muon matching cuts remove only 5% of the background level in a typical $B^- \to J/\psi\ K^-$ reconstruction such as shown in Fig. 1.1 since P_T, $c\tau$, and CL(χ^2) cuts also reduce the background dimuons.

4.5 J/ψ Mass Window Requirement

From Fig. 4.1, one can see that nearly all the J/ψs come from dimuons within 100 MeV/c^2 of the world average J/ψ mass of 3096.9 MeV/c^2. A window of 100 MeV/c^2 around the world average J/ψ mass is required. An alternative approach requiring the measured dimuon mass to be within three standard deviations (calculated using the mass uncertainty of the event) of the world average gives virtually identical results in the B candidate mass distributions. The simplicity of a 100 MeV/c^2 window is preferred and is used.

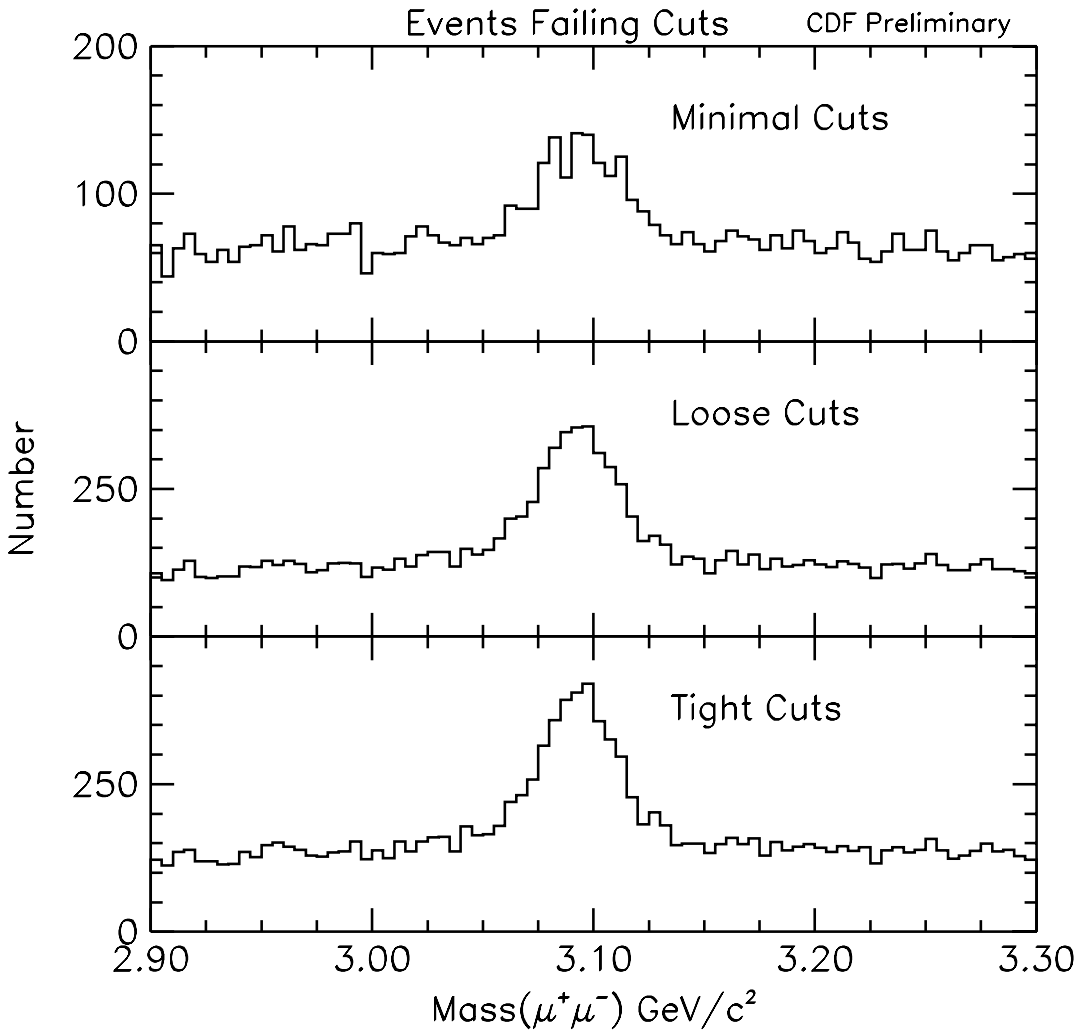

Figure 4.7: Dimuon mass distributions for events failing a minimal, loose, and tight set of muon cuts as described in the text.

Chapter 5

Analysis

The analysis has been outlined in the Introduction in section 1.4. In this chapter, the analysis will be described in greater detail with emphasis on the justification for making various choices. A set of selection criteria will be motivated using Monte Carlo and physics arguments for preserving b hadron signal and by using combinatoric background for background rejection. In the following chapter, the results of applying the analysis on various reconstructed modes will be discussed including the reconstruction of $B_s^0 \to J/\psi\ \phi$.

5.1 Track selection

Applying selection criteria to track candidates is done to remove certain pathologies, reduce background, and to improve the mass resolution. These selection criteria are to require that the track be well-measured in the CTC and to use SVX information if and only if the match between the CTC and SVX track segments is good. The main requirement is that the track must be measured in three dimensions by the CTC and must have a minimum number of associated hits on a minimum number of axial and stereo superlayers. Figure 5.1 shows the number of axial (stereo) CTC superlayers with more than four (two) hits for muons from the sideband and the J/ψ sideband-subtracted regions. Notice that real tracks associated with muon hits tend to have more superlayers with hit information. The requirement is made that there must be at least two axial and two stereo superlayers with a minimum of four axial and two stereo hits. This loose requirement removes two dimensional track candidates (without stereo information, or found only in the VTX, etc) and other poorly measured track segments. This requirement also speeds up the computational time of the analysis.

Selecting well-measured tracks helps remove possible pathologies which allow background to enter into the signal region. For instance, consider a CTC track

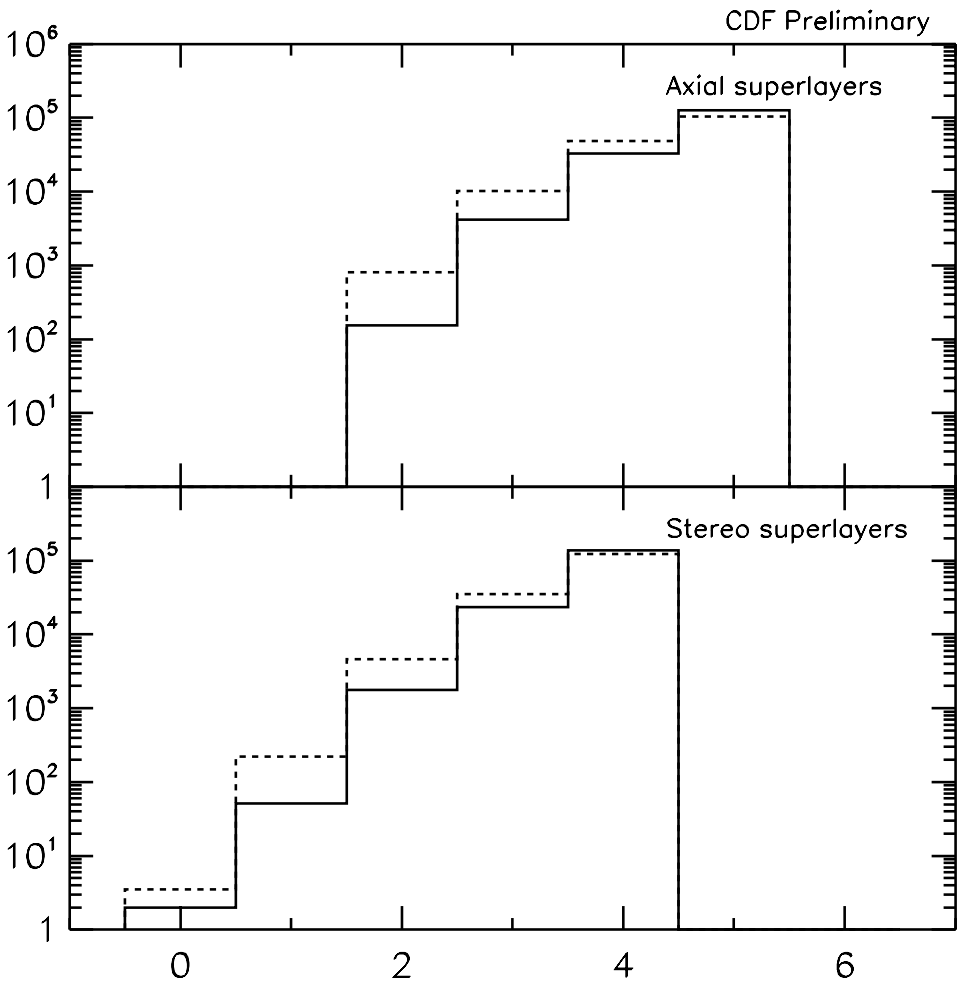

Figure 5.1: Number of (top) axial and (bottom) stereo superlayers with a minimum of four and two hits respectively. The solid histograms shows the sideband-subtracted signal region and the dashed histogram shows the normalized sideband region.

matched to SVX hits either due to noise in the SVX or to another track. In this case, one would expect the track impact parameter to be large since it is being steered by misassociated SVX information. Further, since SVX information is present, the covariance matrix will indicate that the impact parameter is well measured. We require that SVX information be used for a given track only if the χ^2/dof of the SVX-CTC match is less than six. This requirement has been shown to remove pathologies with misassociated SVX information [53].

5.2 Daughter Meson

The *daughter meson* refers to the K, K^*, or ϕ candidate in $B^- \to J/\psi\ K^-$, $B^0 \to J/\psi\ K^*$, and $B_s^0 \to J/\psi\ \phi$ decays respectively. CDF does not have particle identification which clearly distinguishes kaons from pions. Thus, a K candidate is any charged track assigned a kaon mass. A K^* candidate consists of any two oppositely charged tracks that have an invariant mass in a window around the K^* mass when one track is assigned a kaon and one a pion mass. In the case where the two tracks are consistent with the K^* in $B^0 \to J/\psi\ K^*$ decay under both mass assignments, only the K^* candidate closest to the world average K^* mass is used. This procedure has been estimated to be correct approximately 65% of the time with insignificant loss of mass resolution [54]. A ϕ candidate consists of any two oppositely charged tracks which have an invariant mass in a window around the ϕ mass when both tracks are assigned kaon masses. Specifics concerning the size of the window used for the daughter mesons will be discussed below.

5.3 Constrained Fits

The mass resolution is improved by using the best possible estimates of the track parameters. In order to demonstrate possible improvements in mass resolution, consider the reconstruction of $\mathrm{J}/\psi \to \mu^+\ \mu^-$. In Fig. 5.2 are shown a number of dimuon mass distributions of events where both muons have SVX information available. In (a), the mass distribution is shown where track parameters are measured only by the CTC without dE/dx and multiple scattering corrections. In (b), again CTC measured tracks are used but here both the corrections and a vertex constraint have been applied. In (c), the mass distribution is shown using SVX information for the tracks. In (d), both SVX information and a vertex constraint are used for the muon legs and noticeable improvement in resolution is observed. Table 5.1 shows the results of fitting the J/ψ peak to a Gaussian for each of these distributions.

The improvement in mass resolution can also be observed in the reconstruction of exclusive final states. In addition to applying dE/dx and multiple scattering

Fig. 5.2	Tracking	dE/dx + MS Corrections	Constraints	Mass (MeV/c^2)	Width (MeV/c^2)
a	CTC	No	none	3091.3 $\pm$ 0.2	27.3 $\pm$ 0.2
b	CTC	Yes	Vertex	3093.3 $\pm$ 0.1	22.5 $\pm$ 0.1
c	CTC + SVX	Yes	none	3093.7 $\pm$ 0.1	20.6 $\pm$ 0.1
d	CTC + SVX	Yes	Vertex	3093.8 $\pm$ 0.1	15.3 $\pm$ 0.1

Table 5.1: Fit results of dimuon mass spectra in Fig. 5.2.

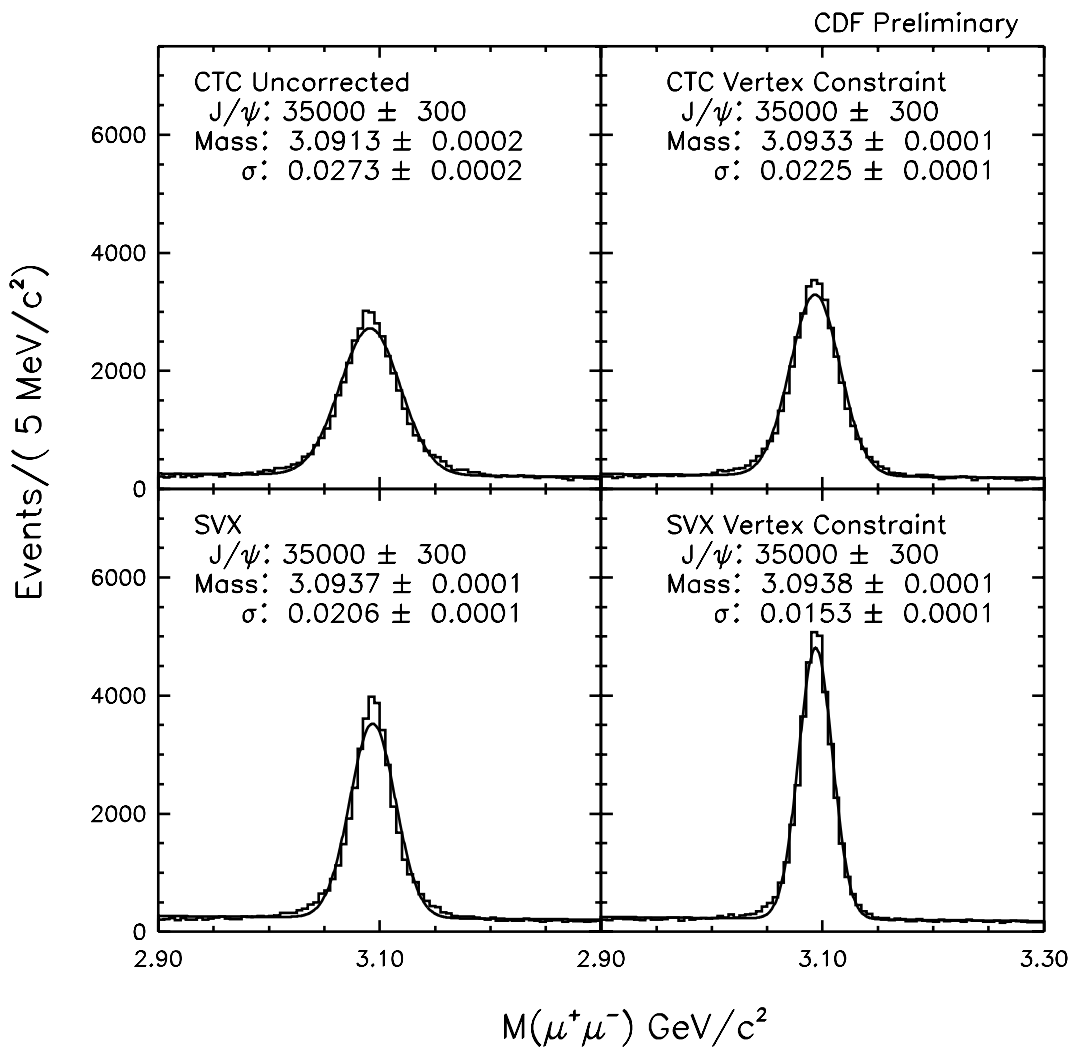

Figure 5.2: Dimuon mass distribution for J/ψ candidates reconstructed with various corrections and constraints as described in the text.

corrections, to using SVX information when it is available, and to using a vertex constraint, the reconstruction of exclusive final states is further improved by the addition of a constraint of the dimuon to the world average J/ψ mass and by a constraint which requires the final state to point back to the primary vertex in two dimensions. A three dimensional pointing constraint is not done because there is little improvement in resolution and the interaction of r-ϕ and r-z measurements is less well understood. In Figs. 5.3, 5.4 are shown a number of mass distributions of $J/\psi\ K^-$ where the events have been selected as discussed in section 1.4. In Fig. 5.3 (top), CTC or SVX information is used without dE/dx and multiple scattering corrections. In Fig. 5.3 (bottom), the corrected CTC or SVX information is used. There is little improvement since the corrections are small compared with the nominal resolution. Figure 5.4(top) shows the improvement in mass resolution when applying a vertex constraint and simultaneously mass constraining the dimuon to the J/ψ mass. In (bottom), the additional r-ϕ pointing constraint is applied. Table 5.2 shows the results of fitting the $J/\psi\ K^-$ peak to a Gaussian for each of these distributions. Addition of the pointing constraint improves the mass resolution because it uses information which in principle should give better estimates of the track parameters. Further, selecting combinations which pass a 1% requirement on CL(χ^2) is more stringent for the fit with the pointing constraint than without it.

Figure	Tracking	Constraints	Mass MeV/c^2	Width MeV/c^2
top	CTC + SVX	no dE/dx	5286 $\pm$ 6	47 $\pm$ 7
bottom	CTC + SVX	with dE/dx	5285 $\pm$ 4	47 $\pm$ 7
top	CTC + SVX	Vertex + J/ψ Mass	5278 $\pm$ 2	18 $\pm$ 2
bottom	CTC + SVX	above constraint + 2D Pointing	5277 $\pm$ 2	15 $\pm$ 2

Table 5.2: Fit results of mass spectra in Fig. 5.3 and Fig. 5.4.

5.3.1 Unconstrained Mass Window Requirements

In order to reduce the computational time for the analysis, requirements are made on the reconstructed mass of the resonances and P_T of the tracks using track parameters which are not subject to constraints and which have not been corrected for dE/dx and multiple Coulomb scattering. Care is taken to insure that the effects of these requirements do not impact the final distributions. That is, since the mass will change after corrections and after constraints are imposed, one needs to make sure that requirements on the uncorrected and unconstrained quantities will not influence a corrected and constrained distribution. The trigger

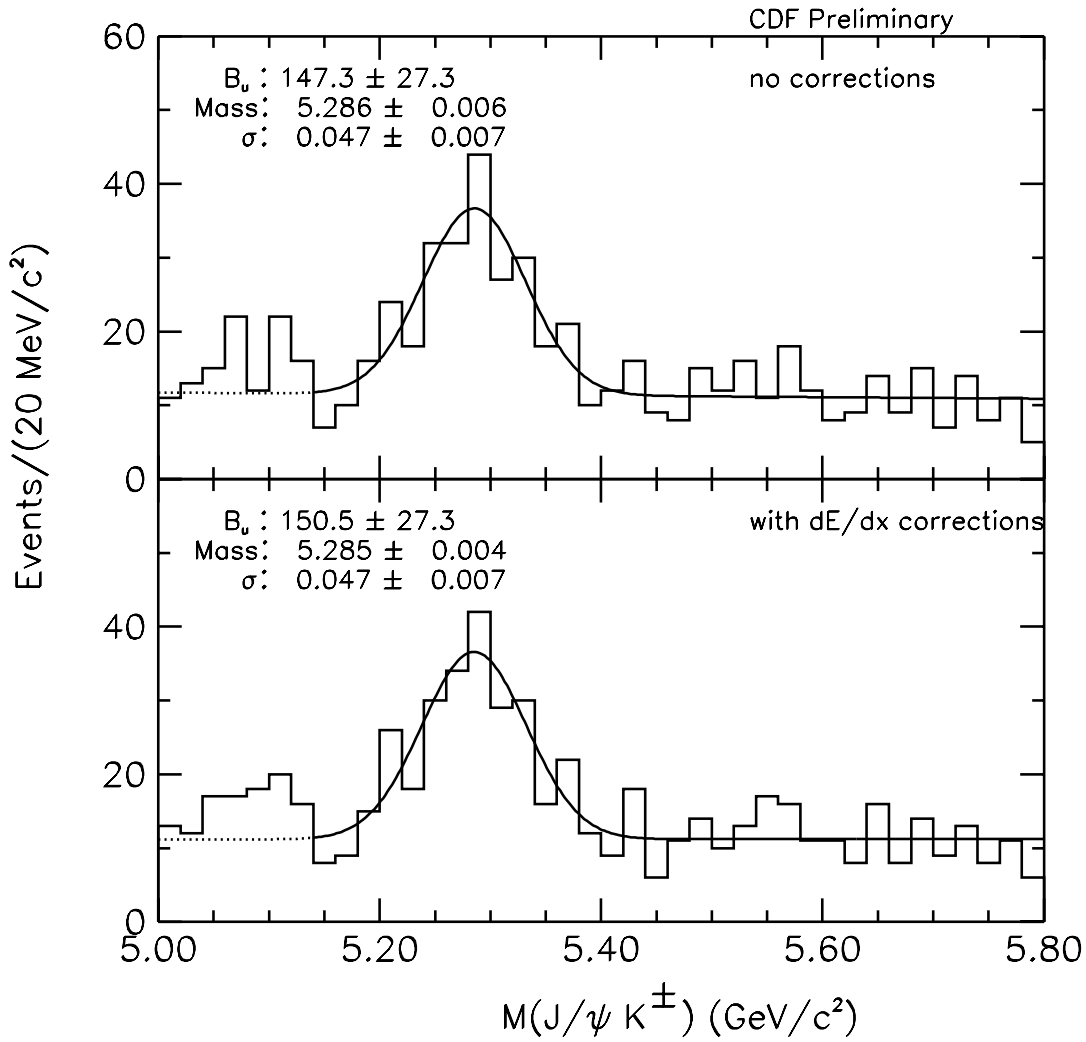

Figure 5.3: $J/\psi\ K^-$ mass distribution for B^- candidates reconstructed without and with dE/dx corrections.

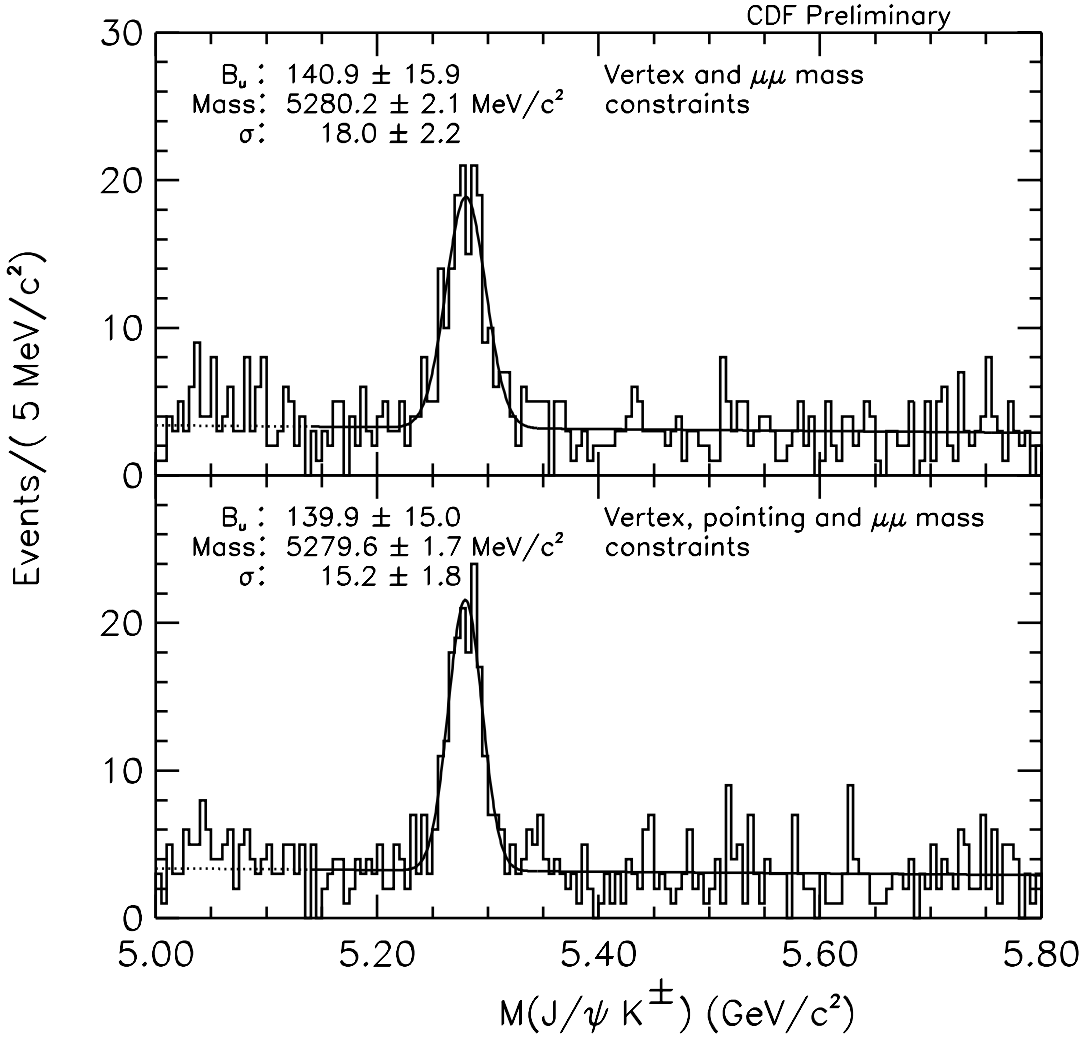

Figure 5.4: $J/\psi\ K^-$ mass distribution for B^- candidates reconstructed with vertex and pointing constraints.

selects dimuons with mass between 2.8 and 3.4 GeV/c^2. After a vertex constraint, the background is flat between 2.85 and 3.35 GeV/c^2 which includes the entire sideband and signal region from 2.9 to 3.3 GeV/c^2. When reconstructing exclusive B states, an unconstrained and uncorrected mass window 300 MeV/c^2 wider than requirements on the constrained B reconstruction is used. Figure 5.5 shows the mass distribution for $J/\psi\ K^-$ candidates (solid) with constraints and (dashed) without constraints with the following minimal cuts:

- Vertex constrained mass($\mu^+\mu^-$) between 2.9 and 3.3 GeV/c^2
- $P_T(K) > 1.5$ GeV/c (unconstrained)
- Mass($J/\psi\ K^-$) between 4.7 and 6.1 GeV/c^2 (unconstrained)
- $P_T(K) > 1.8$ GeV/c (fully constrained)
- Mass($J/\psi\ K^-$) between 5.0 and 5.8 GeV/c^2 (fully constrained)
- CL(χ^2) $> 1\%$ on the constrained fit (lower figure only)

The issue is whether a significant number of additional combinations could enter the constrained mass region (5.0 to 5.8 GeV/c^2) if the requirement on the unconstrained region would be wider than 4.7 to 6.1 GeV/c^2. In the top figure, there is some evidence that the tails for the unconstrained mass do extend past the 4.7 to 6.1 GeV/c^2 region, but, the bottom figure shows that those combinations are most likely to fail an additional requirement on the CL(χ^2) of the constrained fit.

5.3.2 Primary Vertex

The interaction region at CDF is distributed along the z-axis with a width of approximately 30 cm. At any given z, a beam spot can be defined as the one sigma distribution of x and y positions of collision points. The primary vertex is determined by measuring the beam position on a run-by-run basis. The beam position is determined by fitting a straight line to the beam in the r-ϕ plan giving the x_0 and y_0 positions of the beam center with respect to the CDF origin and the slopes in x and y as a function of the longitudinal position z. The beam position can be determined online during data-taking using the first several hundred events. Slightly better precision can be obtained with an offline analysis which stores results in a database. For this analysis, these differences are minor. The uncertainty in the r-ϕ plane is 40 μm which is roughly a 35 μm beam spot size convoluted with a 20 μm measurement uncertainty. Figure 5.6 shows the beam profile calculated for a particular run. Figure 5.7 shows the sideband-subtracted difference in the primary vertex z_0 between a calculation which uses the average

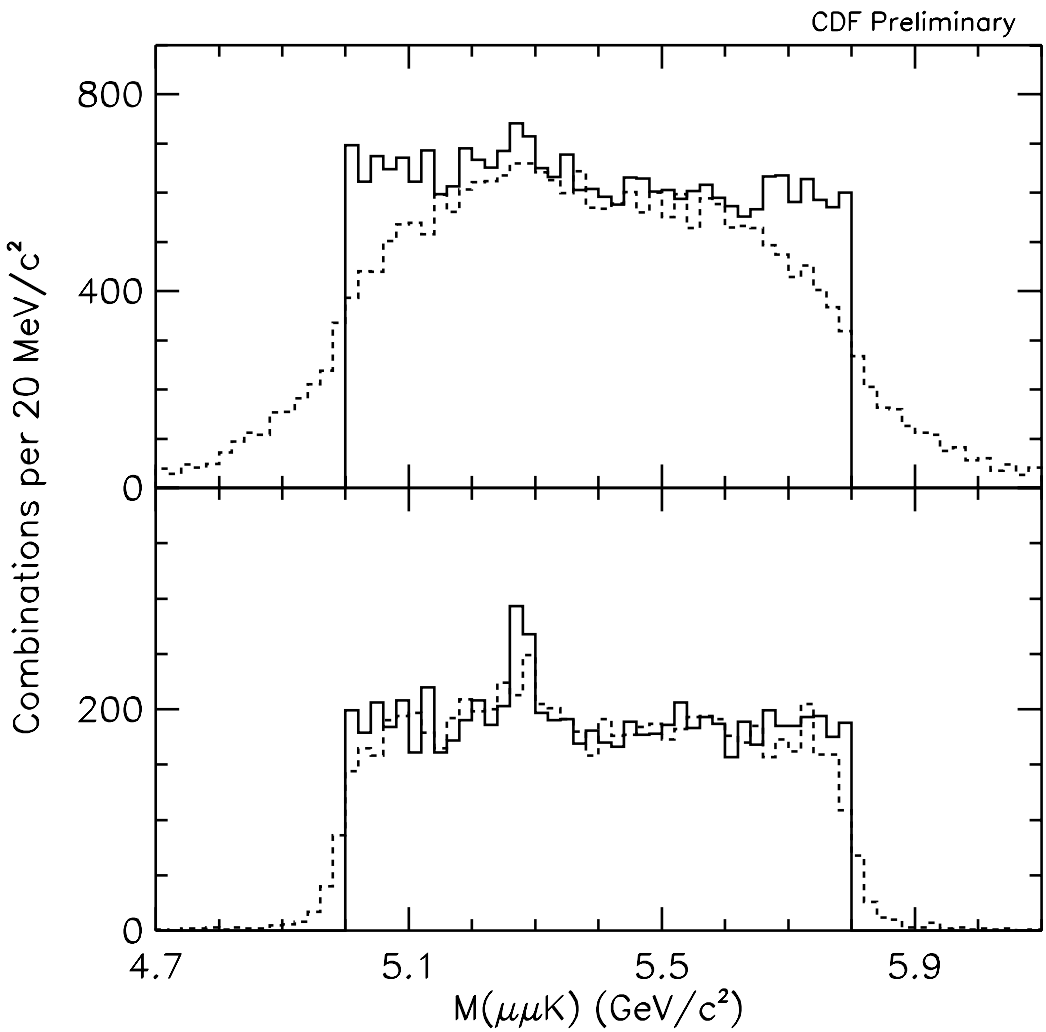

Figure 5.5: Constrained (solid) and unconstrained (dashed) mass distributions of $J/\psi\ K^-$ candidates which satisfy a minimal set of cuts. In the bottom figure, an additional quality requirement on the goodness of the CL(χ^2) from the constrained fit is required.

muon z_0 after the vertex constraint and a calculation which picks up the vertex found in the VTX which has the highest total P_T originating from it. Fitting to a Gaussian gives the z_0 resolution of approximately 0.5 cm which is taken to be the uncertainty in z_0.

5.3.3 Constrained Fit and Secondary Vertex

As already described, track parameters are subject to several geometrical and kinematic constraints to improve the mass resolution. The constrained fit [55] involves an iterative adjustment of the track parameters imposing constraints so as to minimize the χ^2 calculated from the change in parameters with respect to their errors. The iterative process is needed as some non-linear derivatives are approximated by linear terms in a Taylor's series expansion. Several constraints are available including mass, vertex, and a pointing constraint which requires a system of tracks to point back towards a given primary vertex. The result of the constrained fit is a new set of track parameters and a secondary vertex along with the associated error matrices. The fit also returns a CL(χ^2) which is calculated using the change in each of the track parameters weighted by the appropriate uncertainties contained in the covariance matrix. For tracks which do not come from the same vertex as the two muons, the attempt to constrain the track parameters to come from that vertex results in a large χ^2 which can be used to distinguish these tracks from those which have a much higher probability of originating from a common vertex. The power of making requirements on both the calculated $c\tau$ and CL(χ^2) which come from the constrained fit will be demonstrated below.

5.4 Preserving Signal

A set of selection criteria are used to reject combinatoric background while preserving the signal. These selection criteria were chosen on the basis of their power to improve the signal-to-noise in reconstructing $B^- \to J/\psi\ K^-$ and $B^0 \to J/\psi\ K^*$ and on the basis of simplicity. By "simplicity," the requirements involve round numbers (P_T(X) $>$ 2 GeV/c not P_T(X) $>$ 1.875 GeV/c). The selection criteria include making cuts on kinematic quantities such as the transverse momentum of the daughter mesons, the transverse momentum of the B meson, $c\tau$ of the reconstructed B, and CL(χ^2) from the constrained fit. In this chapter, a brief discussion is given of what is expected for these quantities for signal events. A quantitative description will be given for what happens to the combinatoric background upon application of the selection criteria. In the next chapter, using the reconstructed decays, the effects of the selection criteria will be quantified for the signal.

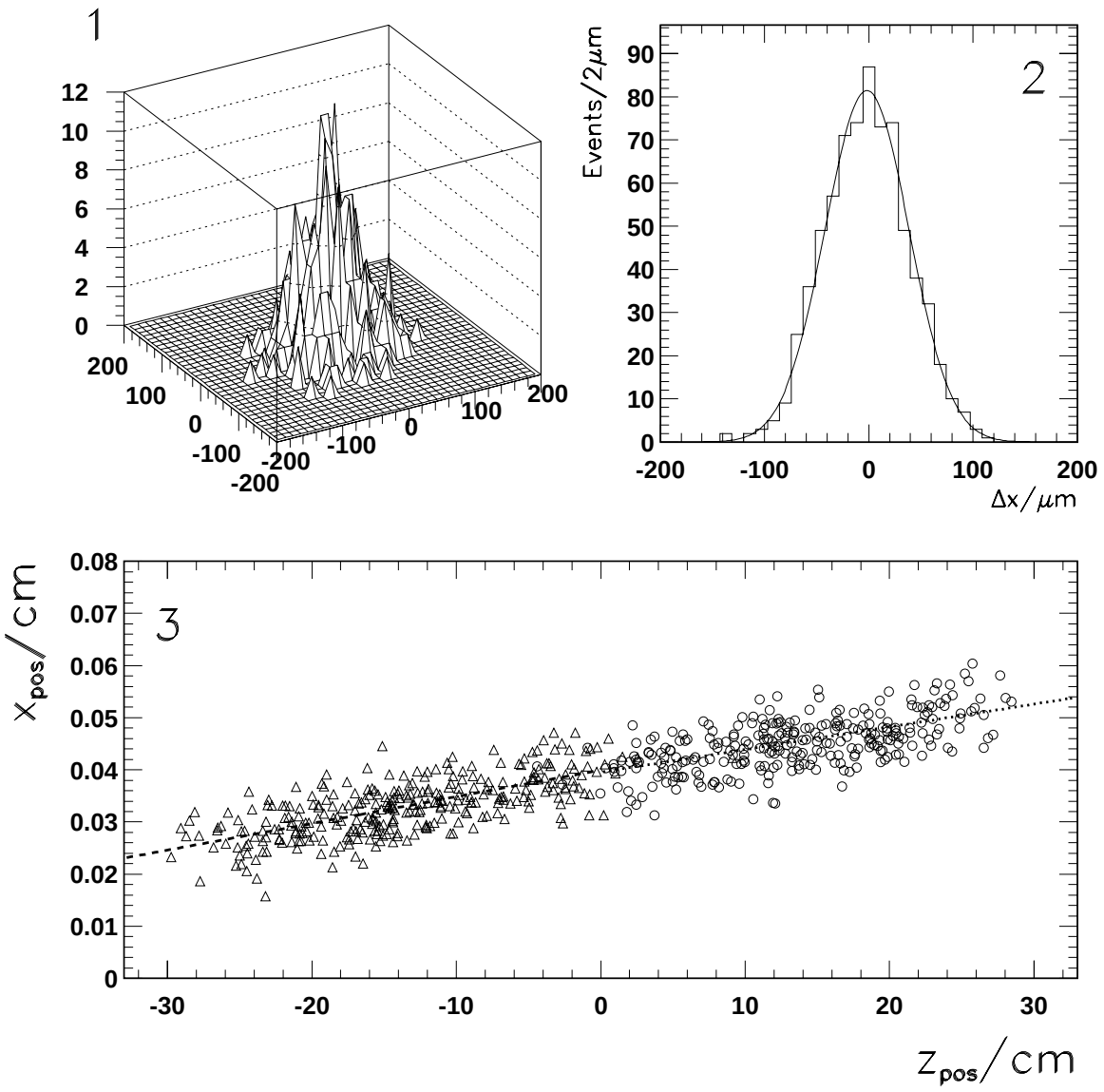

Figure 5.6: Beam profile in (1) r-ϕ, (2) x only, and in the (3) $x - z$ plane. In (3), each primary vertex is indicated by a circle or triangle depending on whether the track was matched to SVX hits in the East or West barrel.

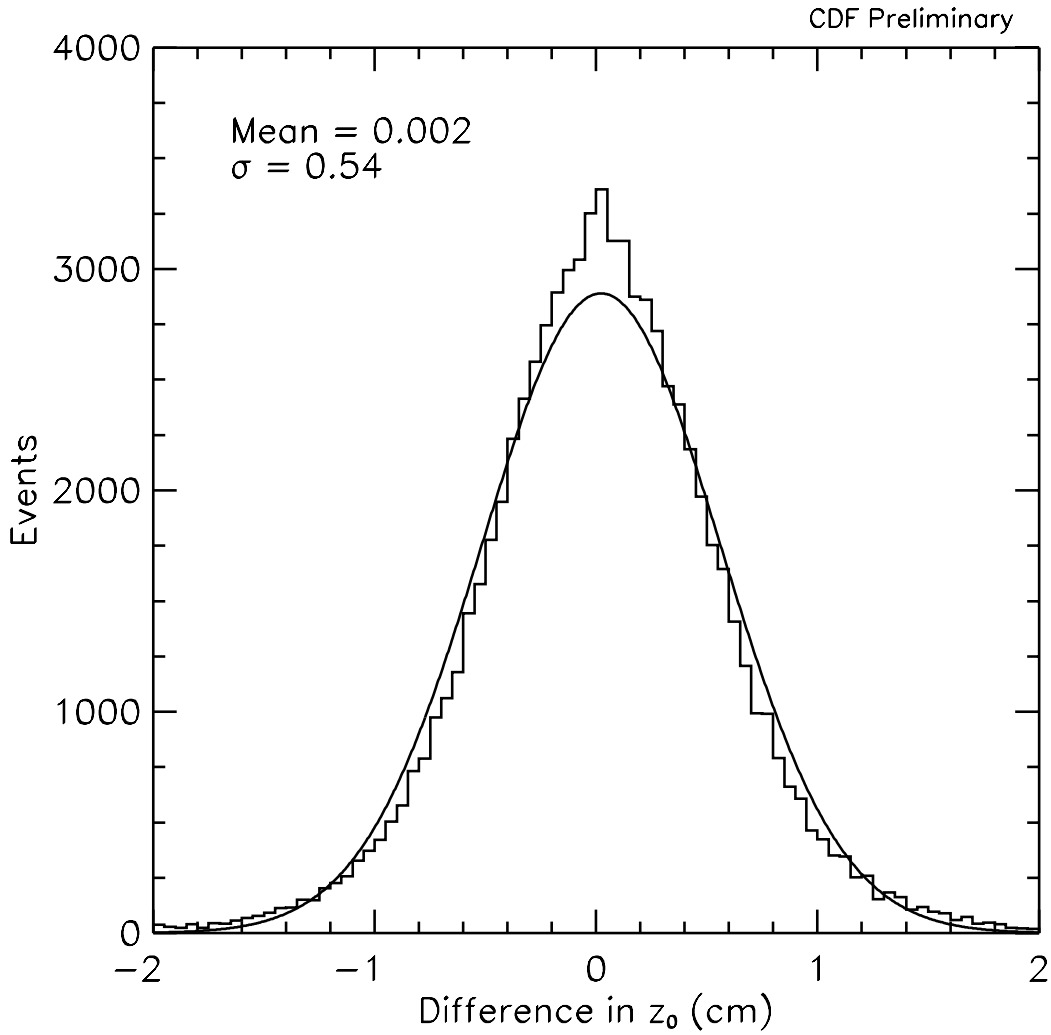

Figure 5.7: Difference in z_0 between the average muon z_0 and the primary vertex found by the VTX. The fit is a Gaussian.

5.4.1 Kinematics of $B \rightarrow J/\psi\ X$

The kinematics of $B \rightarrow J/\psi\ X$ can be studied using a Monte Carlo simulation which incorporates the NDE b quark production spectrum, Peterson fragmentation, and a model of CDF including the dimuon trigger. The characteristics of the dimuon trigger impact greatly the kinematics of reconstructed b hadrons at CDF. The efficiencies which will be quoted are after simulation of the trigger and detector. Work is in progress to calculate cross sections [56] which relies on the trigger efficiencies and detector acceptance. The histograms in Fig. 5.8 show the P_T spectrum of J/ψs from two-body B meson decays in the Monte Carlo along with the spectra for the daughter meson and the B meson. The points represent the spectra observed in the sideband-subtracted data using $B^- \rightarrow J/\psi\ K^-$ and $B^0 \rightarrow J/\psi\ K^*$ decays described in the next chapter. Some differences in the P_T distribution for the K and K^* are expected but those differences are small and inconsequential for this discussion as are polarization effects [57]. Note that a requirement on $P_T(\mathrm{X}) > 2$ GeV/c has been applied to both the data and the Monte Carlo events.

The agreement between Monte Carlo and data provides confidence in using the Monte Carlo to calculate the efficiency for the signal when the kinematic selection criteria are varied. Figure 5.9 (solid) shows the Monte Carlo transverse momentum distribution for the daughter meson in two-body $B^0 \rightarrow J/\psi\ K^*$ decays and for the B meson itself. The P_T distributions are nearly identical for the kinematically similar $B_s^0 \rightarrow J/\psi\ \phi$ decay. The dashed (dotted) histograms show the distribution after requiring the $P_T(\mathrm{B}) > 6$ (8) GeV/c or $P_T(\mathrm{X}) > 2$ (3) GeV/c. Also shown are the corresponding inefficiency curves for making a P_T cut at a particular value. From this curve, imposing the $P_T(B)$ to be above 6 GeV/c, we expect to lose approximately 35% of the signal when also making a cut on $P_T(\mathrm{X})$ at 2 GeV/c. This inefficiency for signal will be compared with the power of rejecting combinatoric background as a function of these cuts.

5.4.2 Expected $c\tau$ Distribution for Signal

b hadrons have an average lifetime of $1.46 \pm 0.06 \pm 0.06$ picoseconds [58] which translates into a decay length of order 500 μm for $P_T(B) \sim 10$ GeV/c. This decay length is large compared with the expected resolution using the SVX and comparable to the expected resolution using CTC information only. Thus, the signal is expected to have a measurable proper lifetime distribution which is distinguishable from combinatoric background with no lifetime. Making a selection on $c\tau$ should preserve signal and reject background. The next chapter will give some quantitative feel of the power of making a cut on $c\tau$. A detailed analysis determining the proper lifetime of b hadrons is ongoing and will contain more detail [59].

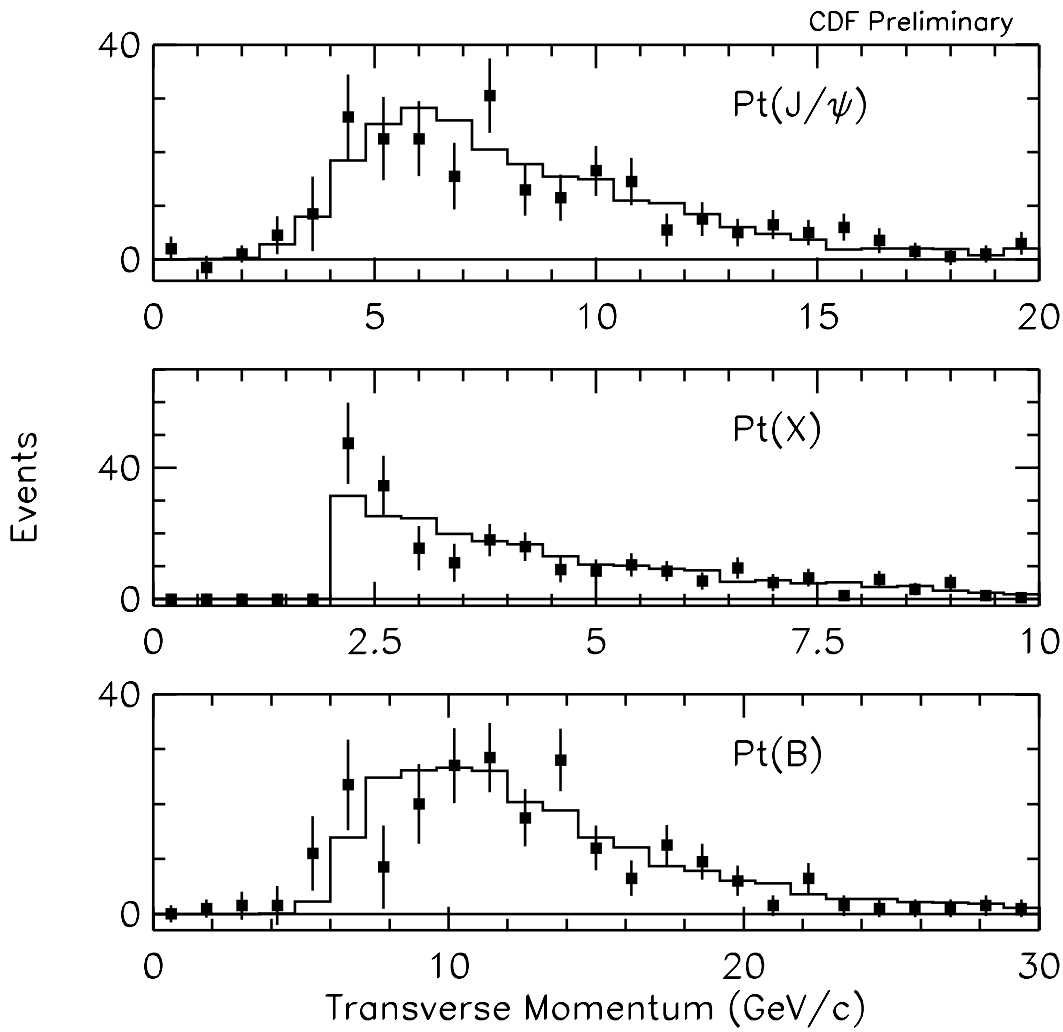

Figure 5.8: Monte Carlo (histogram) transverse momentum spectra of J/ψ coming from $B \to J/\psi\ X$ decays. Also shown are the spectra of $P_T(X)$ and $P_T(B)$. The points represent the sideband-subtracted distribution observed in the data using $B^- \to J/\psi\ K^-$ and $B^0 \to J/\psi\ K^*$ decays. The sharp edge at 2 GeV/c reflects one of the selection criteria used in both the Monte Carlo and data.

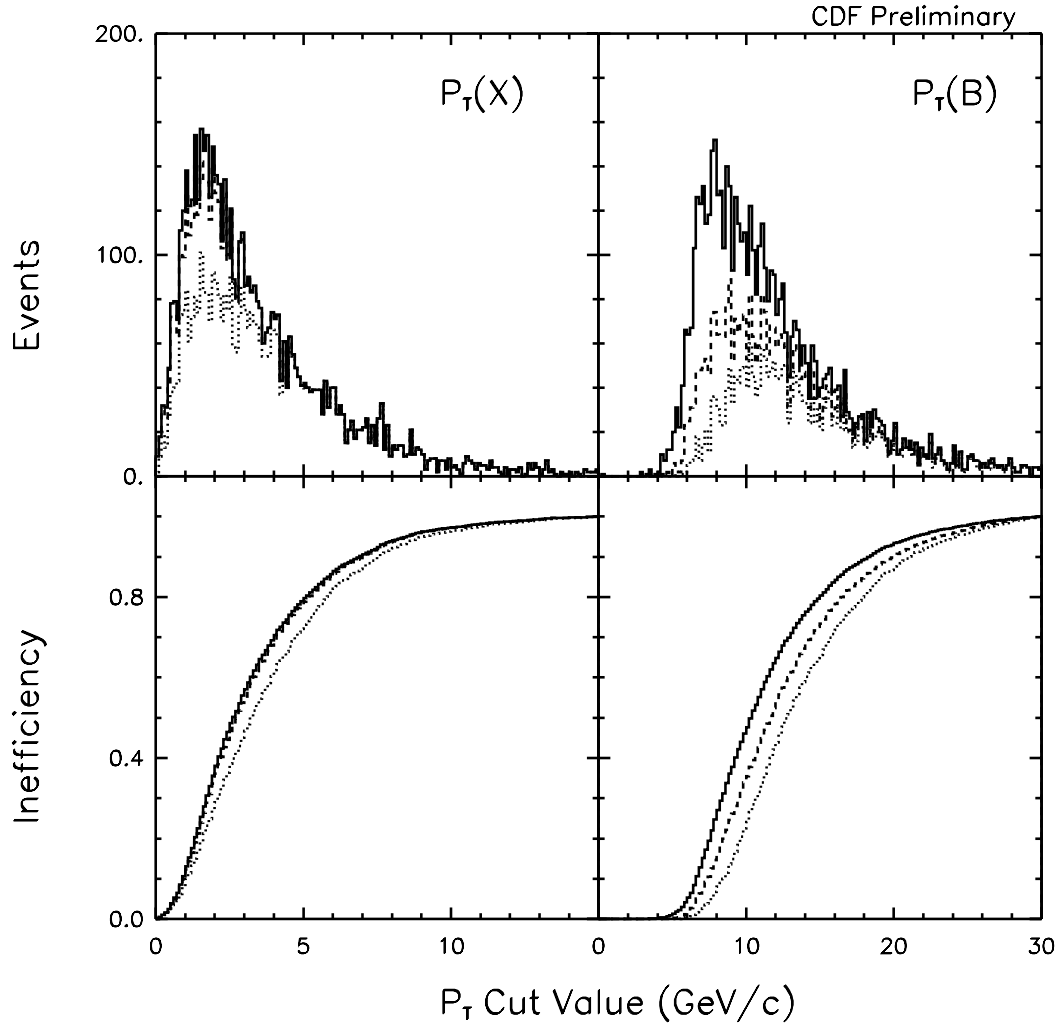

Figure 5.9: The solid histogram shows the Monte Carlo P_T distribution and inefficiency for preserving signal by making a cut on the P_T of (a) the daughter meson and (b) the B meson. The histogram shows the inefficiency given that (a) $P_T(B) > 6$ (dashed) and $P_T(B) > 8$ GeV/c (dots) and (b) $P_T(X) > 2$ (dashed) and $P_T(X) > 3$ (dots) GeV/c.

5.4.3 Expected CL(χ^2) Distribution for Signal

If the track parameters and the covariance matrix are accurately described, the "χ^2" from the constrained fit should be distributed as a true χ^2. A test of our understanding of this distribution is seen if one converts the "χ^2" distribution into a CL(χ^2) distribution which is expected to be uniformly distributed from zero to one. Figure 5.10 shows the CL(χ^2) distribution for dimuons of J/ψ candidates and for dimuons in the sideband region after a vertex constrained fit. The dimuons for J/ψ decays are expected to originate from a common vertex while the sideband dimuons are expected to consist of cases where both muons are produced from a common vertex (such as a Drell-Yan process) and are produced from distinct vertices (such as the dimuons coming from two separate long-lived semileptonic decays). In the latter case, we expect a low CL(χ^2) since the constraint is likely to grossly adjust the track parameters to satisfy the constraint. In examining Fig. 5.10, the CL(χ^2) distribution for the J/ψ signal is relatively flat indicating that the covariance matrix does a reasonable job in describing the uncertainties on the measured track parameters. There is some excess for CL(χ^2) below 25% and especially below 1%. Approximately 2.5% of real J/ψ dimuons have a CL(χ^2) after a vertex constraint of less than 1%. However, the CL(χ^2) distribution for the sideband dimuons shows a clear enhancement at low values and a cut on CL(χ^2) at 1% would enhance S/N with a small inefficiency. The CL(χ^2) distribution for $B \to J/\psi\ X$ decays will be described in the next chapter.

5.5 Combinatoric Background Reduction

In the reconstruction of exclusive B final states, there exist large combinatoric backgrounds due to combining tracks with a J/ψ candidate. In this analysis, the combinatoric background is defined as the background level in mass distributions after imposing minimal selection requirements on the kinematic quantities. These minimal requirements are arbitrary but allow one to study the effect of more stringent requirements used to observe the signal. Table 5.3 lists the requirements for the different decay channels along with the measured background level in a 10 MeV/c^2 bin at the nominal B meson mass. For $B^- \to J/\psi\ K^-$, the combinatoric background level depends upon the P_T distribution of tracks in J/ψ events. The background level under B^0 and B_s^0 depends upon the two tracks forming the $K^* \to K^\pm\ \pi^\mp$ or $\phi \to K^+\ K^-$ respectively. Figure 5.11 shows the invariant mass distributions for K^* and ϕ candidates such that when combined with a J/ψ fall in $\pm$ 200 MeV/c^2 windows about nominal B^0 and B_s^0 masses and pass the minimal selection criteria. From this figure, the combinatoric background is much less for B_s^0 compared with B^0 because both the mass window around the ϕ

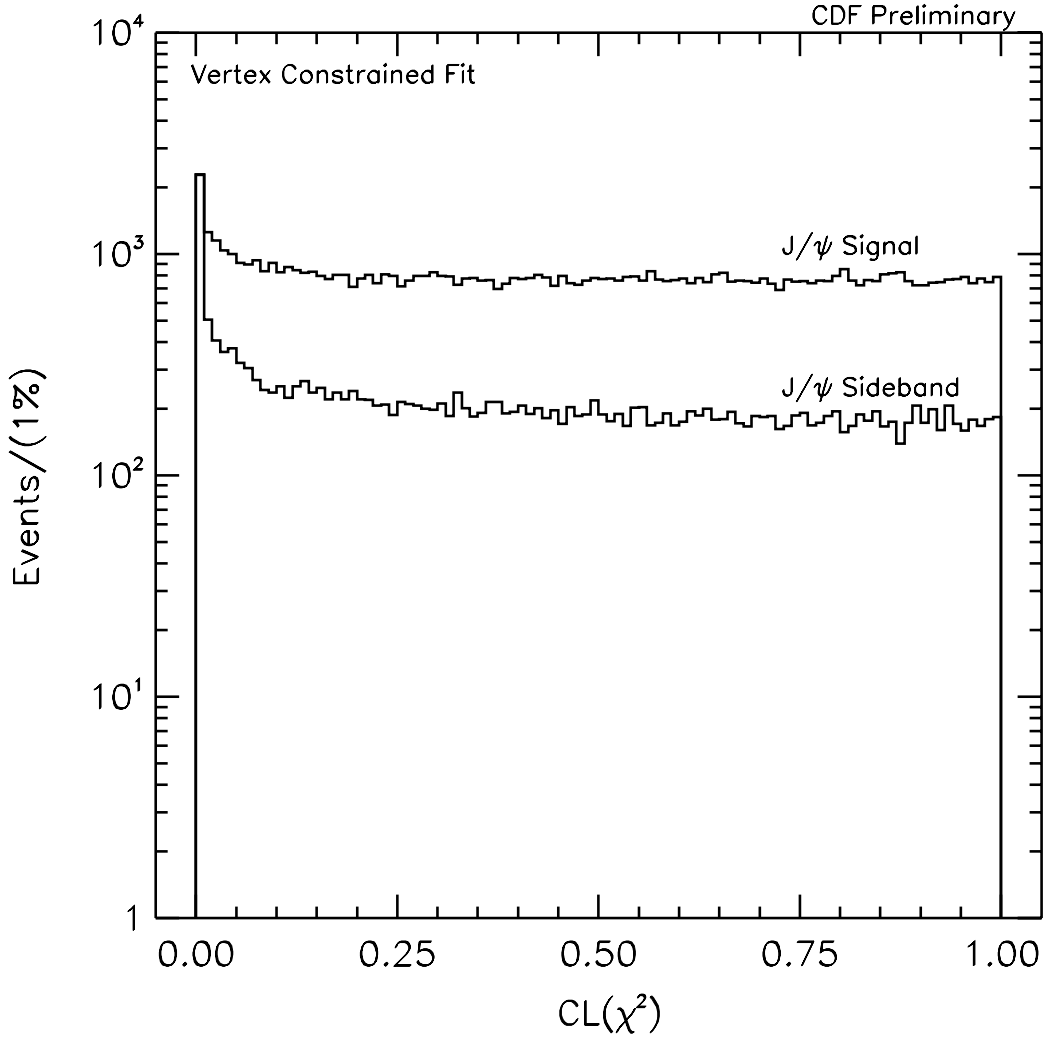

Figure 5.10: $\mathrm{CL}(\chi^2)$ distribution for dimuons from the sideband-subtracted J/ψ signal region and from the sideband region.

is smaller than that around the K^* and because the ϕ is very close to the kinematic limit when combining two particles assigned kaon masses. The final set of selection requirements will be tighter for B^0 relative to B_s^0 due to the larger B^0 background level.

Decay Mode	J/ψ Mass Window (MeV/c^2)	Daughter Mass Window (MeV/c^2)	Daughter P_T (GeV/c)	Background per 10 MeV/c^2
All modes	Track Quality Cuts			
$B^- \to J/\psi\ K^-$	$\pm$ 100		1.8	190 $\pm$ 10
$B^0 \to J/\psi\ K^*$	$\pm$ 100	$\pm$ 100	1.8	650 $\pm$ 10
$B_s^0 \to J/\psi\ \phi$	$\pm$ 100	$\pm$ 20	1.8	50 $\pm$ 7

Table 5.3: Minimal selection requirements for the reconstruction of different decay modes.

5.5.1 Kinematics for Background

Figure 5.12 shows the P_T distribution for the K^* and B^0 candidates from the upper sideband region (5.4-5.8 GeV/c^2) of the B^0 with a P_T requirement of 1.8 GeV/c on the K^*. Also shown is the effect of cutting on these distributions. Notice that the background is peaked much more at lower P_T compared with the expected signal as shown in Fig. 5.9. Imposing selection requirements on the P_T of the daughter and B mesons improves S/N for reconstructing B mesons. Table 5.4 summarizes the background rejection power on making kinematic selection requirements for the three B meson decay modes.

P_T(X) Cut (GeV/c)	1.8			2.0			3.0		
$P_T(B)$ Cut	0.0	6.0	8.0	0.0	6.0	8.0	0.0	6.0	8.0
$B^- \to J/\psi\ K^-$	100	56	26	71	43	22	20	16	10
$B^0 \to J/\psi\ K^*$	100	56	26	66	41	20	14	12	8
$B_s^0 \to J/\psi\ \phi$	100	55	26	65	40	20	13	11	8

Table 5.4: Percentage of combinatoric background events remaining for the given cuts on P_T(X) and $P_T(B)$ relative to P_T(X)$>$ 1.8).

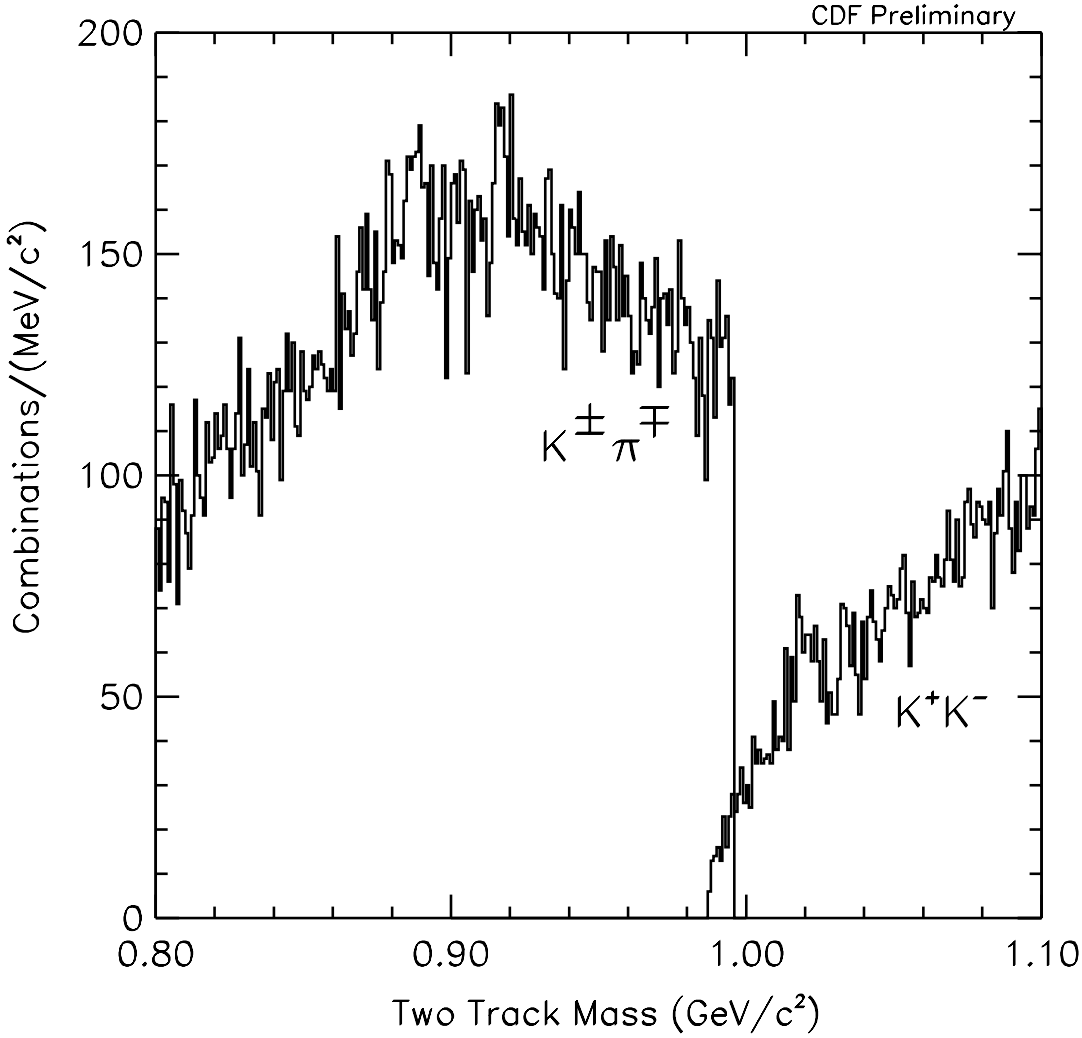

Figure 5.11: Two track mass distribution for K^* and ϕ candidates of B^0 and B_s^0 decays respectively.

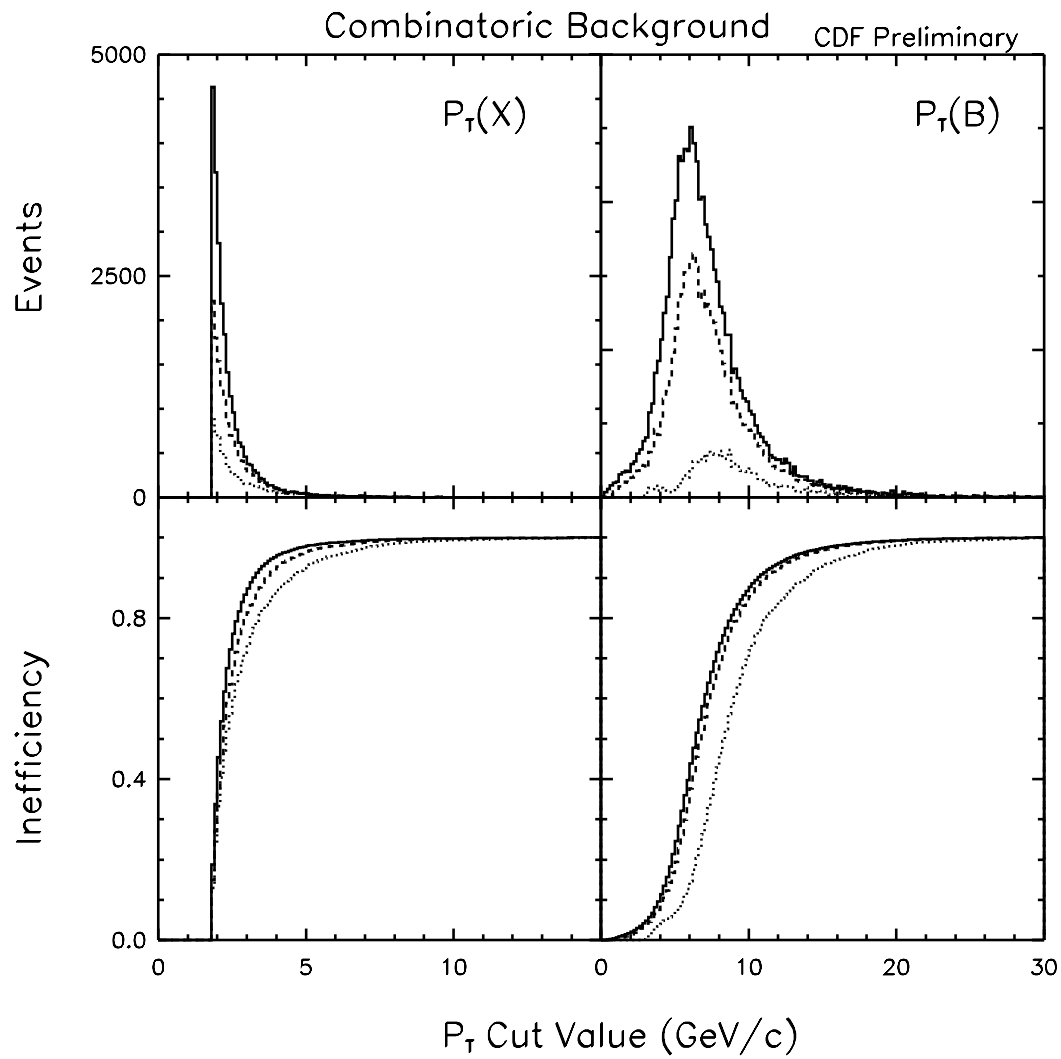

Figure 5.12: The solid histogram shows the combinatoric background P_T distribution and inefficiency when making a cut on the P_T of (a) the daughter meson and (b) the B meson. The histogram also shows the inefficiency given that the (a) $P_T(B) > 6$ (dashed) and $P_T(B) > 8$ GeV/c (dots) and (b) $P_T(X) > 2$(dashed) and $P_T(X) > 3$(dots) GeV/c. Notice that a P_T cut at 1.8 GeV/c on the daughter meson has already been applied.

5.5.2 $c\tau$ for Background

Figure 5.13 shows the $c\tau$ distribution for the upper sideband region of B^0 candidates passing the minimal selection criteria separated into groups that have fewer than 2 associated SVX tracks or with 2 or more matched SVX tracks. The distributions for B^- and B_s^0 candidates are very similar and the background rejection is summarized in Table 5.5. A Gaussian fit of the peak region gives a resolution for $c\tau$ of 170 μm for the case when less than 2 SVX tracks are used and a resolution of 60 μm for the case when 2 or more tracks have SVX information. In terms of background rejection, the SVX helps little relative to only using CTC information unless one requires a large positive lifetime relative to the resolution (100 μm, for instance).

	CTC+SVX			< 2 SVX tracks			≥ 2 SVX tracks			% ≥ 2 SVX tracks
$c\tau$ Cut (μm)	none	0	100	none	0	100	none	0	100	
$B^- \to J/\psi\ K^-$	100	54	29	100	53	41	100	55	20	58
$B^0 \to J/\psi\ K^*$	100	54	31	100	54	44	100	55	24	68
$B_s^0 \to J/\psi\ \phi$	100	55	32	100	56	46	100	55	25	66

Table 5.5: Percentage of combinatoric background events remaining after the given cuts on $c\tau$ for all events, for events with less than 2 SVX tracks, and for events where at least two of the tracks have SVX information.

5.5.3 CL(χ^2) for Background

Figure 5.14 shows the CL(χ^2) distribution for the upper sideband region of B^0 candidates passing the minimal selection criteria. The distributions for B^- and B_s^0 candidates are very similar. From the figure, requiring the CL(χ^2) to be larger than 1% would remove 70% of the combinatoric background. The background rejection of the CL(χ^2) cut for the three different B decay modes is summarized in Tab. 5.6. Note that more background is rejected with the CL(χ^2) requirement when four tracks are part of the constraint than with the three tracks involved in $B^- \to J/\psi\ K^-$ decays.

5.5.4 Correlations between the Selection Criteria

The effect on combinatoric background when applying each of the selection criteria have been presented independently. However, there is some correlation between

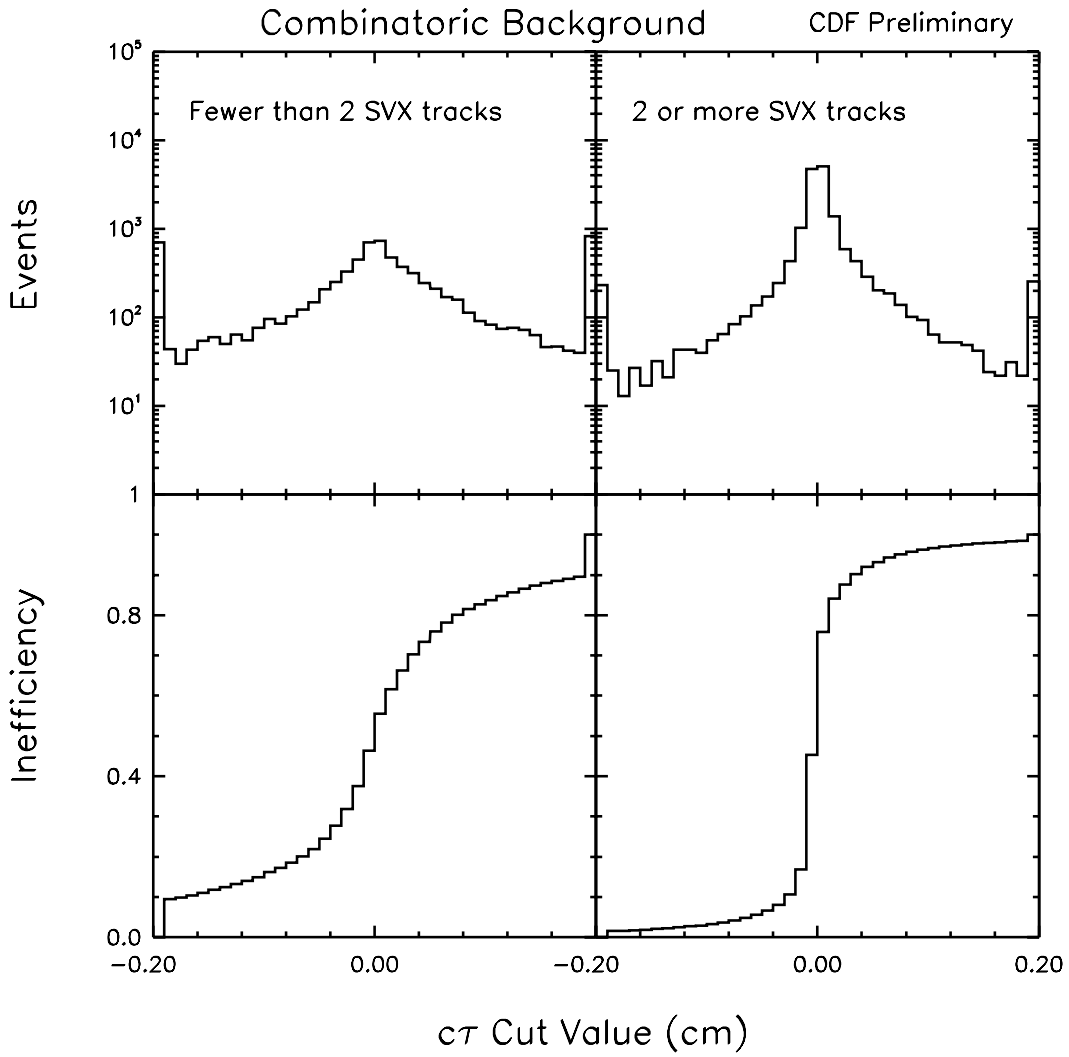

Figure 5.13: The combinatoric background $c\tau$ distribution and inefficiency when making a cut on the $c\tau$ for the upper sideband B^0 candidates having SVX information for less than 2 of the tracks and for 2 or more of the tracks. Note than underflow and overflow bins have been filled.

CL(χ^2) Cut (%)	1	5	10	20
$B^- \to J/\psi\ K^-$	46	40	36	30
$B^0 \to J/\psi\ K^*$	30	26	23	19
$B_s^0 \to J/\psi\ \phi$	30	27	24	20

Table 5.6: Percentage of combinatoric background events remaining after the given cuts on CL(χ^2) for the respective upper B sideband regions.

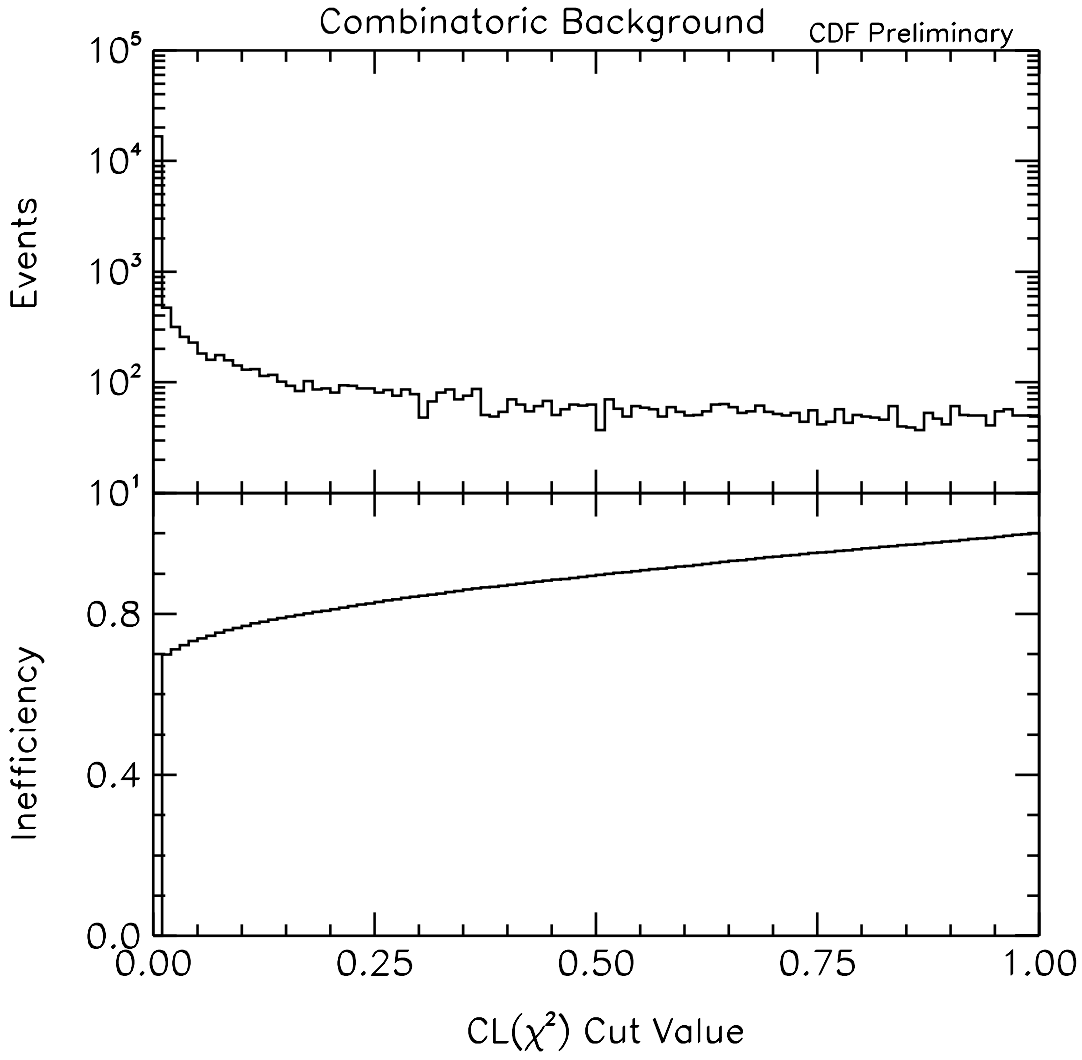

Figure 5.14: The CL(χ^2) distribution and inefficiency of the combinatoric background when making a cut on the CL(χ^2) for the upper sideband B^0 candidates.

the cuts on kinematic quantities, $c\tau$ and CL(χ^2). The expected correlation between P_T(X) and $P_T(B)$ is a direct result of the trigger bias and has already been taking into consideration in the discussion of those quantities. Figure 5.15 shows the $c\tau$ and CL(χ^2) distributions of the background candidates in the upper sideband region of B^0 separated into (solid) $P_T(B) < 6.$ GeV/c and (dashed) $P_T(B) > 8$ GeV/c (normalized). The higher P_T background candidates are slightly less likely to contribute in the very high $c\tau$ tails (positive or negative) and are also slightly less likely to contribute to the CL(χ^2) $< 1\%$ region. Figure 5.16 shows the $c\tau$ (CL(χ^2)) distributions separated into two regions of CL(χ^2) ($c\tau$). There is a higher correlation between $c\tau$ and CL(χ^2) in the background. Namely, tracks which have a poor CL(χ^2) are also more likely to contribute to the extreme tails in $c\tau$.

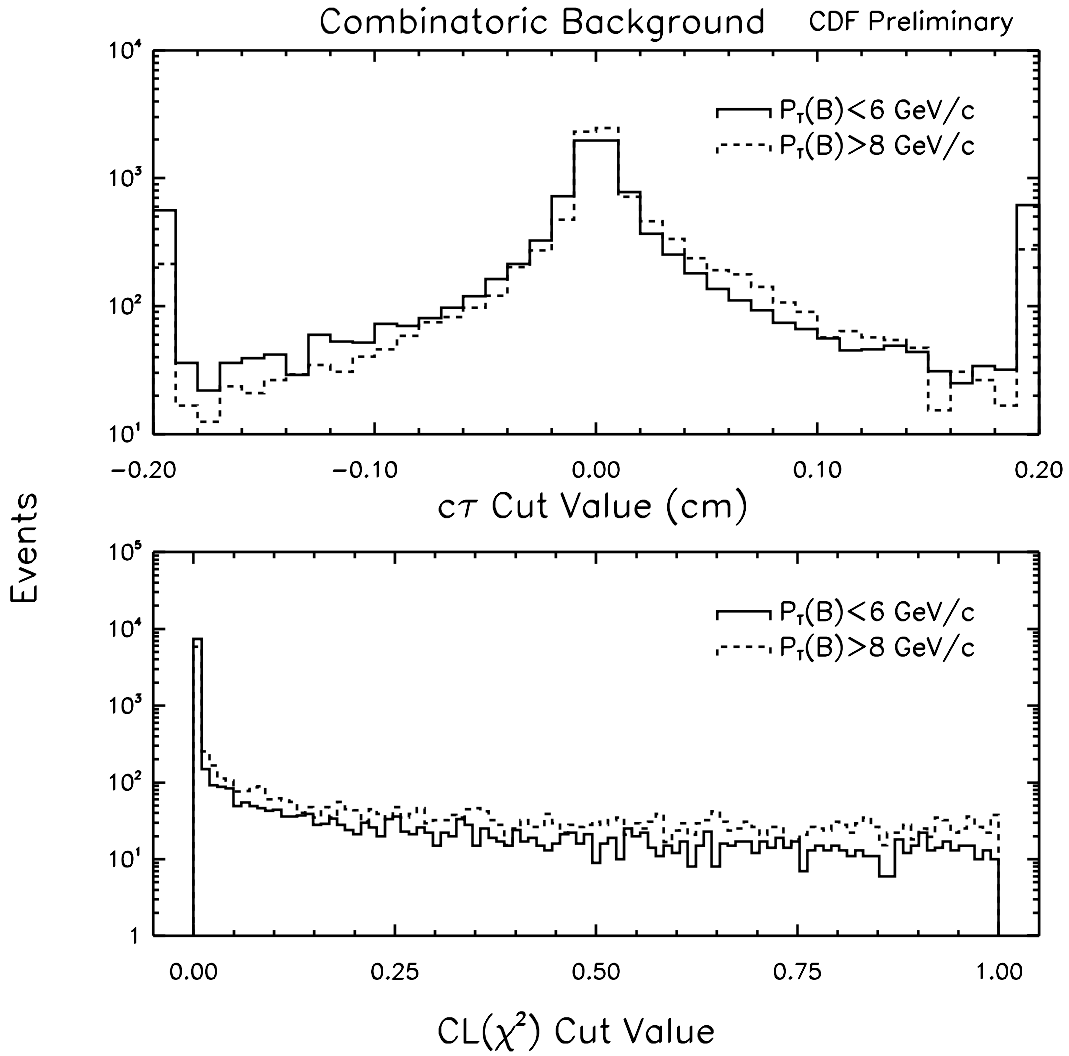

Figure 5.15: The $c\tau$ and CL(χ^2) distributions of the combinatoric background of upper sideband B^0 candidates separated into regions of low and high $P_T(B)$.

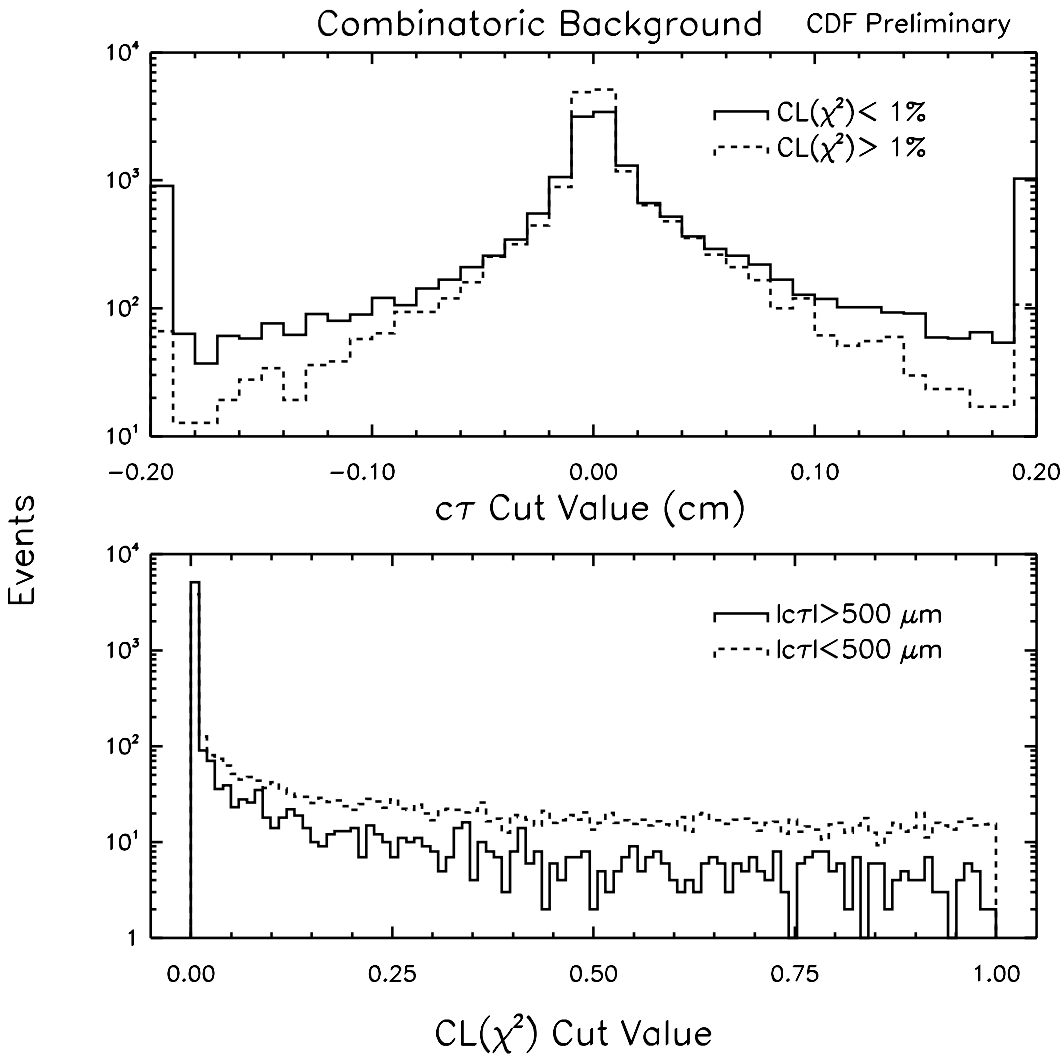

Figure 5.16: The $c\tau$ distribution (top) of the combinatoric background of upper sideband B^0 candidates separated into CL(χ^2) $< 1\%$ (solid) and CL(χ^2) $> 1\%$ (dashed). Also shown is the CL(χ^2) distribution (bottom) separated into $|c\tau| < 500$ μm (solid) and $|c\tau| > 500$ μm (dashed).

Chapter 6

Reconstruction of Exclusive B Decays into J/ψ

This chapter will show the results of applying the analysis just described on the reconstruction of exclusive B meson decays into J/ψ. A correction applied to the P_T scale will be described. Next the selection criteria used to improve S/N for the reconstruction will be quantified in terms of preserving the signal in the data and will be compared with the effects on Monte Carlo and combinatoric background distributions described in the previous chapter. The chapter ends by measuring the mass of each the B mesons and assigning a statistical uncertainty. Systematic uncertainties on the measurement will be discussed in the next chapter.

6.1 P_T Scale Correction

The transverse momentum scale is used to convert measured hits in the tracking chambers and the associated curvature into a transverse momentum. A charged track traversing the tracking chambers in the presence of a uniform magnetic field will travel in a circular path in the r-ϕ plane. The hits in the tracking chamber determine the curvature of the track which in turn is related to transverse momentum by Eq. 6.1:

$$P_T\ (GeV) = 1.5\ \times\ 10^{-4}\ \mathrm{B\ (KG)}/crv \tag{6.1}$$

where the constant is proportional to the speed of light, B is the magnetic field, and crv is the curvature. The P_T scale thus depends on the value of the magnetic field. In the default reconstruction, the magnetic field value is set to a constant of 14.116 KG based on measurements made with 5000 Amps current in the solenoid and then extrapolating the measurement to the operating level of 4650 A. The accuracy of the magnetic field measurement was to 0.05% [41] at 5000 A. A

remeasurement of the field at 4650 A suggests that 14.116 KG should be scaled up by 0.03% [60].

In addition to the magnetic field, the P_T scale also depends on a correction to the curvature due to energy losses experienced by the particle as it passes through material such as the beam pipe, SVX, cables, supports, and inner wall of the CTC. This correction can be applied as an average correction since the actual energy loss of a particle is not known. The correction depends on the velocity, amount and type of material, and type of particle. There is uncertainty in the accuracy of the material database used for dE/dx corrections in the offline reconstruction.

Studies performed in the CDF analysis of measuring the W boson mass [61] suggest that the material used for dE/dx calculations should be scaled by up $31 \pm 10\%$ based on fitting the radiative tail in Z^0 decays to dielectrons. The studies also suggest a scale factor equivalent to scaling the magnetic field by $0.074 \pm 0.071\%$ (B field equals 14.12673 KG). This scale factor is determined by looking at the Υ and J/ψ masses with the uncertainty coming from the material scale uncertainty, the fitting procedure, and non-uniformities in the J/ψ mass when plotted with respect to several geometrical quantities. Many of the effects also impact the mass measurement of B mesons and will be discussed in the next chapter.

Figures 6.1, 6.2 show the reconstructed $J/\psi \rightarrow \mu^+ \mu^-$ and $\Upsilon \rightarrow \mu^+ \mu^-$ before and after these corrections are applied. The J/ψ mass is determined by fitting a double Gaussian with a single mass parameter. The Υ masses are determined, after using a vertex and pointing constraint, by fitting the linear background and Gaussian signals to approximately 15 pb^{-1} of data. For the Υ candidates, one muon is required to have $P_T > 2.5$ GeV/c, both muons are required to have $P_T > 2$ GeV/c, and the CL(χ^2) is required to be larger than 1%. The uncorrected masses are lower than the world averages while the corrected masses agree within uncertainties to the world averages. The P_T corrections consisting of scaling the magnetic field and increasing the amount of material used in dE/dx calculations are applied when reconstructing B mesons. Uncertainties associated with these corrections will be treated as systematics in the next chapter.

6.2 Selection Criteria

Requirements are made on the transverse momentum of the daughter and B mesons, the lifetime, and the CL(χ^2) coming from the constrained fit. The effect of these cuts on combinatoric background has been described in the previous chapter using the background region above the B meson peak. In this chapter, we can study each of the quantities by looking at the effect on the signal region (after subtracting the normalized upper sideband region). Each criteria with the

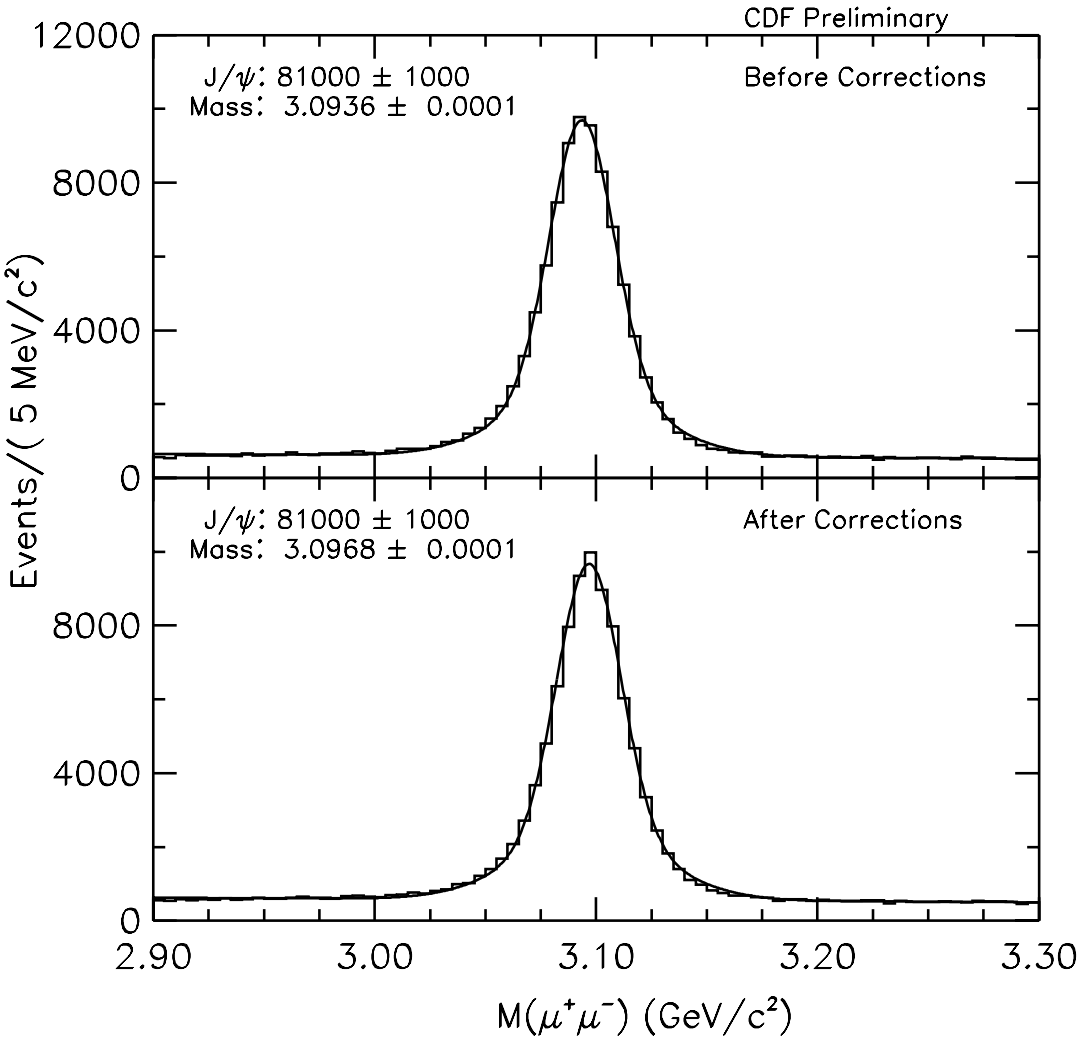

Figure 6.1: Dimuon mass distribution for J/ψ candidates before and after transverse momentum scale corrections.

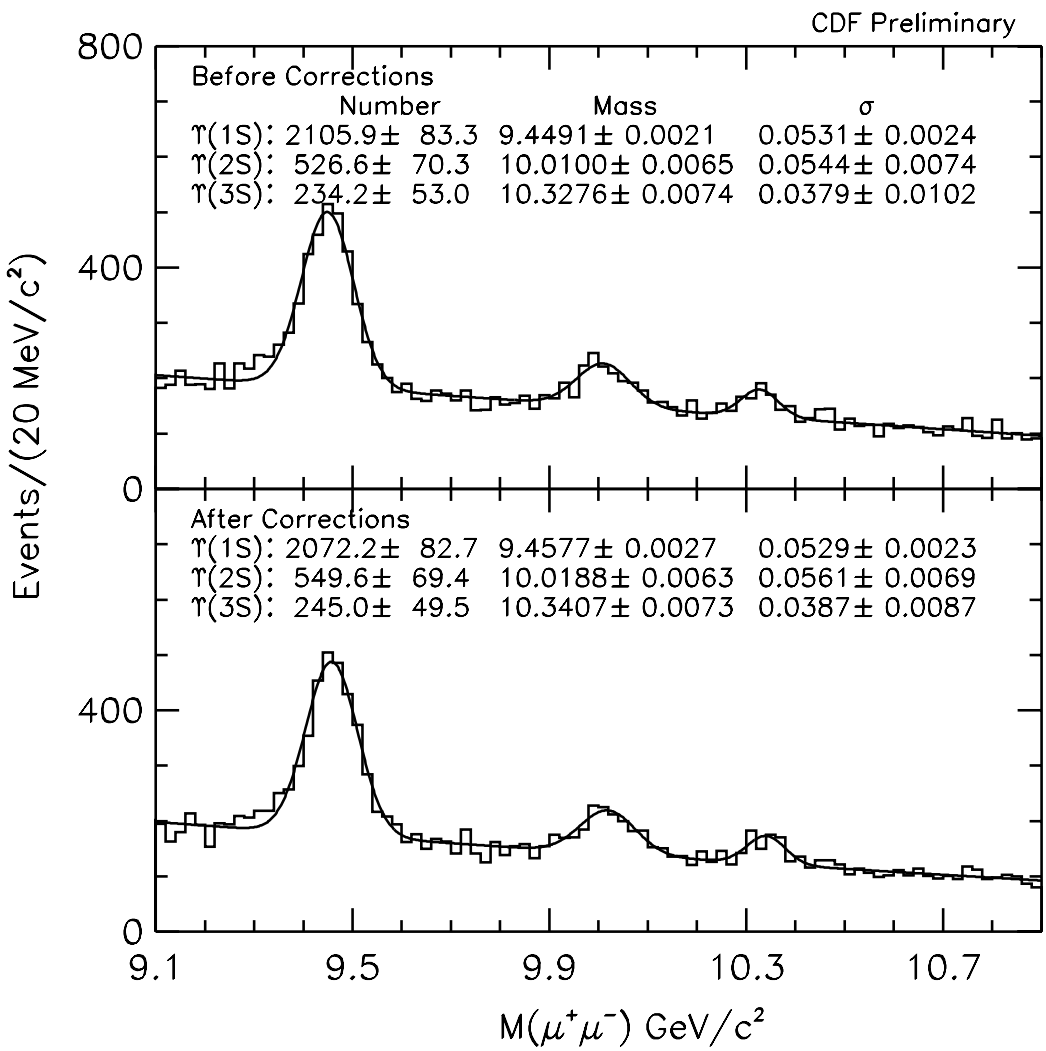

Figure 6.2: Dimuon mass distribution for Υ candidates before and after transverse momentum scale corrections.

cut value is displayed. In addition, the efficiency for preserving signal for the cuts is calculated from the data. The philosophy used to choose the particular set of cuts for the reconstruction of each of the B mesons is based upon optimizing signal-to-noise. However, for the mass measurement, the specific selection criteria has little effect. After demonstrating the power of these cuts to provide clear B meson signals, the resulting mass distributions will be fit to determine the mass.

6.2.1 B Reconstruction

Table 6.1 lists the final set of cuts which will be used for each of the B mesons. The table also lists the signal and sideband regions which will be used in the following discussion to display the quantities on which cuts are imposed. The exact cut values have been chosen first by obtaining good signal-to-noise for the B^- and B^0 signals in the first half of the CDF data. Studies of the P_T cuts using Monte Carlo simulation of B production guided the optimization of the kinematic requirements. The $c\tau$ cut has been chosen based upon the expected picosecond lifetime of the B mesons and the effect of the cut on background. The CL(χ^2) cut has been chosen based upon its improvement of the B^- and B^0 signals. Due to the larger background under the B^0 peak as seen in Fig. 5.11, the $P_T(K^*)$ requirement is more stringent than the $P_T(K)$ requirement for B^-.

The B_s^0 signal is small and care has been taken to insure that cuts have not been chosen to enhance a background fluctuation. That is, if cuts are tuned to obtain the *best-looking* B_s^0 peak, the possibility exists that more background events entered the signal region relative to the sideband region due to random event fluctuations. Rather than tuning on the signal, the specific requirements for $B_s^0 \to J/\psi\ \phi$ is based upon the above optimization in B^- and B^0 reconstruction along with Monte Carlo studies. The Monte Carlo studies show that the kinematics of $B_s^0 \to J/\psi\ \phi$ decays are very similar to $B^0 \to J/\psi\ K^*$ decays as expected. Because the combinatoric background is small for the $J/\psi\ \phi$ candidates relative to the $J/\psi\ K^*$ channel, looser requirements on the kinematic quantities and $c\tau$ have been chosen for B_s^0 reconstruction. The cuts used for all three B mesons are nearly identical to those used for the previous CDF result based upon the first half of the CDF data [62]. In terms of the mass measurement, the specific selection criteria will be varied and the resulting uncertainty will be quantified in Chapter 7. Figures 6.3, 6.4, 6.5 show the mass distributions of the B candidates with successive application of the final cuts in the order of CL(χ^2), P_T(X), $P_T(B)$, and $c\tau$.

B Meson	Selection Quantity CL(χ^2) (%)	P_T(X) (GeV/c)	P_T(B) (GeV/c)	$c\tau$ (μm)	Signal Window (GeV/c^2)	Sideband Window (GeV/c^2)
B^-	1	2	8	100	5.22 – 5.32	5.4 – 5.8
B^0	1	3	8	100	5.22 – 5.32	5.4 – 5.8
B_s^0	1	2	6	positive	5.22 – 5.32	5.5 – 5.9
	K^* within $\pm$ 50 MeV/c^2 of 896.1 MeV/c^2					
	ϕ within $\pm$ 10 MeV/c^2 of 1019.4 MeV/c^2					

Table 6.1: Final selection criteria used to reconstruct B mesons. Also shown are the mass windows used to define the B meson signal and sideband regions.

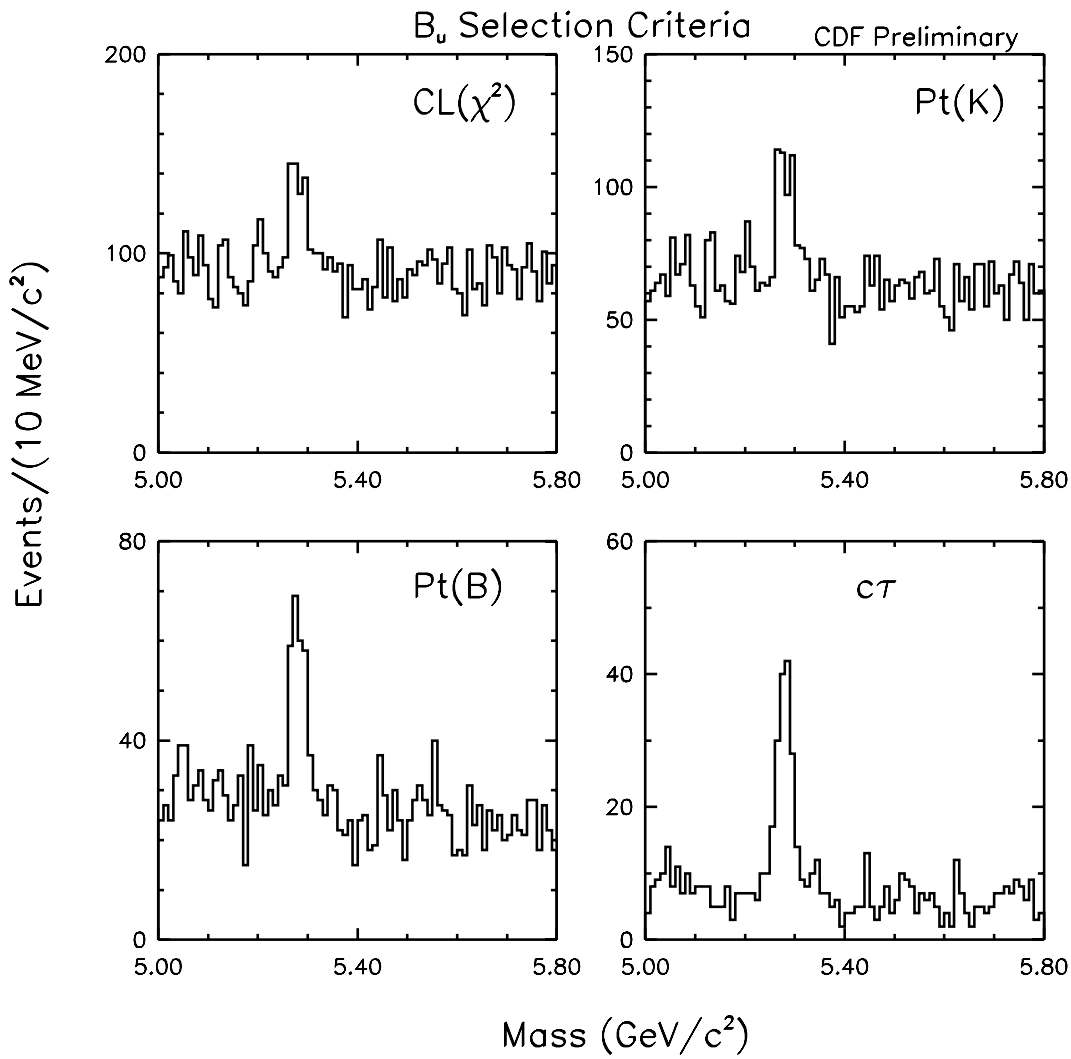

Figure 6.3: Mass distribution of the $J/\psi\ K^-$ candidates with successive applications of the cuts listed in Table 6.1.

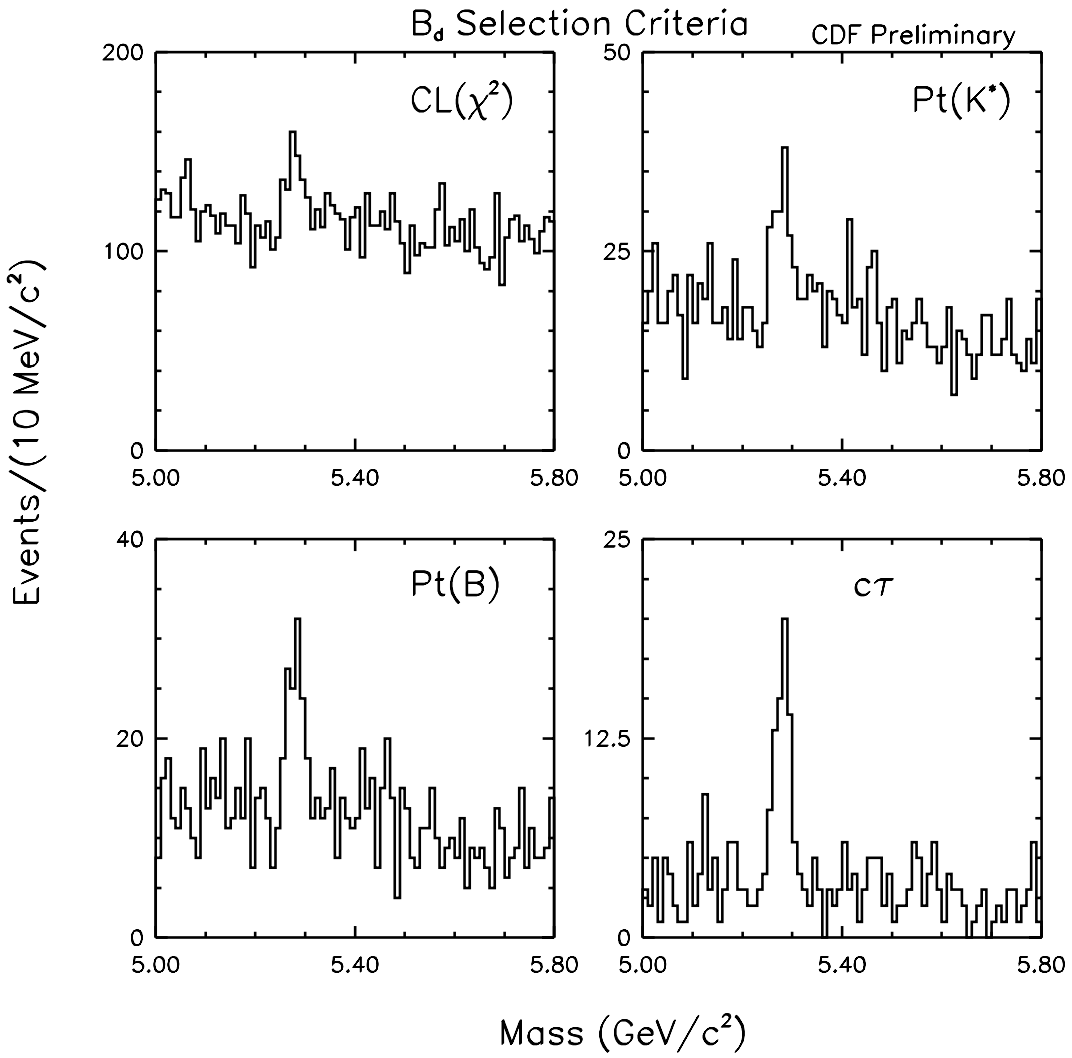

Figure 6.4: Mass distribution of the J/ψ K^* candidates with successive applications of the cuts listed in Table 6.1. The K^* candidate is required to be within 50 MeV/c^2 of the K^* mass world average.

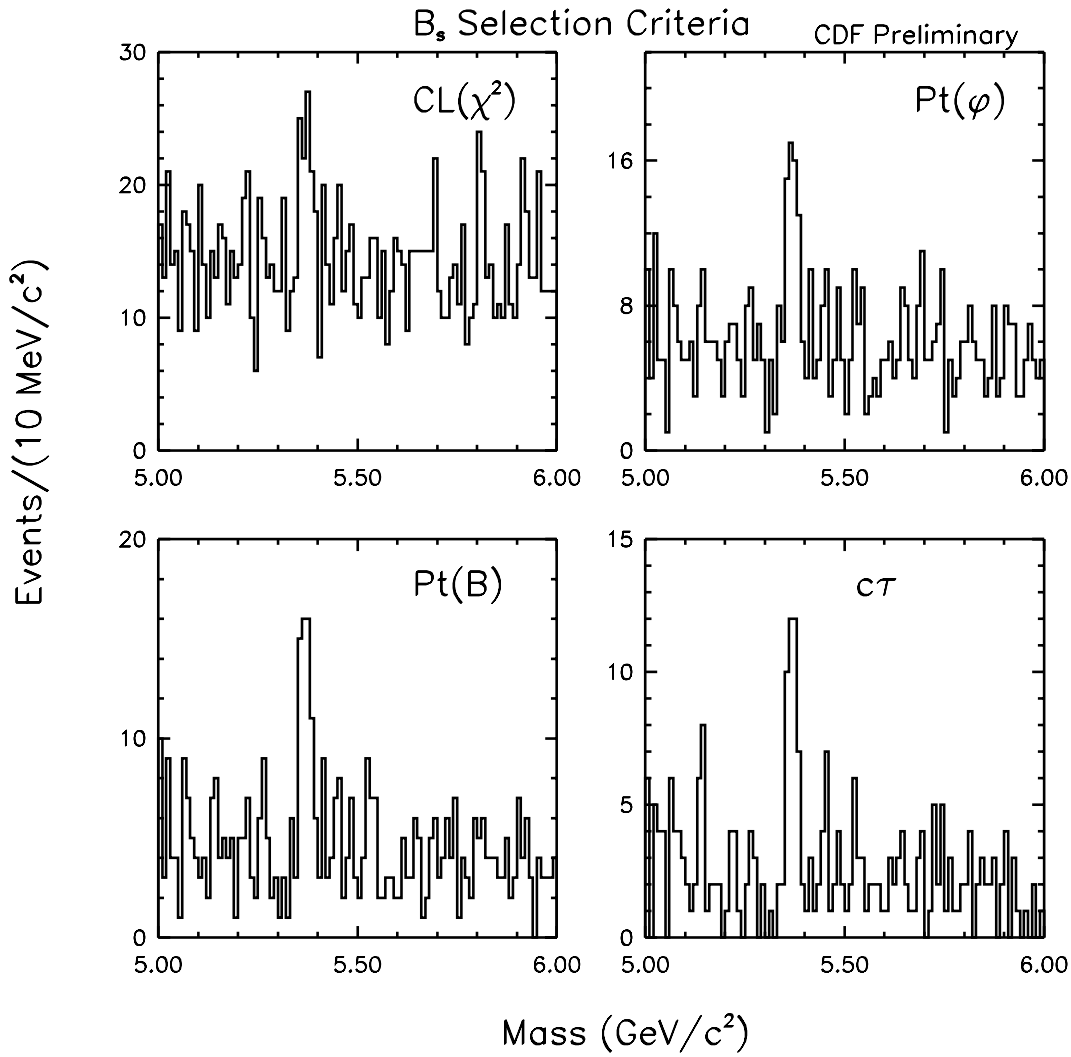

Figure 6.5: Mass distribution of the J/ψ ϕ candidates with successive applications of the cuts listed in Table 6.1. The ϕ candidate is required to be within 10 MeV/c^2 of the ϕ mass world average.

6.2.2 Daughter Meson Mass Window

The window on the $K\pi$ invariant mass for K^* candidates is $\pm$ 50 MeV/c^2 about 896.1 MeV/c^2 and for ϕ candidates is $\pm$ 10 MeV/c^2 about 1019.412 MeV/c^2. For the K^* candidates, this requirement is expected to be 70% efficient based upon the Breit-Wigner natural width of the K^* (51 MeV/c^2). The natural width is large compared to the mass resolution. For the ϕ candidates, the requirement is expected to be approximately 85% efficient based upon studying the measured ϕ width in CDF. The mass resolution of the ϕ is comparable to its natural width (4.4 MeV/c^2).

6.2.3 Kinematics for Signal

Defining the sideband and signal regions as given in Table. 6.1, one can plot the P_T distributions of the candidate B events after doing a bin-by-bin subtraction of the normalized sideband region. Figure 6.6 shows the transverse momentum distribution of the daughter mesons for the various reconstructed B mesons. For this figure, the $c\tau$ and CL(χ^2) cuts have been applied, but the kinematic cuts (except the nominal P_T(X) $>$ 1.8 GeV/c) have not. The dashed line in the figure shows the P_T distribution of the daughter meson after the B P_T cut has been applied. Figure 6.7 shows the transverse momentum distribution of the B meson. The dashed line shows the distribution after applying a cut requiring P_T(X) $>$ 2 GeV/c. In order to compare the ability of the kinematic selection criteria in preserving signal, the sideband-subtracted spectra from all three B mesons are added together and the corresponding inefficiency as a function of P_T can be calculated as shown in Fig. 6.8. Comparing this figure with the combinatoric background shown in Fig. 5.9, the P_T distribution for the signal is clearly peaked at higher P_T.

For each mode, the inefficiency of a particular cut can be measured by taking the difference in the mass distribution obtained with and without a given cut. Figure 6.9 shows the $B^- \to J/\psi\ K^-$ mass distribution (top) for events which pass the standard cuts except for the kinematic cuts (a minimal $P_T(K) > 1.8$ GeV/c is implicitly applied). The figure also shows (middle) the mass distribution for events which pass the additional selection of $P_T(K) > 2.0$ GeV/c and no $P_T(B)$ requirement. Finally the figure shows (bottom) the bin-by-bin mass difference with a Gaussian fit (the width is fixed at 14.9 MeV/c^2). The fit shows that the cuts remove 22.1 $\pm$ 7.9 events from the original 187.1 fitted events so that 88 $\pm$ 4% of the signal is preserved. Table 6.2 summarizes the inefficiencies for all three decay modes in such a way that the numbers can be compared to that of the combinatoric background rejection. Within the statistical uncertainties, the values in Table 6.2 agree with the Monte Carlo expectations in the previous chapter. Clearly more background is rejected relative to signal for the specific selection criteria used in this analysis to reconstruct B mesons.

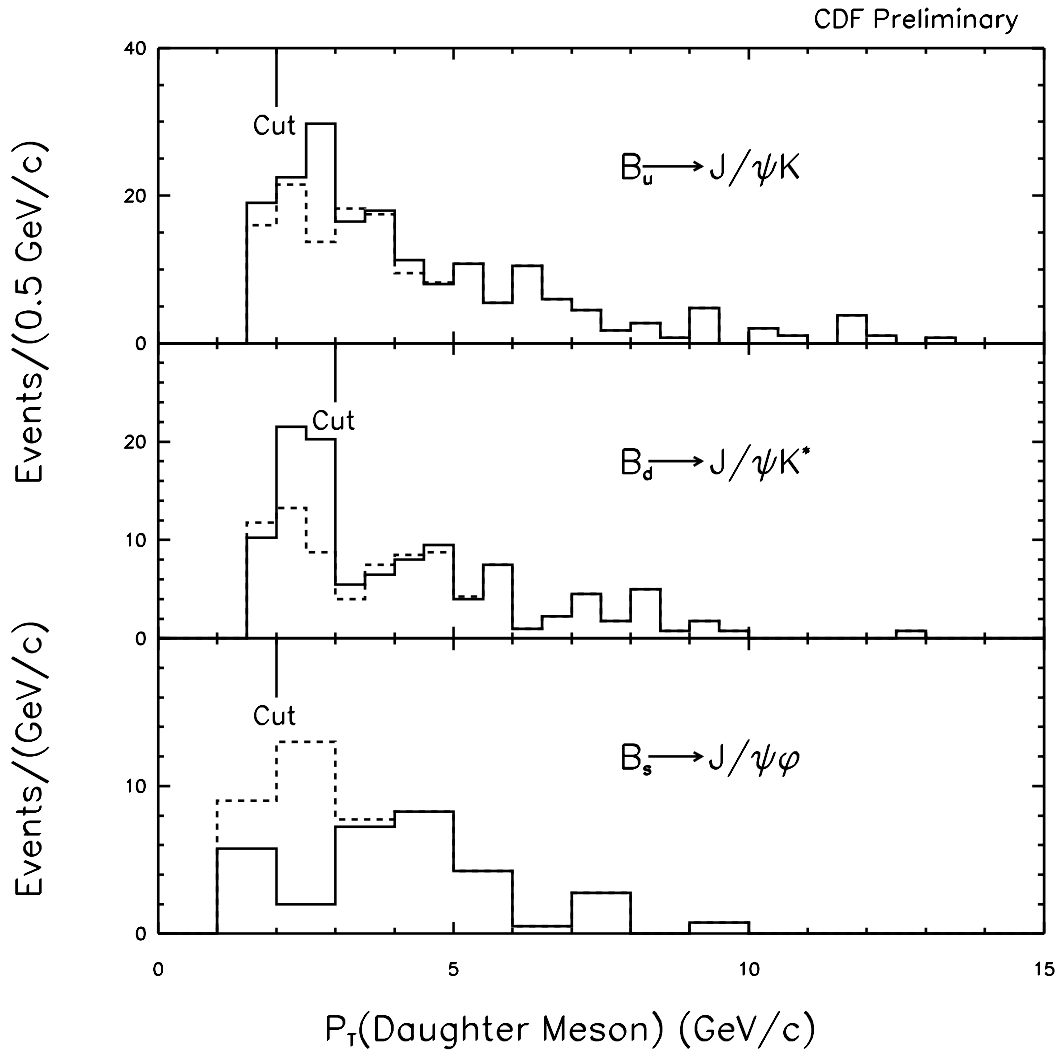

Figure 6.6: Sideband-subtracted P_T distribution for K, K^*, and ϕ coming from reconstructed B mesons. The dashed line shows the distribution when a cut on $P_T(B)$ is applied.

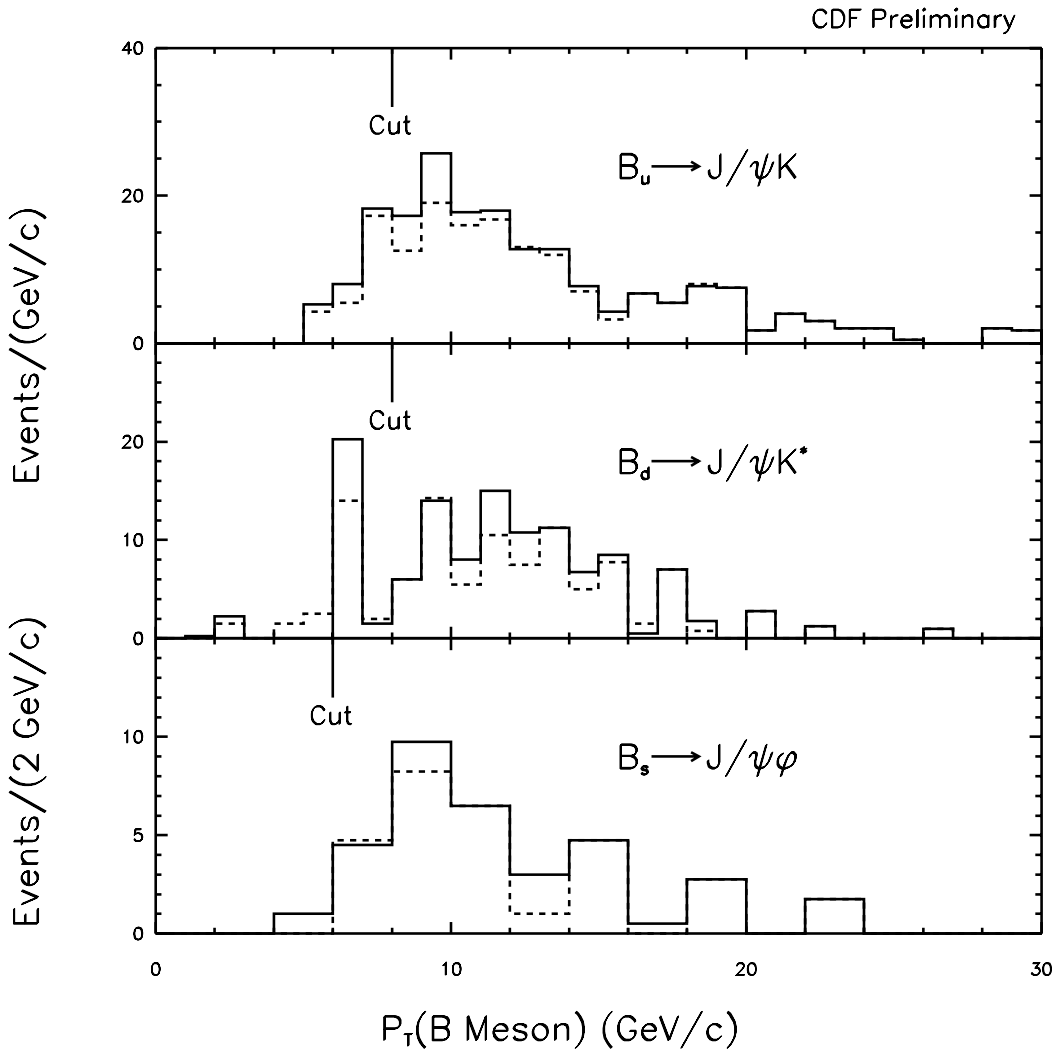

Figure 6.7: Sideband-subtracted P_T distribution for each of the reconstructed B mesons. The dashed line shows the distribution when a cut on $P_T(\mathrm{X}) > 2$ GeV/c is applied.

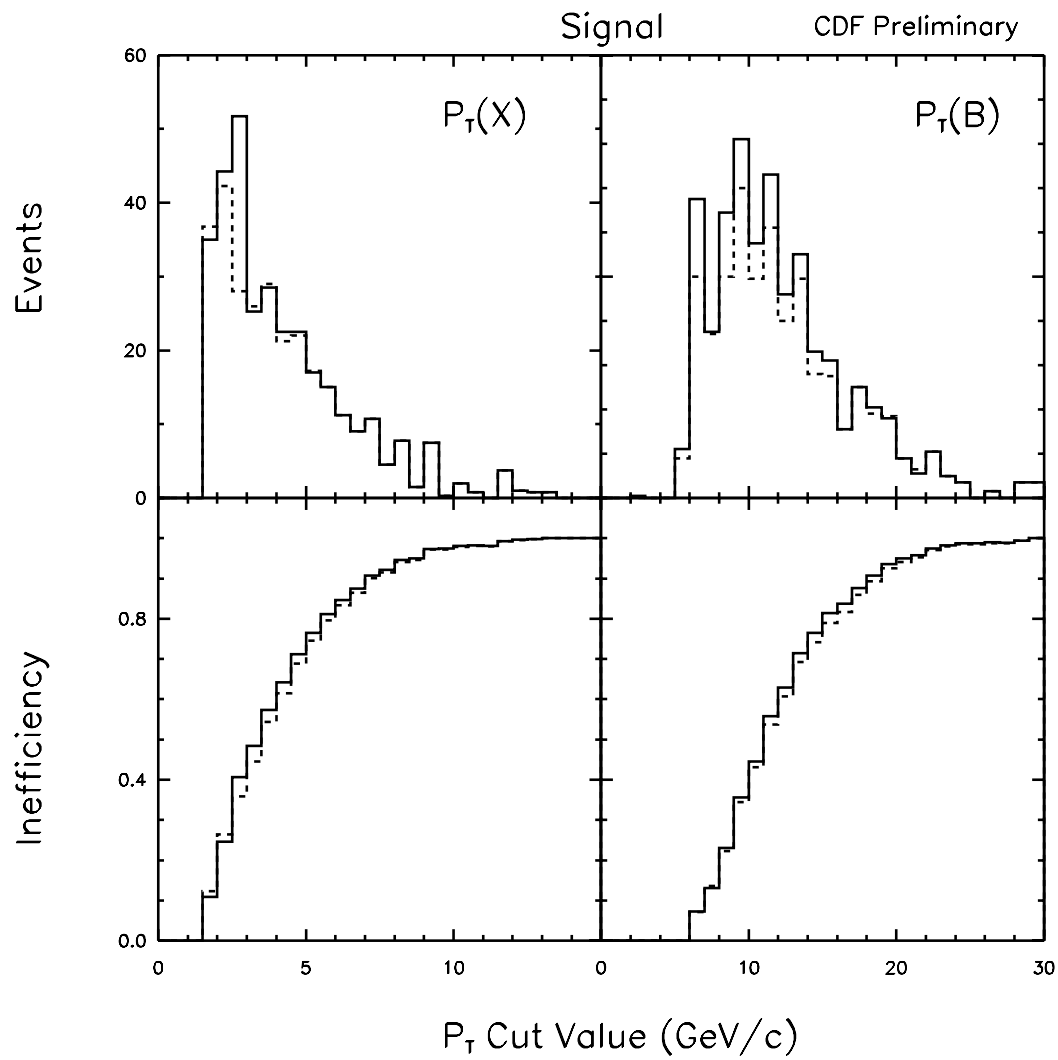

Figure 6.8: The solid histogram shows the sideband-subtracted P_T distribution and inefficiency when making a cut on the P_T of (a) the daughter meson and (b) the B meson. The histogram also shows the inefficiency given that $P_T(B) > 8$ (dashed) and (b) $P_T(X) > 2$ GeV/c (dashed). Notice that a P_T cut at 1.8 GeV/c on the daughter meson has already been applied.

P_T(X)	1.8 (GeV/c)			2.0 (GeV/c)		
$P_T(B)$	evts	6.0	8.0	0.0	6.0	8.0
B^-	187.1	93 ± 4	79 ± 6	88 ± 4	83 ± 5	73 ± 7
B^0	106.9	94 ± 6	80 ± 10	89 ± 8	85 ± 9	77 ± 11
B_s^0	40.0	95^{+5}_{-7}	75 ± 12	88 ± 10	90 ± 10	68 ± 14
P_T(X)	3.0 (GeV/c)					
$P_T(B)$	0.0	6.0	8.0			
B^-	53 ± 8	54 ± 8	51 ± 8			
B^0	48 ± 13	49 ± 13	50 ± 13			
B_s^0	65 ± 16	66 ± 16	64 ± 16			

Table 6.2: Percentage of candidate events remaining after the given cuts on P_T(X) and $P_T(B)$ relative to P_T(X)$>$ 1.8 GeV/c).

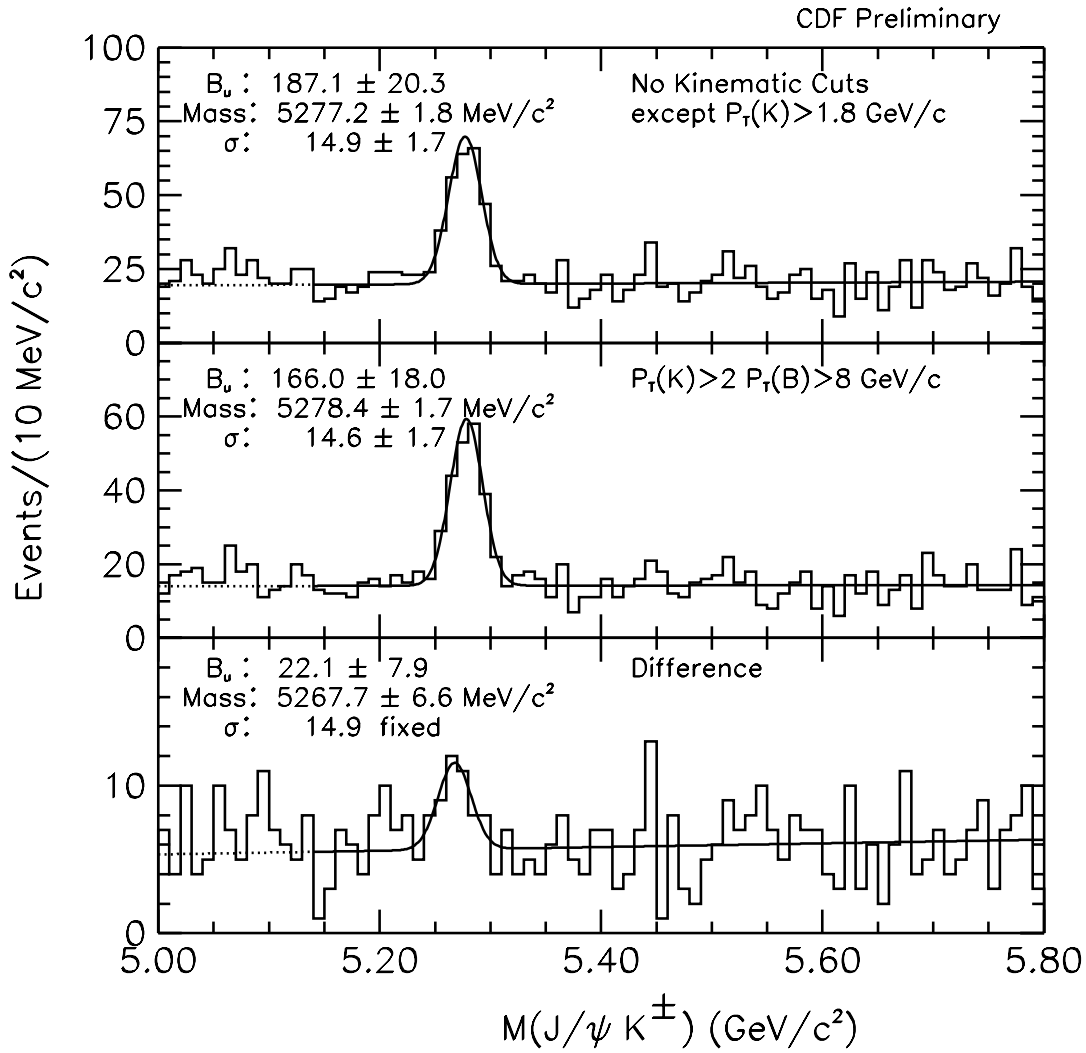

Figure 6.9: An example using $B^- \to J/\psi\ K^-$ of calculating the relative efficiency of a cut by fitting the difference in mass distributions with and without the given cuts.

6.2.4 $c\tau$ for Signal

Figure 6.10 shows the $c\tau$ distribution of each of the sideband-subtracted B meson candidates. Figure 6.11 shows the $c\tau$ distribution of B candidates obtained by adding the individual distributions for B^-, B^0, and B_s^0. The lifetimes of all three B mesons are similar within the statistical uncertainty of current measurements. The figure is divided into those reconstructed B mesons with less than 2 of the tracks using SVX information and with 2 or more of the tracks using SVX information. There is a clear enhancement at positive values of $c\tau$ as expected. When at least 2 tracks use SVX information, the $c\tau$ distribution takes the characteristic exponential shape. Table 6.3 presents the relative efficiency of making a requirement on $c\tau$. Agreeing with Fig. 6.11, the table shows that the efficiency of requiring $c\tau$ to be larger than 0 or 100 μm is not very different for the signal when SVX is or is not used. However, in the previous chapter, it was shown that when requiring $c\tau$ to be larger than 100 μm a larger percentage of the background is removed for the case when at least 2 SVX tracks are involved.

$c\tau$ Cut (μm)	CTC+SVX evts	CTC+SVX 0	CTC+SVX 100	< 2 SVX tracks 0	< 2 SVX tracks 100	≥ 2 SVX tracks 0	≥ 2 SVX tracks 100
B^-	164.3	93 ± 6	85 ± 8	87 ± 8	74 ± 11	95^{+5}_{-8}	86 ± 11
B^0	68.5	88 ± 8	86 ± 12	100^{+0}_{-21}	78 ± 21	85 ± 11	89^{+11}_{-15}
B_s^0	43.1	78 ± 11	39 ± 16	82 ± 15	65 ± 20	70 ± 15	23 ± 22

Table 6.3: Percentage of signal events remaining after the given cuts on $c\tau$ relative to no $c\tau$ cut for all events and for events with fewer than and at least two of the tracks having SVX information. The percentage of candidates with at least 2 SVX tracks is 53 ± 8, 67 ± 11, and 62 ± 12 for B^-, B^0, and B_s^0 respectively.

6.2.5 CL(χ^2) for Signal

Figure 6.12 shows the sideband-subtracted CL(χ^2) distribution for each of the reconstructed B mesons. Especially for B^0 and B_s^0 there is some peaking towards low values of CL(χ^2). This is also seen when the three distributions are added and the inefficiency as a function of a cut in CL(χ^2) is shown in Fig. 6.13. There are cases when the tracking covariance matrix does not accurately describe the measurement uncertainties between the track parameters. However, requiring the CL(χ^2) to be above a cut value improves signal-to-noise as can be observed when one compares Table 6.4 which summarizes the CL(χ^2) effect on the B signal with Table 5.6 which does the same for the background. The uncertainty in the

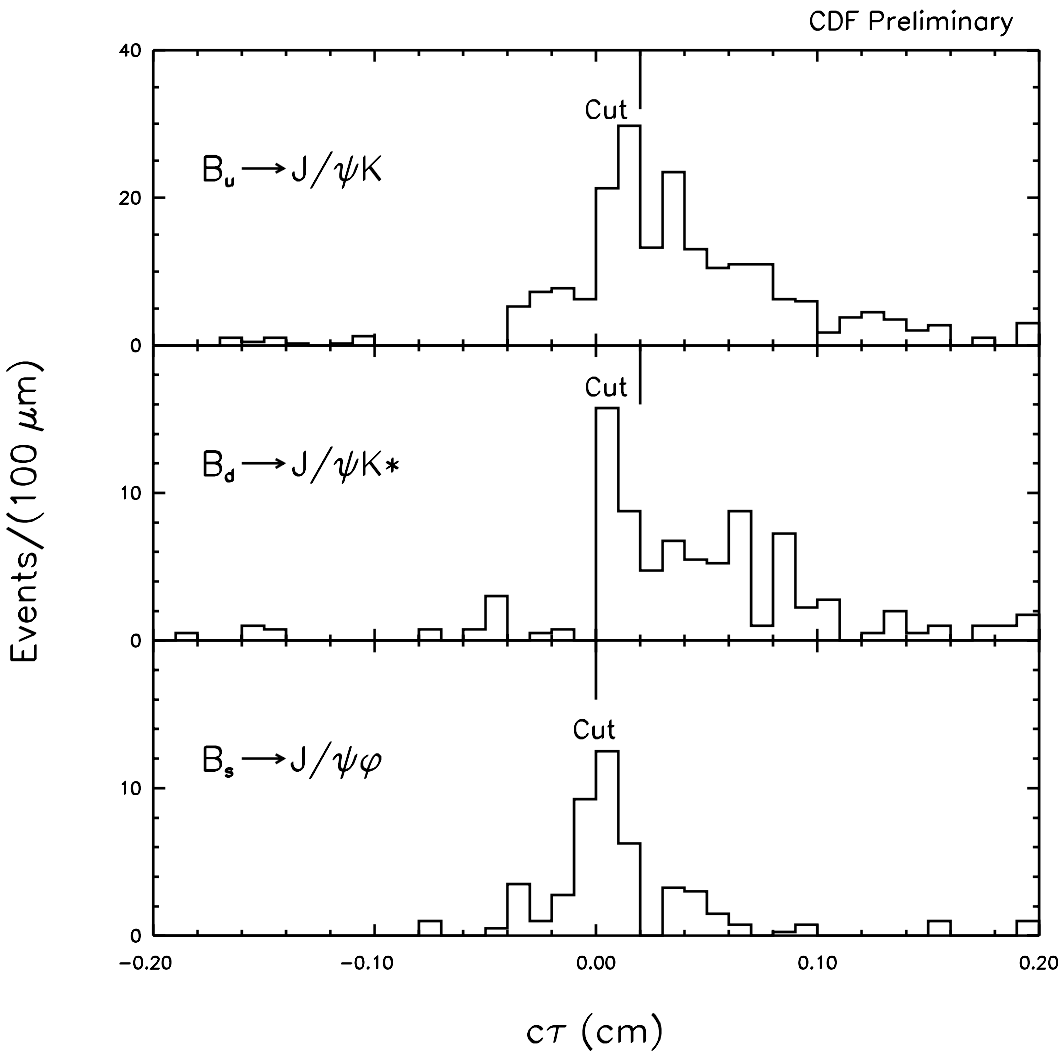

Figure 6.10: Sideband-subtracted $c\tau$ distribution for each of the reconstructed B mesons.

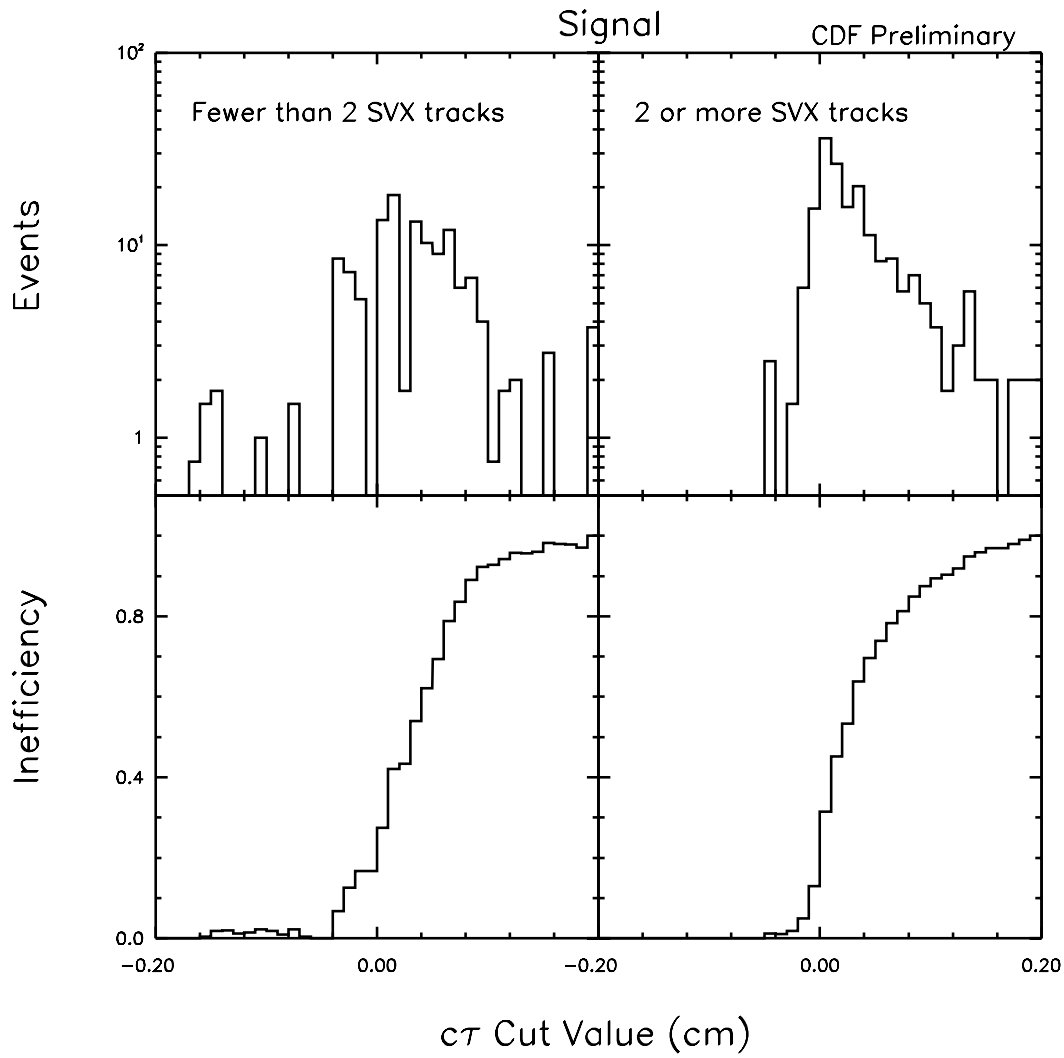

Figure 6.11: The $c\tau$ distribution obtained by adding the sideband-subtracted $c\tau$ distributions for B^-, B^0, and B_s^0 candidates. The inefficiency of making a cut on the $c\tau$ is also shown. The plot is divided into cases when fewer than two of the tracks from the B decay have SVX information and when 2 or more tracks from the decay do have SVX information.

covariance matrix is taken into account in calculating systematic uncertainties for the mass measurement.

CL(χ^2) Cut	none(evts)	1%	5%	10%	20%
$B^- \to J/\psi\ K^-$	145.8	96 ± 10	93 ± 9	84 ± 9	72 ± 8
$B^0 \to J/\psi\ K^*$	60.9	91 ± 15	85 ± 14	81 ± 13	67 ± 12
$B_s^0 \to J/\psi\ \phi$	39.9	86 ± 17	71 ± 16	53 ± 14	45 ± 13

Table 6.4: Percentage of signal events remaining after the given cuts on CL(χ^2) for each of the B decay modes. The numbers are calculated by fitting the mass distribution with the given cut and dividing by the number of signal events fitted with no CL(χ^2) cut (shown in the Table).

6.3 The Reconstruction of $B_s^0 \to J/\psi\ \phi$

Figure 6.5 shows the B_s^0 peak being enhanced by the application of the selection criteria. Further demonstration of the signal is given in Fig. 6.14 which shows the mass distribution when combining J/ψ with K^+K^- in the ϕ region and in a ϕ sideband region. In addition, Fig. 6.14 shows the K^+K^- mass distribution obtained from the B_s^0 signal region and from a B_s^0 sideband region.

6.4 Mass Measurement

6.4.1 Fitting

As mentioned previously, the mass distribution of the B meson candidates is fit to a Gaussian signal function and a linear background function. The fit is a binned likelihood fit which excludes the region larger than 140 MeV/c^2 below the nominal peak to avoid a region where possible partially reconstructed B decays with a missing final state particle might contribute. For the specific mass measurement, a bin width of 5 MeV/c^2 is chosen for all decay modes in order to reduce effects caused by a coarse binning. There are other methods of performing the fit and those are discussed in the context of contributing to the systematic uncertainty in Chapter 7.

6.4.2 Results

The mass distributions with the fits superimposed are shown in Figs. 6.15, 6.16, 6.17. The results are given in Table 6.5.

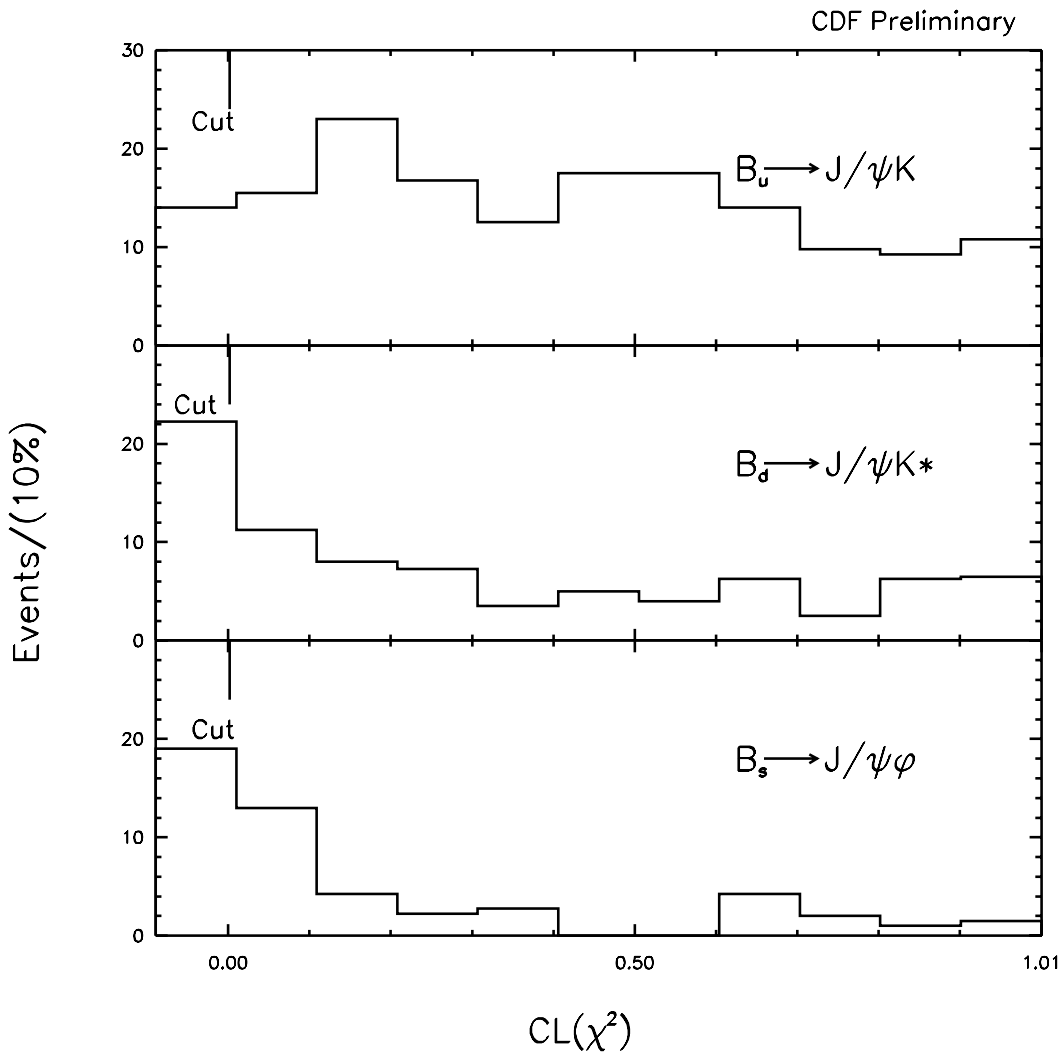

Figure 6.12: Sideband-subtracted $CL(\chi^2)$ distribution for each of the reconstructed B mesons.

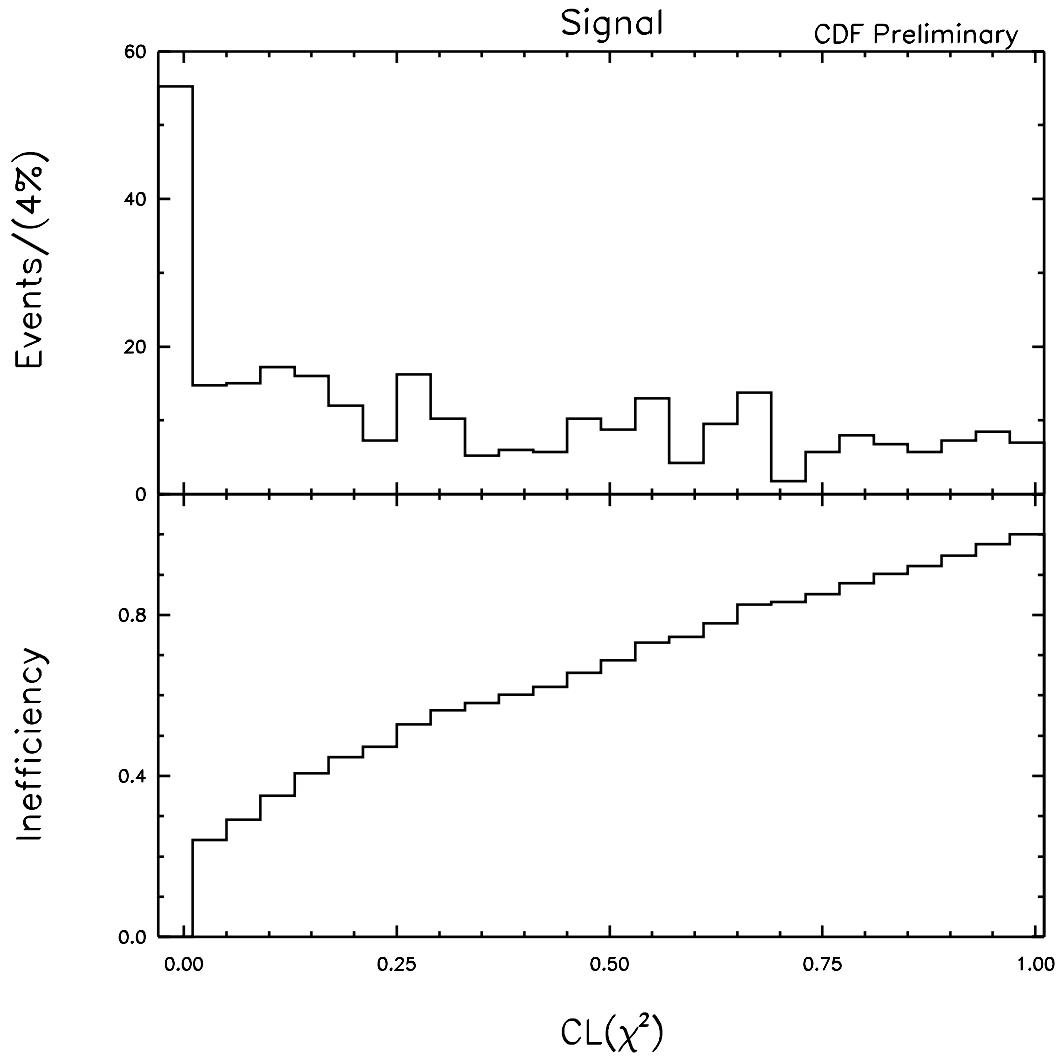

Figure 6.13: The CL(χ^2) distribution obtained by adding the sideband-subtracted $c\tau$ distributions for B^-, B^0, and B_s^0 candidates. The inefficiency for making a cut on CL(χ^2) is also shown.

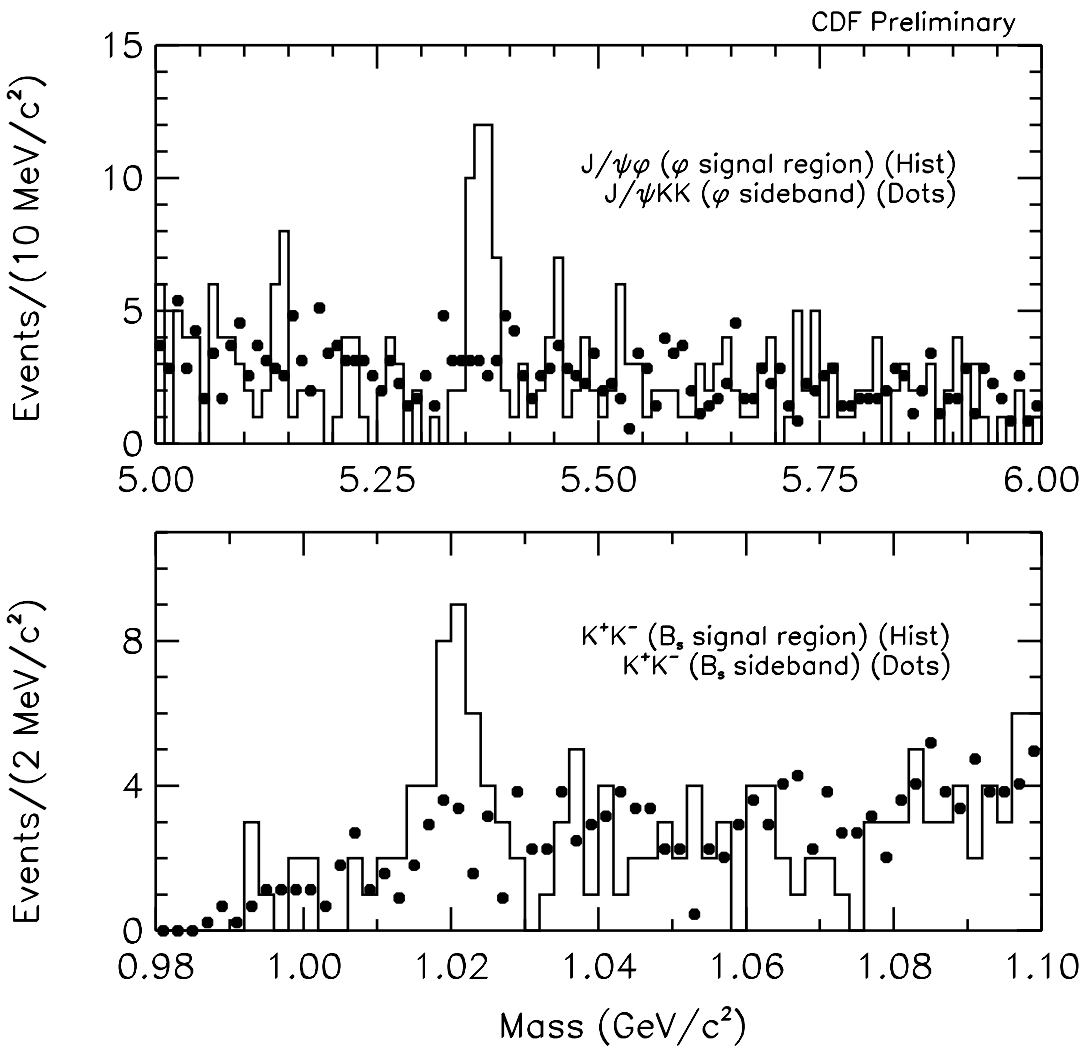

Figure 6.14: Mass distribution of the $J/\psi\ \phi$ candidates formed from K^+K^- combinations in the $\phi \pm 10$ MeV/c^2 signal and a normalized sideband region. Also shown is the K^+K^- mass distribution when selecting events around the $\pm$ 30 MeV/c^2 of the B_s^0 signal and a normalized sideband region.

B Meson	Number	Mass (MeV/c^2)	Width (MeV/c^2)	Background (per 5 MeV/c^2)	Background Slope
B^-	140 $\pm$ 15	5279.6 $\pm$ 1.7	15.2 $\pm$ 1.8	3.2 $\pm$ 0.3	-0.6 $\pm$ 0.9
B^0	57 $\pm$ 10	5279.9 $\pm$ 2.5	13.6 $\pm$ 2.2	1.7 $\pm$ 0.2	-1.1 $\pm$ 0.6
B_s^0	33 $\pm$ 7	5367.7 $\pm$ 2.4	10.5 $\pm$ 1.9	1.1 $\pm$ 0.1	-0.3 $\pm$ 0.4

Table 6.5: Results from fitting reconstructed B mesons to a Gaussian signal and a linear background shape. The background level is the level under each of the peaks.

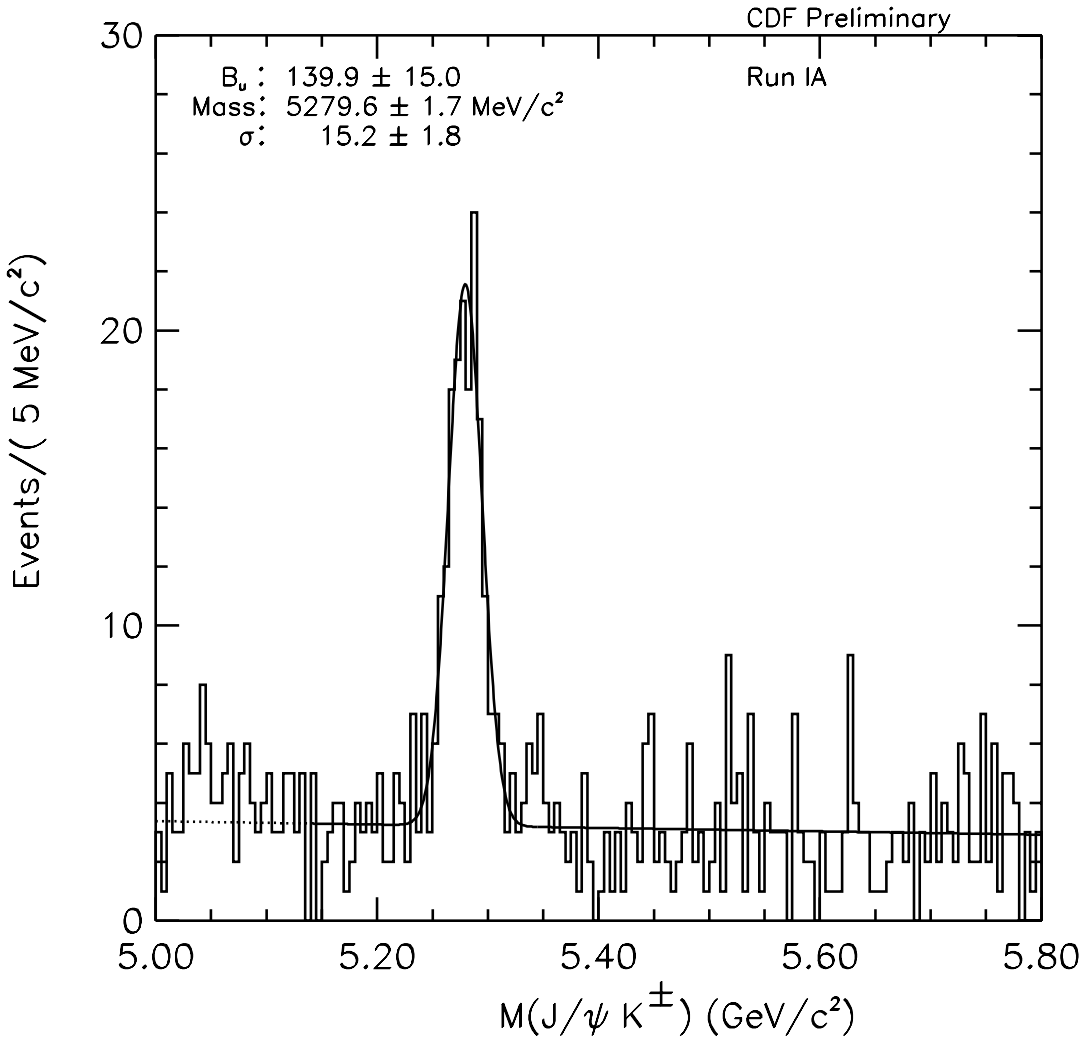

Figure 6.15: Mass distribution of $J/\psi\ K^-$ candidates using the Run IA data.

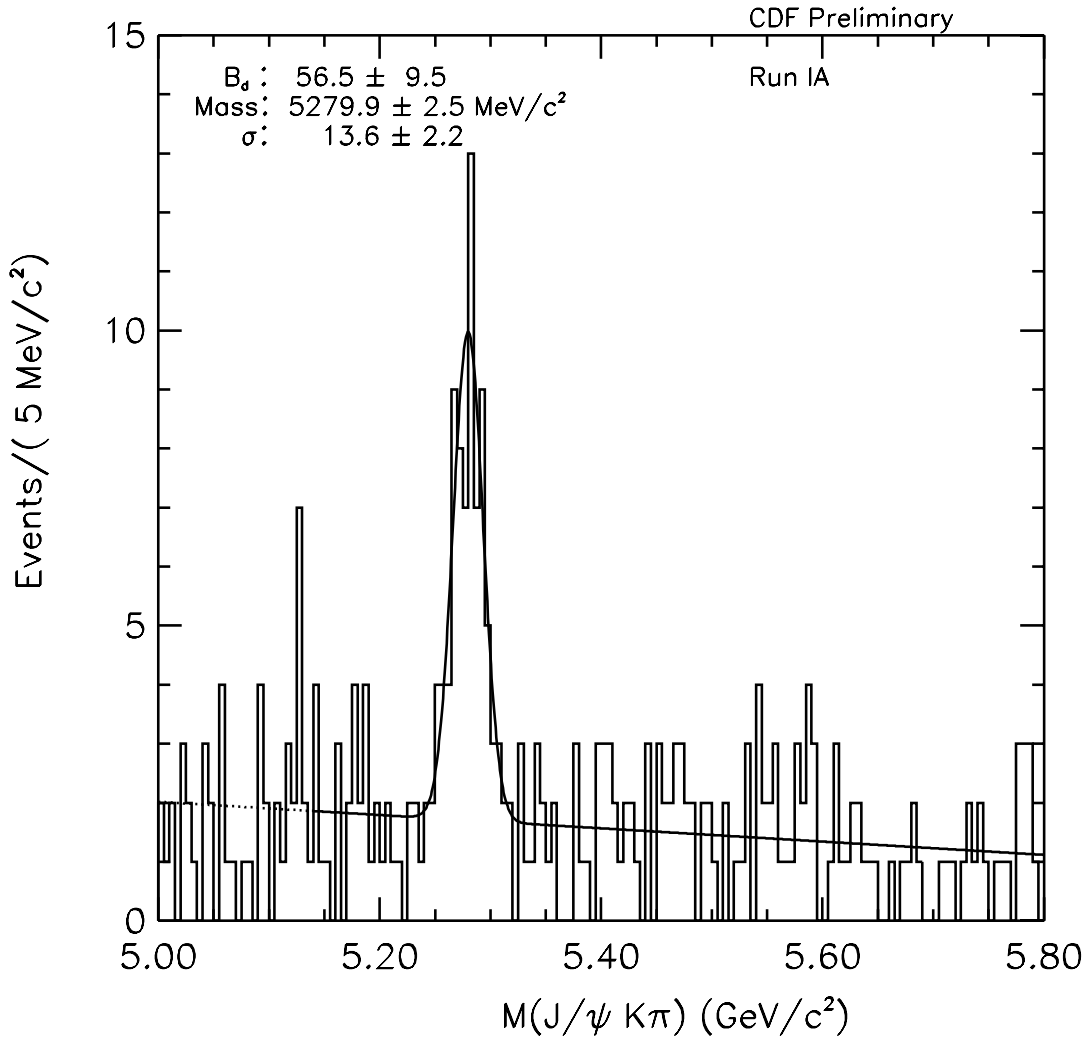

Figure 6.16: Mass distribution of $J/\psi\ K^*$ candidates using the Run IA data.

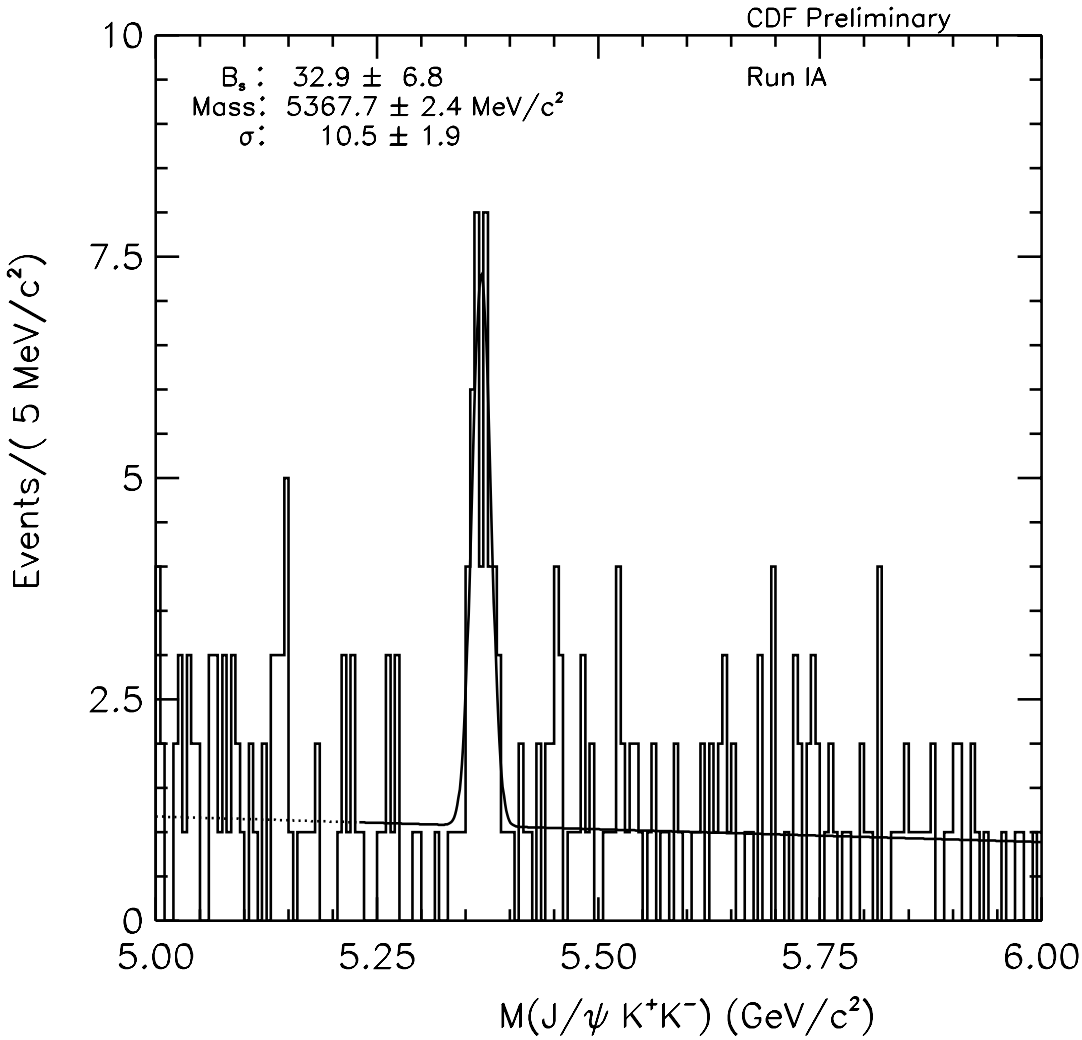

Figure 6.17: Mass distribution of $J/\psi\ K^+K^-$ candidates using the Run IA data.

Chapter 7

Systematic Uncertainties

The reconstruction of various B meson states has been described. The reconstruction involved combining tracks with J/ψ candidates and applying selection criteria to observe B meson peaks in the mass distribution. The mass distributions are fit to obtain a measure of the respective B meson mass. In the course of the description of the analysis, a number of arbitrary choices have been made; a different choice would result in a different mass value from the one quoted. In addition, there are effects in the CDF data which are understood and can impact the mass value. These contribute to the components of the systematic uncertainty which is the topic for discussion in this chapter.

7.1 Selection Criteria

The selection criteria to obtain Figs. 6.15, 6.16, 6.17 were chosen without bias with respect to the fitted mass. A *golden* mass was taken from the fit of each of these distributions. However, the choice of selection criteria was arbitrary and the fitted central mass value depends on the set of cuts. To estimate a systematic, B meson distributions are generated using different cuts on $c\tau$, the mass window for the K^* and ϕ, $P_T(\mathrm{X})$, and $P_T(B)$. Tables 7.1, 7.2 show the results from fitting each of the distributions. There is no well defined procedure to obtain a systematic. The difficulty is that the different fits are correlated and rarely vary by more than the statistical uncertainty. If the maximum deviation between the different fitted masses and the *golden* masses is taken as the systematic, the uncertainty is overestimated since part of the statistical uncertainty is double counted. In order to account for this difficulty, the estimate of the uncertainty due to the selection criteria is given by the following:

$$syst = \max(diff^2 - \sigma^2)^{\frac{1}{2}} \tag{7.1}$$

where the maximum is taken over the values in Table 7.1, 7.2 (except for B^0 masses with a statistical mass uncertainty larger than 3 MeV/c^2), *diff* is the difference between the value and the *golden* value, and σ is the statistical uncertainty of the *golden* fit. This procedure gives systematic uncertainties of 1.5 MeV/c^2 to the B^- and B^0 masses and 2.8 MeV/c^2 to the B_s^0 mass.

7.2 Fitting Procedure

A systematic uncertainty due to the fitting procedure is obtained by varying the histogram binning. Additionally, comparisons are made with an unbinned likelihood fit with the likelihood function consisting of a Gaussian signal and linear background. The width of the Gaussian was both fixed for each event and also was taken as the uncertainty obtained by propagating the errors of the covariance matrix (this was also scaled by different amounts). A toy Monte Carlo producing a Gaussian signal and linear background was used to study the ability of a binned fit and unbinned fit to predict the generated masses. As expected, there was very little difference and so I choose to quote the binned fit as the central mass value. Table 7.3 show some of the variation of the fitted values upon changing the fitting procedure. Estimating a systematic uncertainty by taking half of the mass spread in Table 7.3, uncertainties of 0.4, 0.9, and 1.2 MeV/c^2 are assigned to the respective B masses.

7.3 Constrained Fits

The choice of adding a r-ϕ pointing constraint to the constrained fit procedure improves the mass resolution; however, it is not known as to whether a potential mass bias could be introduced. Differences between a vertex constrained fit and a vertex plus pointing constraint have been studied for B^-, B^0, and B_s^0 candidates. Figure 7.1 shows the mass difference of B meson candidates with mass calculated using a vertex constraint alone and using a vertex plus pointing constraint. The mean of all three cases is less than 0.2 MeV/c^2 which is taken as the systematic uncertainty.

7.4 Pt Scale

As described, studies done for the CDF W mass analysis obtain a transverse momentum scale factor of 0.076% $\pm$ 0.071% after adding an additional 31% $\pm$ 10% of material used in the calculation of energy loss and multiple scattering. The uncertainty in the scale factor includes effects from the variation of the J/ψ mass

$c\tau > 0$			$c\tau > 100\mu m$			DW	P_T(X)	$P_T(B)$
Num	Mass	*diff*	Num	Mass	*diff*		(GeV/c)	
$B^- \to J/\psi\ K^-$								
224	5278.3 ± 1.8	-1.3	188	5277.3 ± 1.7	-2.3	–	1.8	0
199	5279.3 ± 1.8	-0.3	174	5277.8 ± 1.7	-1.8	–	1.8	6
170	5280.0 ± 1.7	0.4	151	5279.5 ± 1.7	-0.1	–	1.8	8
190	5279.6 ± 1.7	0.0	165	5278.4 ± 1.6	-1.2	–	2.0	0
174	5280.2 ± 1.8	0.6	157	5278.8 ± 1.7	-0.8	–	2.0	6
152	5279.6 ± 1.7	0.0	140	5279.6 ± 1.7	–	–	2.0	8
$B^0 \to J/\psi\ K^*$								
105	5283.4 ± 3.9	3.5	106	5281.5 ± 2.0	1.6	80	2.0	0
114	5284.9 ± 4.2	5.0	99	5281.2 ± 1.9	1.3	80	2.0	6
95	5281.0 ± 2.1	1.1	95	5281.2 ± 1.7	1.3	80	2.0	8
91	5281.2 ± 2.4	1.3	85	5281.7 ± 2.4	1.8	80	2.5	0
95	5280.6 ± 2.4	0.7	84	5280.7 ± 2.4	0.8	80	2.5	6
90	5279.6 ± 2.1	-0.3	79	5280.5 ± 2.3	0.6	80	2.5	8
85	5280.5 ± 2.5	0.6	72	5282.4 ± 2.2	2.5	80	3.0	0
87	5280.3 ± 2.5	0.4	73	5282.2 ± 2.2	2.3	80	3.0	6
87	5280.0 ± 2.1	0.1	73	5282.1 ± 2.1	2.2	80	3.0	8
102	5280.0 ± 3.6	0.1	95	5279.6 ± 2.2	-0.3	50	2.0	0
96	5279.4 ± 3.3	-0.5	86	5278.6 ± 2.0	-1.3	50	2.0	6
84	5278.0 ± 2.4	-1.9	81	5279.0 ± 2.0	-0.9	50	2.0	8
69	5278.4 ± 2.9	-1.5	69	5279.0 ± 2.9	-0.9	50	2.5	0
73	5277.7 ± 2.7	-2.2	70	5277.7 ± 2.7	-2.2	50	2.5	6
71	5277.0 ± 2.5	-2.9	66	5277.6 ± 2.6	-2.3	50	2.5	8
66	5277.7 ± 2.8	-2.2	54	5279.6 ± 2.7	-0.3	50	3.0	0
68	5277.8 ± 2.7	-2.1	56	5279.5 ± 2.7	-0.4	50	3.0	6
68	5277.8 ± 2.3	-2.1	57	5279.9 ± 2.5	–	50	3.0	8

Table 7.1: Fitted B^- and B^0 mesons masses reconstructed using different selection criteria. Masses are in MeV/$c^2$and DW refers to the daughter window or |M($K\pi$)-M(K^*)|.

$c\tau > 0$			$c\tau > 100\mu m$			DW	P_T(X)	$P_T(B)$
Num	Mass	*diff*	Num	Mass	*diff*		(GeV/c)	
$B_s^0 \to J/\psi\ \phi$								
40	5369.2 ± 3.6	1.5	18	5366.7 ± 3.6	-1.0	12	1.6	0
40	5368.8 ± 3.1	1.1	22	5366.6 ± 2.5	-1.1	12	1.6	6
29	5365.1 ± 3.3	-2.6	18	5365.6 ± 2.8	-2.1	12	1.6	8
43	5368.3 ± 3.3	0.6	22	5364.6 ± 4.1	-3.1	12	1.8	0
39	5367.9 ± 2.9	0.2	23	5365.2 ± 3.0	-2.5	12	1.8	6
33	5365.6 ± 3.0	-2.1	20	5365.6 ± 2.7	-2.1	12	1.8	8
33	5368.2 ± 2.7	0.5	17	5365.0 ± 3.3	-2.7	12	2.0	0
33	5368.2 ± 2.5	0.5	18	5366.1 ± 2.7	-1.6	12	2.0	6
27	5365.0 ± 2.5	-2.7	18	5365.3 ± 2.6	-2.4	12	2.0	8
38	5368.1 ± 3.2	0.4	19	5365.6 ± 3.5	-2.1	10	1.6	0
38	5367.9 ± 2.7	0.2	21	5366.0 ± 2.6	-1.7	10	1.6	6
26	5364.2 ± 2.5	-3.5	18	5365.0 ± 2.6	-2.7	10	1.6	8
40	5367.9 ± 3.1	0.2	21	5364.0 ± 3.7	-3.7	10	1.8	0
38	5367.2 ± 2.6	-0.5	22	5364.4 ± 3.1	-3.3	10	1.8	6
29	5364.5 ± 2.6	-3.2	19	5364.9 ± 2.5	-2.8	10	1.8	8
33	5367.3 ± 2.6	-0.4	17	5364.2 ± 3.2	-3.5	10	2.0	0
33	5367.7 ± 2.4	–	17	5365.4 ± 2.7	-2.3	10	2.0	6
27	5364.5 ± 2.4	-3.2	17	5364.5 ± 2.6	-3.2	10	2.0	8
39	5369.0 ± 3.0	1.3	19	5367.2 ± 2.9	-0.5	8	1.6	0
38	5368.3 ± 2.8	0.6	21	5366.7 ± 2.4	-1.0	8	1.6	6
26	5364.9 ± 2.5	-2.8	18	5365.6 ± 2.4	-2.1	8	1.6	8
39	5368.9 ± 3.0	1.2	20	5366.4 ± 3.0	-1.3	8	1.8	0
37	5367.4 ± 2.7	-0.3	22	5365.1 ± 3.1	-2.6	8	1.8	6
28	5365.0 ± 2.6	-2.7	18	5365.6 ± 2.5	-2.1	8	1.8	8
31	5368.6 ± 2.6	0.9	15	5366.5 ± 2.6	-1.2	8	2.0	0
32	5368.4 ± 2.5	0.7	17	5366.3 ± 2.6	-1.4	8	2.0	6
25	5365.1 ± 2.5	-2.6	17	5365.4 ± 2.6	-2.3	8	2.0	8

Table 7.2: Fitted B_s^0 mesons masses reconstructed using different selection criteria. Masses are in MeV/$c^2$and DW refers to the daughter window or |M(KK)-M(ϕ)|.

Fitting Procedure			B^-	B^0	B_s^0
Binned Fits					
Bin Size MeV/c^2	Initial Bin MeV/c^2	Gaussian Width MeV/c^2	MeV/c^2	MeV/c^2	MeV/c^2
5	5000	floating	5279.6	5279.9	5367.7
5	5001	floating	5279.3	5279.9	5367.6
5	5002	floating	5279.7	5279.8	5368.0
5	5003	floating	5279.4	5279.9	5367.9
5	5004	floating	5279.7	5279.8	5367.7
10	5000	floating	5279.0	5280.3	5368.4
15	5000	floating	5279.8	5279.3	5367.5
10	5000	15 14 11 fixed	5279.1	5280.3	5368.5
10	5000	18 17 14 fixed	5279.0	5280.2	5368.5
10	5000	12 11 8 fixed	5279.2	5280.8	5368.2
Unbinned Fits					
Width fixed at 15 14 11 MeV/c^2			5279.6	5279.8	5367.9
Width fixed at 18 17 14 MeV/c^2			5279.6	5279.6	5368.1
Width fixed at 12 11 8 MeV/c^2			5279.6	–	5367.2
Width from errors			5279.6	5280.1	5369.1
Width from errors$\times$1.3			5279.6	5280.8	5368.9
Width from errors$\times$1.5			5279.7	5281.0	5368.4
Width from errors/1.5			5279.2	–	5369.5

Table 7.3: Fitted B^-, B^0, and B_s^0 mesons masses using different binned and unbinned fitting procedures. No entry is made if the fit did not properly converge.

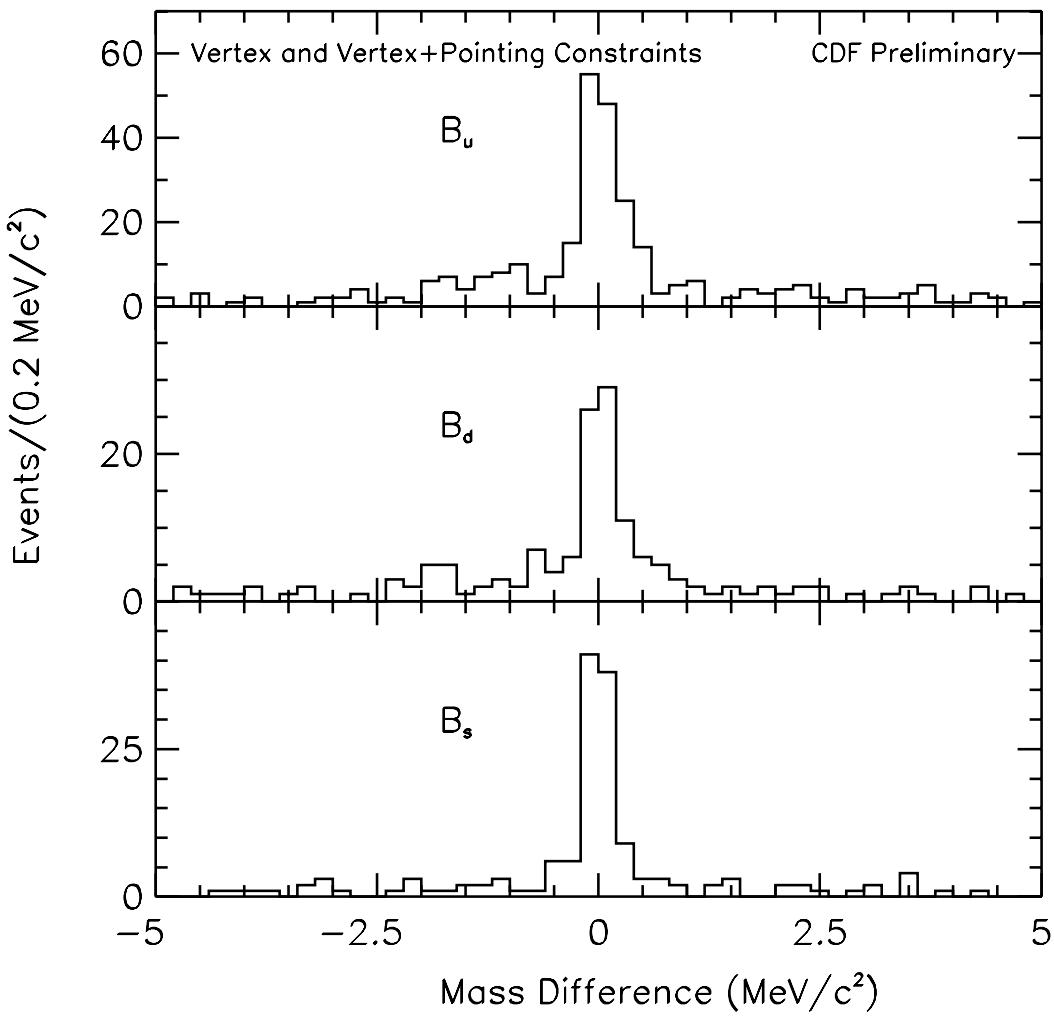

Figure 7.1: Distribution of the difference in mass when using a vertex constraint alone and when using a vertex and r-ϕ pointing constraint. The mean of each histogram is less than 0.2 MeV/c^2. The events are B^-, B^0, and B_s^0 candidates which includes the signal region and some of the sideband region.

versus the run number, J/ψ mass fitting, the presence of radiative tails, scaling to P_Ts relevant for W decays, and geometric and kinematic dependencies of the J/ψ mass.

To study how the uncertainty in the transverse momentum scale factor affects reconstructed B mesons, event-by-event mass differences are calculated for B meson candidates (signal plus sideband) when the scale factors are varied. Compared to the default value of 14.127 KG, Fig. 7.2 shows the distribution of mass differences when magnetic fields of 14.116 and 14.138 are used. The uncertainties for B^-, B^0, and B_s^0 are 1.3, 1.2, and 1.1 MeV/c^2 respectively. In Fig. 7.3, the mass differences are shown when the material is scaled by 1.0 and 1.5 compared with the default value of 1.31. The uncertainties are taken to be the mean of each plot. The uncertainties for B^-, B^0, and B_s^0 are 0.4, 0.6, and 0.6 MeV/c^2 respectively.

7.5 Covariance Matrix

Studies of the CTC covariance matrix [63] indicate that the uncertainties returned by the track fit are underestimated. The offline analysis used in this dissertation scales all the elements of the covariance matrix by a factor of 2.0. This scale factor gives better agreement between with the data in terms of mass uncertainties, constrained fit CL(χ^2) distributions, and CTC-SVX matching χ^2s. Since the constrained fitting routine, CTVMFT, minimizes a χ^2 using the elements of the covariance matrix, the uncertainty in the scale factor could potentially result in systematic mass shifts. It is also known that even with the 2.0 scale factor, more signal events in both the J/ψ and B samples can be found at low CL(χ^2) than expected. This could indicate that the covariance matrix is still not correct. Figure 7.4 shows the mass difference for B meson candidates when scale factors of 1.5 and 2.5 are used instead of 2.0. There is no indication of a systematic mass shift although the mass measurement of an individual candidate could shift 1 or 2 MeV/c^2. The uncertainties are taken from the means of these distributions.

Another potential concern is whether a systematic mass shift could result if the individual elements of the covariance matrix are scaled differently. To exaggerate this effect, I consider the mass shifts if the curvature and ϕ_0 elements are scaled by 2.5 while cotangent and z_0 are scaled by 1.5 (and visa versa). Figure 7.5 shows the resulting mass difference. Notice that any systematic shift is small; however, individual events can shift of the order of 10 MeV/c^2. Studies [63] that have been done suggest that the ratio of scale factors is less than 2.5:1.5 and so Fig. 7.5 presents a larger effect than expected in the data. Based on the observed mass shifts, a 1 MeV/c^2 systematic is assigned due to this uncertainty.

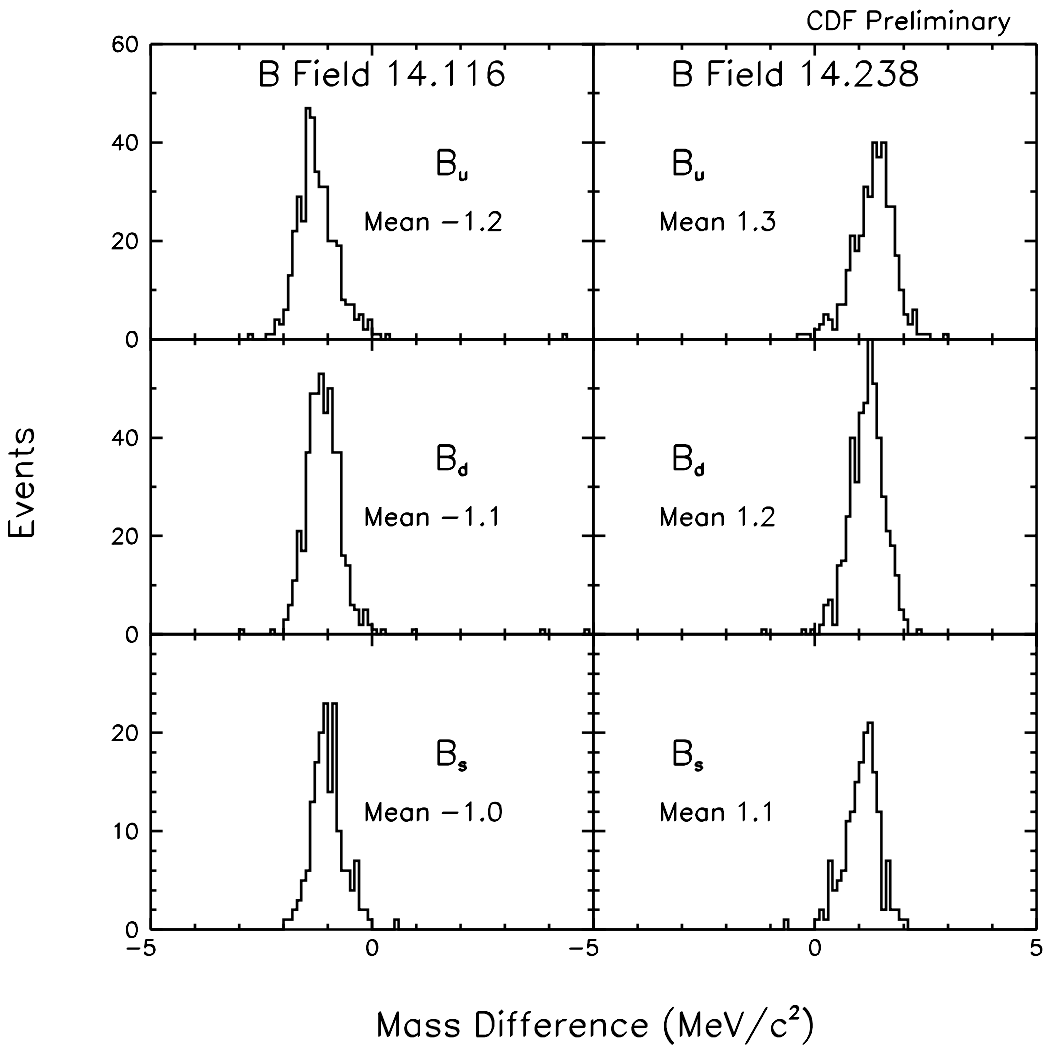

Figure 7.2: Distribution of the difference in mass when using the indicated magnetic field value and using the default value of 14.127 KG. The events are B^-, B^0, and B_s^0 candidates which includes the signal region and some of the sideband region.

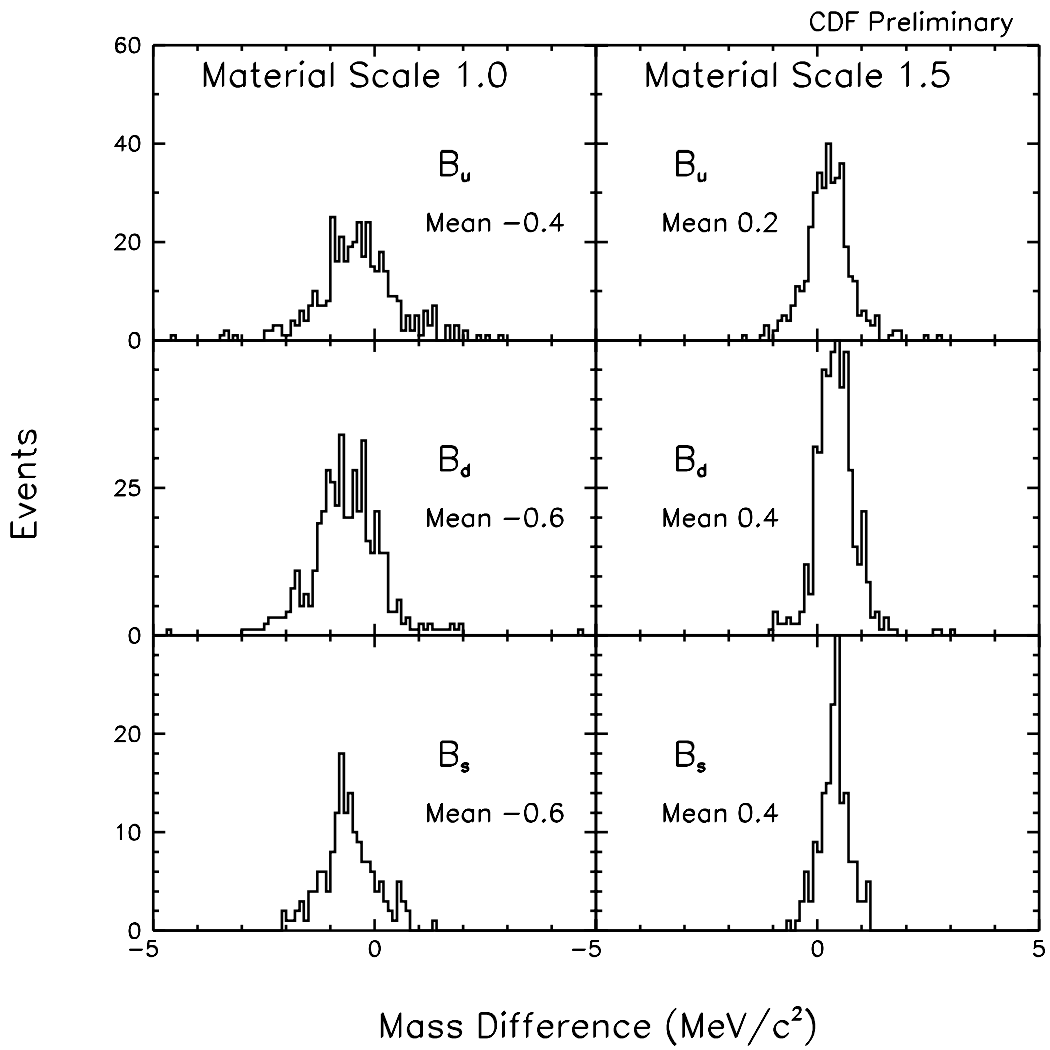

Figure 7.3: Distribution of the difference in mass when using the indicated scale factor on the amount of material used for dE/dx and multiple scattering corrections and using the default value of 1.31. The events are B^-, B^0, and B_s^0 candidates which includes the signal region and some of the sideband region.

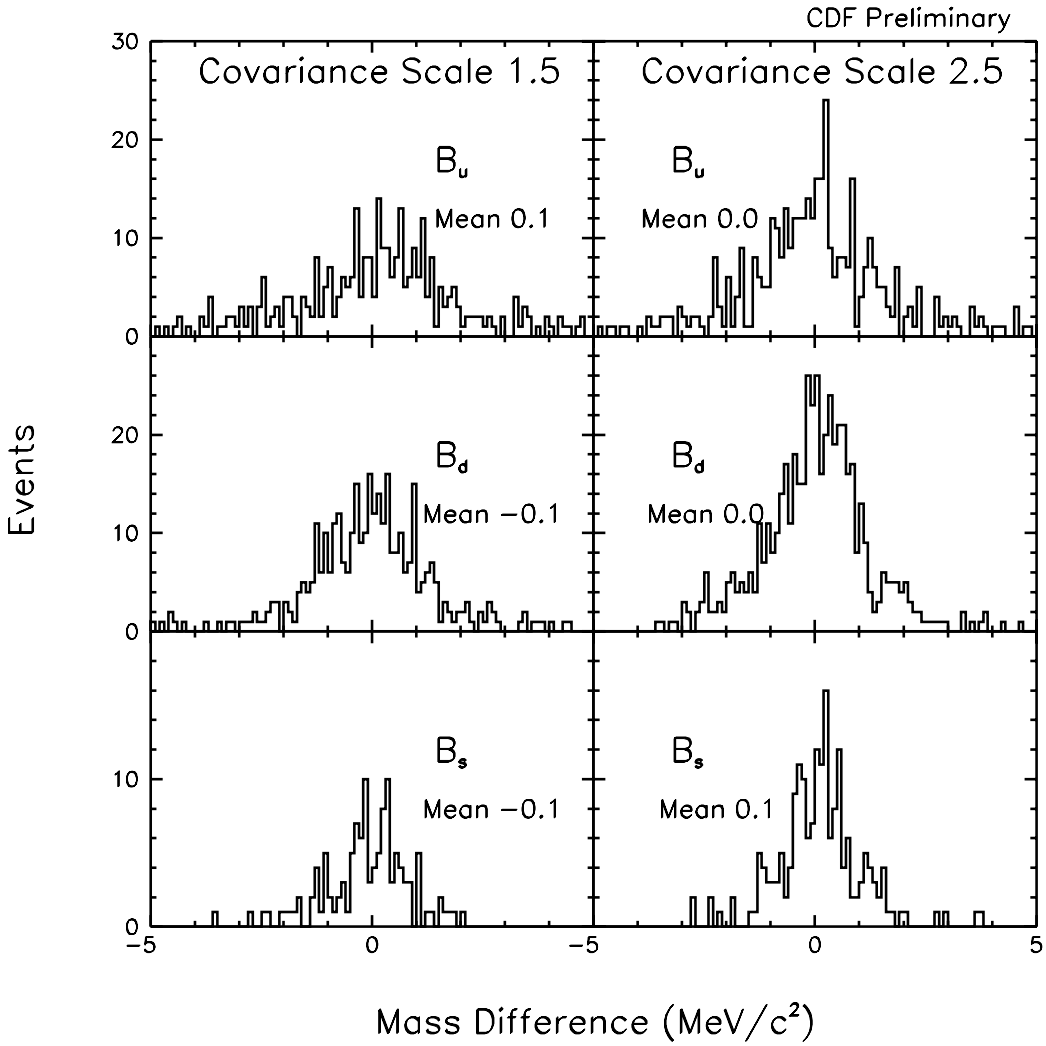

Figure 7.4: Distribution of the difference in mass when using the indicated global scale factors on the elements of the CTC covariance matrix and using the default value of 2.0. The events are B^-, B^0, and B_s^0 candidates which includes the signal region and some of the sideband region.

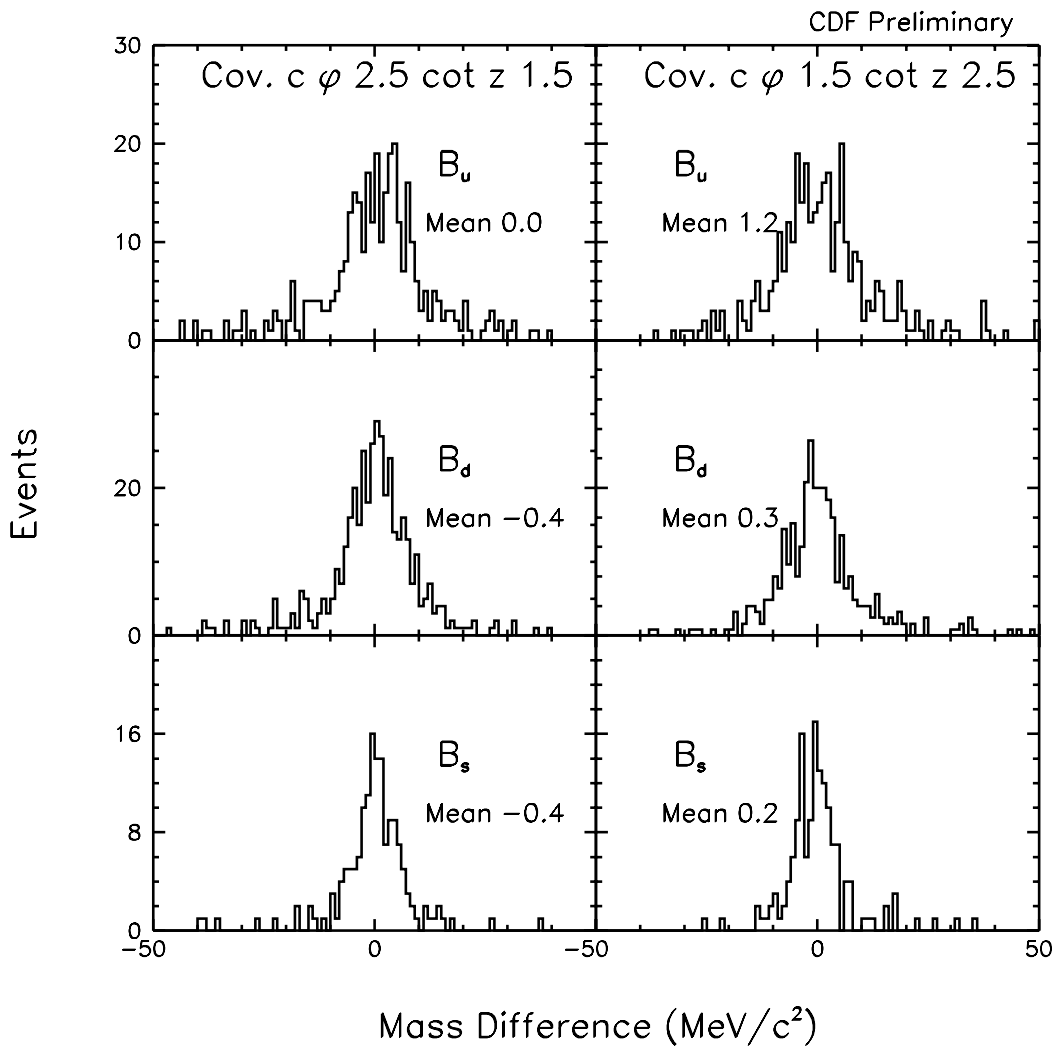

Figure 7.5: Distribution of the difference in mass when using the indicated scale factors on the elements of the CTC covariance matrix and using the default global value of 2.0. The events are B^-, B^0, and B_s^0 candidates which includes the signal region and some of the sideband region.

7.6 False Curvature

Figure 7.6 (top) shows a systematic effect present in the CDF data. The fitted J/ψ mass is plotted for bins of P_T of the negative and positive muon. Each J/ψ contributes twice to plot, which shows a 7 MeV/c^2 spread in the fitted J/ψ mass that depends on the P_T of the negatively charged muon. Studies suggest that this effect is the result of a false curvature and is caused by CTC tracking misalignment. A false curvature correction of -8×10^{-7} is applied to the curvature parameter for both muons. Figure 7.6 (bottom) shows the fitted J/ψ mass after this correction having a narrower spread as a function of the charge and P_T of the muon. Further study of a false curvature correction is needed and preferably new CTC alignment constants should be used in a new reprocessing of the data to remove this effect. To estimate the potential systematic effect in determining the masses of B mesons, the same correction factor has been applied to B candidates. Figure 7.7 shows the difference in the reconstructed B masses after applying this correction. The effect is largest for $B^- \to J/\psi\ K^-$ where only one charged particle (excluding $J/\psi \to \mu^+\ \mu^-$) is in the final state. The systematic mass shift is to a larger mass for the positively charged B meson and to a lower mass for the negatively charged B meson. For B^0 and B_s^0, the hypothesis is that any systematic effect is reduced since the K^* and ϕ decay into a pair of oppositely charged tracks.

Figure 7.8 shows the $J/\psi\ K^-$ mass distributions separately for positive and negative kaon candidates. The lower reconstructed mass for the positively charged B meson relative to the negatively charged B meson is what is expected based on the above discussion on a curvature correction. A systematic mass shift arises if there is an asymmetry in the reconstructed numbers of positive and negative B. This is indeed observed with the fitted mass at 5279.6 MeV/c^2 for the combined sample, being 0.4 MeV/c^2 from the average mass of the two charges of 5280.0 MeV/c^2. For the systematic uncertainty, I allow for an asymmetry of 90 positive and 50 negative events consistent within 1 σ of the number returned by the fit. Weighting the positive and negative masses in this way gives an average of 5279.3 MeV/c^2 which is 0.7 MeV/c^2 from the mass with no weighting. For B^-, I assign 0.7 MeV/c^2 as the systematic and zero uncertainty for B^0 and B_s^0 candidates since the decay of the daughters is charge symmetric.

7.7 $\Delta\cot\theta$

There is a another systematic dependence of the J/ψ mass as a function of the difference in cotangents between the two muons as seen in Fig. 7.9 (top). The cause of this effect is not known. To estimate the possible effect on B masses, a phenomenological correction derived from Fig. 7.9 is developed. The effect of this

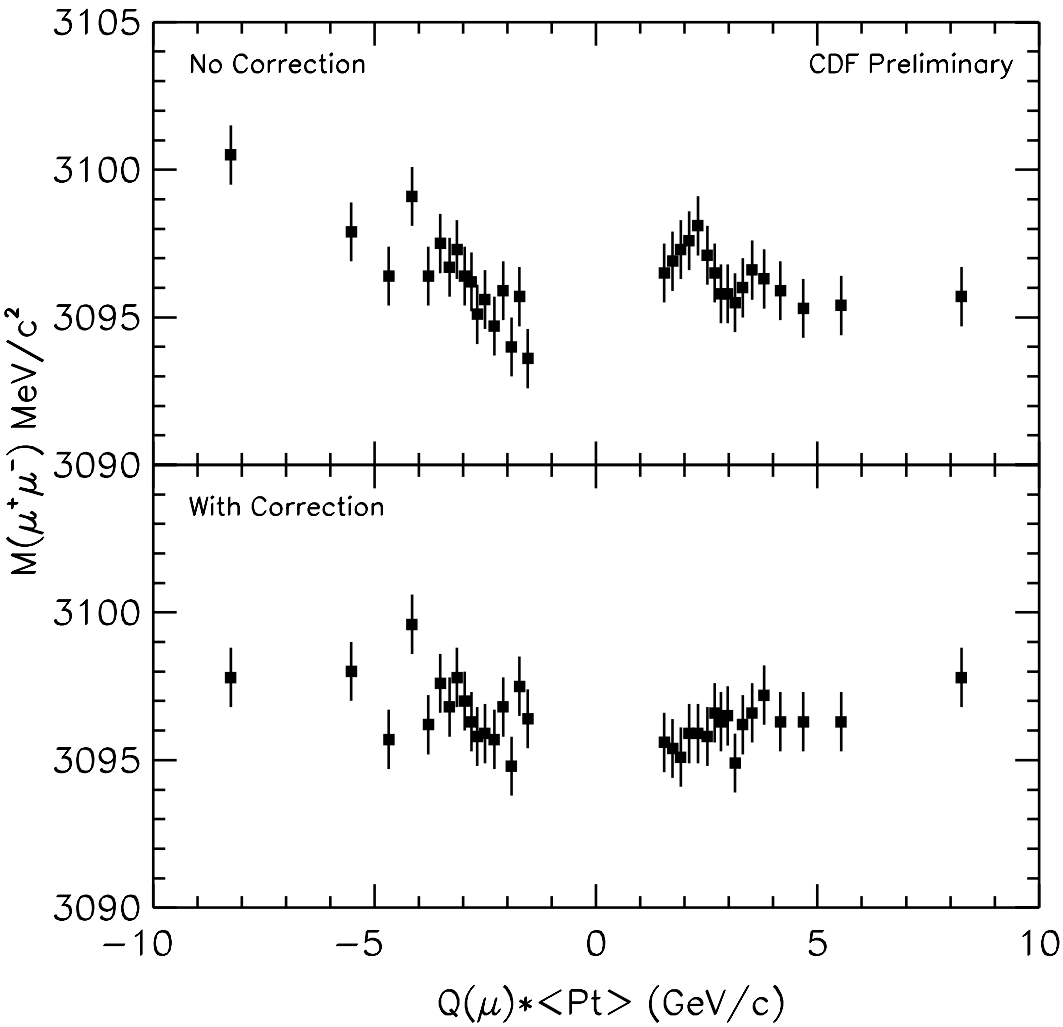

Figure 7.6: Fitted J/ψ mass for bins of P_T in which the negative and positive muon fall (each J/ψ contributes twice to the plot). In the top plot, a large spread is observed coming from the 6.15 data. In the bottom plot, the spread is reduced when corrections are applied to the curvature as discussed in the text.

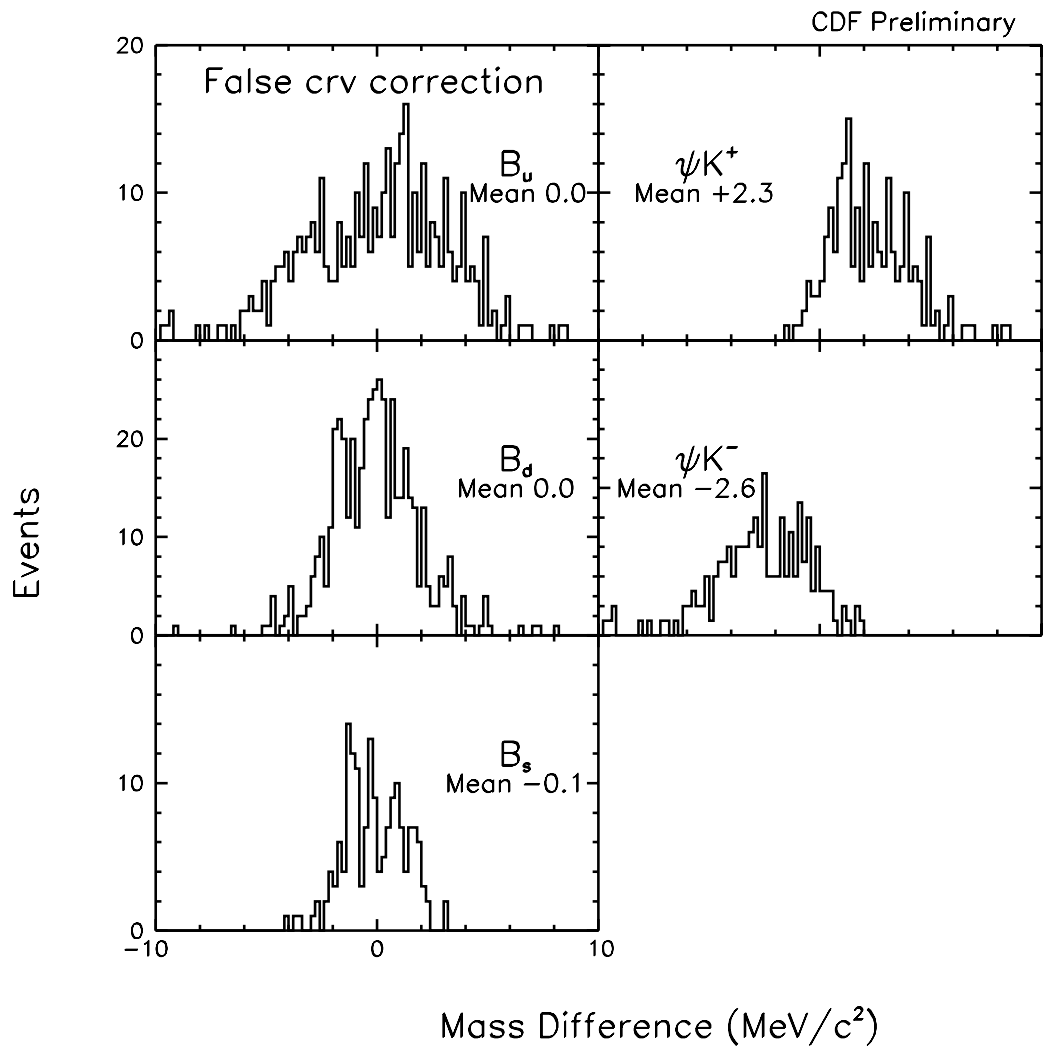

Figure 7.7: Distribution of the difference in mass when using the curvature correction factors discussed in the text and using no correction. The events are B^-, B^0, and B_s^0 candidates which includes the signal region and some of the sideband region. For B^- candidates, a separate distribution is shown for positive and negative kaons.

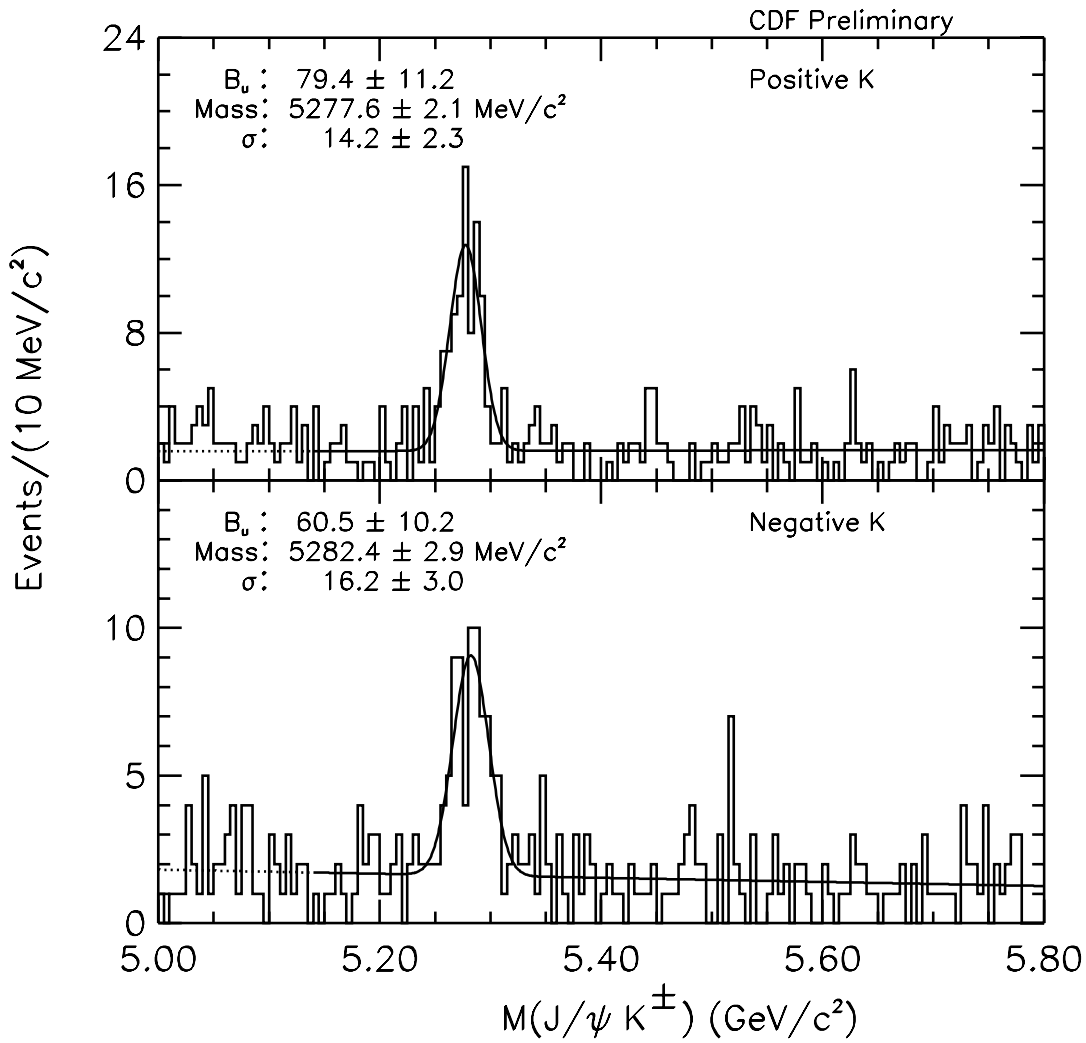

Figure 7.8: Mass distribution of $J/\psi\ K^-$ candidates separated into candidates with a positive and negative kaon.

correction on J/ψ reconstruction is shown in Fig. 7.9 (bottom). The cotangent of both muons is scaled lower by 0.3% and a constant of .0012 was added to the cotangent of the positive muon. In addition, the P_T of both muons is scaled up so that the average J/ψ mass remained approximately constant. This correction can also be applied to the tracks involved in forming B meson candidates and then the mass difference compared with the standard analysis can be plotted as shown in Fig. 7.10. This plot indicates that the $\Delta\cot\theta$ effect affects B meson masses at the level of 1.6 MeV/c^2 or less. Because there are many uncertainties with a correction on cotangent (there are fairly large correlations with curvature, for instance), I consider another approach to estimating the systematic uncertainty.

The effect of this systematic on the reconstructed B masses is estimated by comparing the fitted B masses as a function cotangent of the opening angles for the decay. For each of the B mesons, Figs. 7.11, 7.12, 7.13 show the B mass distributions separated into two regions of $\Delta\cot\theta$ with equal statistics. The difference in cotangent is taken between the J/ψ and daughter meson. For B^0 and B_s^0, Figs. 7.14, 7.15 show the corresponding mass distributions where $\Delta\cot\theta$ is defined as the opening between the kaon and pion or two kaons respectively. The results of the mass fits are shown in Table 7.4 along with the estimated contribution to the systematic uncertainty. The systematic uncertainty is taken as half the difference between masses for the separate regions of $\Delta\cot\theta$ assuming that the correct value lies between the two extremes.

The overall systematic is taken to be the larger systematic either from what happens to B masses after applying a $\cot\theta$ correction or from the study based on dividing the signals into separate regions of $\Delta\cot\theta$.

B Meson	$\Delta\cot\theta < x$ J/ψX	$\Delta\cot\theta > x$ J/ψX	x	syst	$\Delta\cot < x$ $K/\pi K$	$\Delta\cot > x$ $K/\pi K$	x	syst
B^-	5278.2	5280.2	.35	1.0	–	–	–	–
B^0	5280.0	5284.4	.30	0.2	5277.4	5282.9	.12	2.8
B_s^0	5369.2	5367.4	.40	0.9	5365.0	5371.3	.007	3.2

Table 7.4: Results of fitting the masses of reconstructed B mesons separated into regions of $\Delta\cot\theta$.

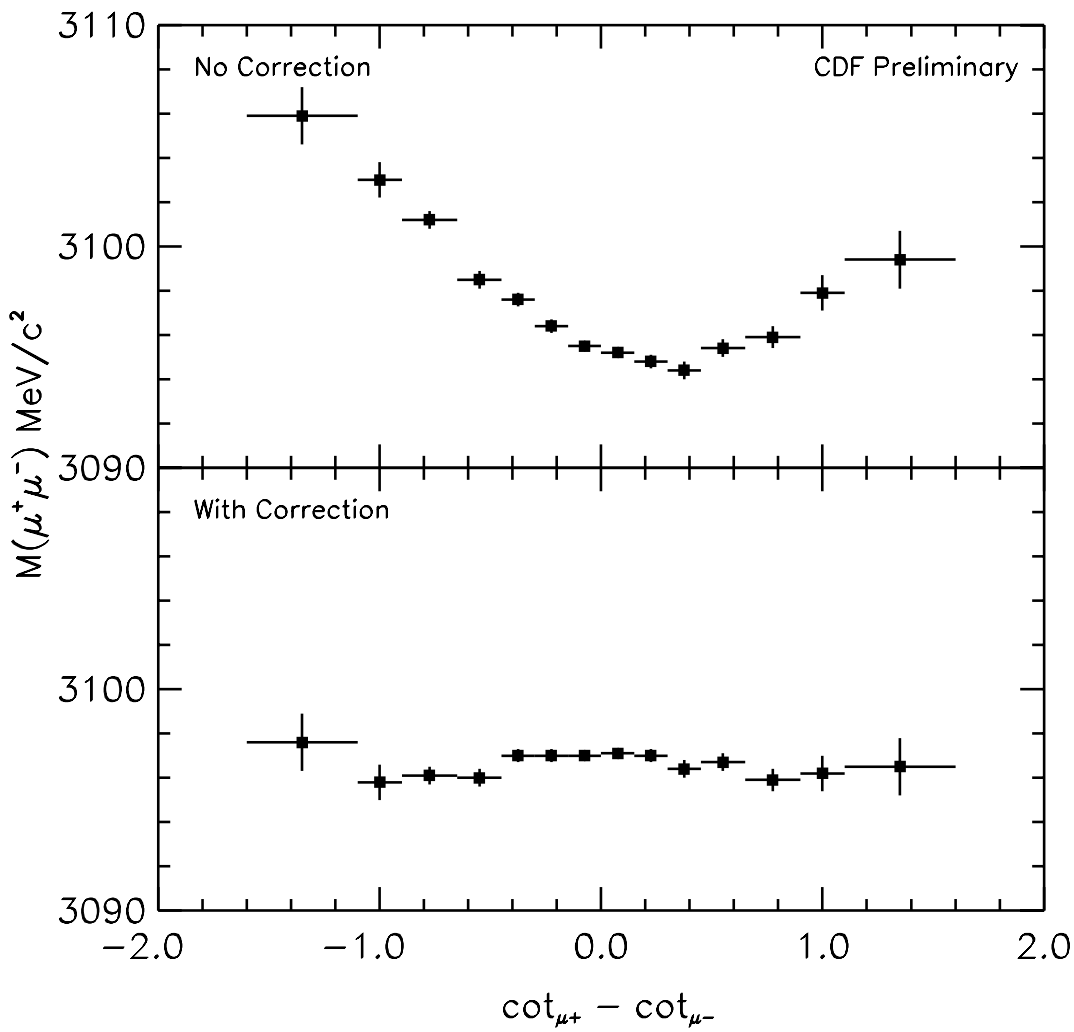

Figure 7.9: Fitted J/ψ masses in bins of $\Delta\cot\theta$ between the two muons. In the top plot, a large spread is observed. In the bottom plot, the spread is reduced when corrections are applied to the cotangent as discussed in the text.

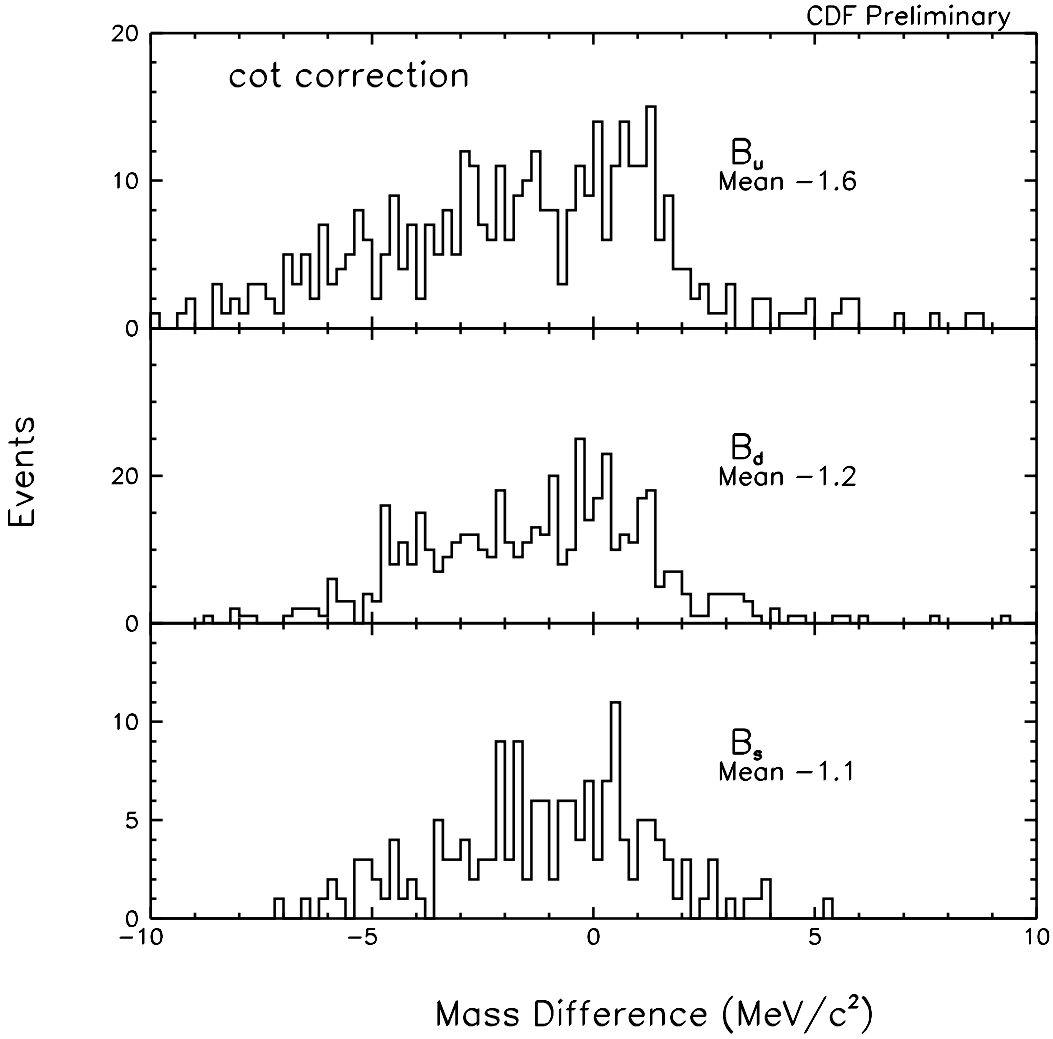

Figure 7.10: Distribution of the difference in mass when using the cotangent correction factors discussed in the text and using no correction. The events are B^-, B^0, and B_s^0 candidates which includes the signal region and some of the sideband region.

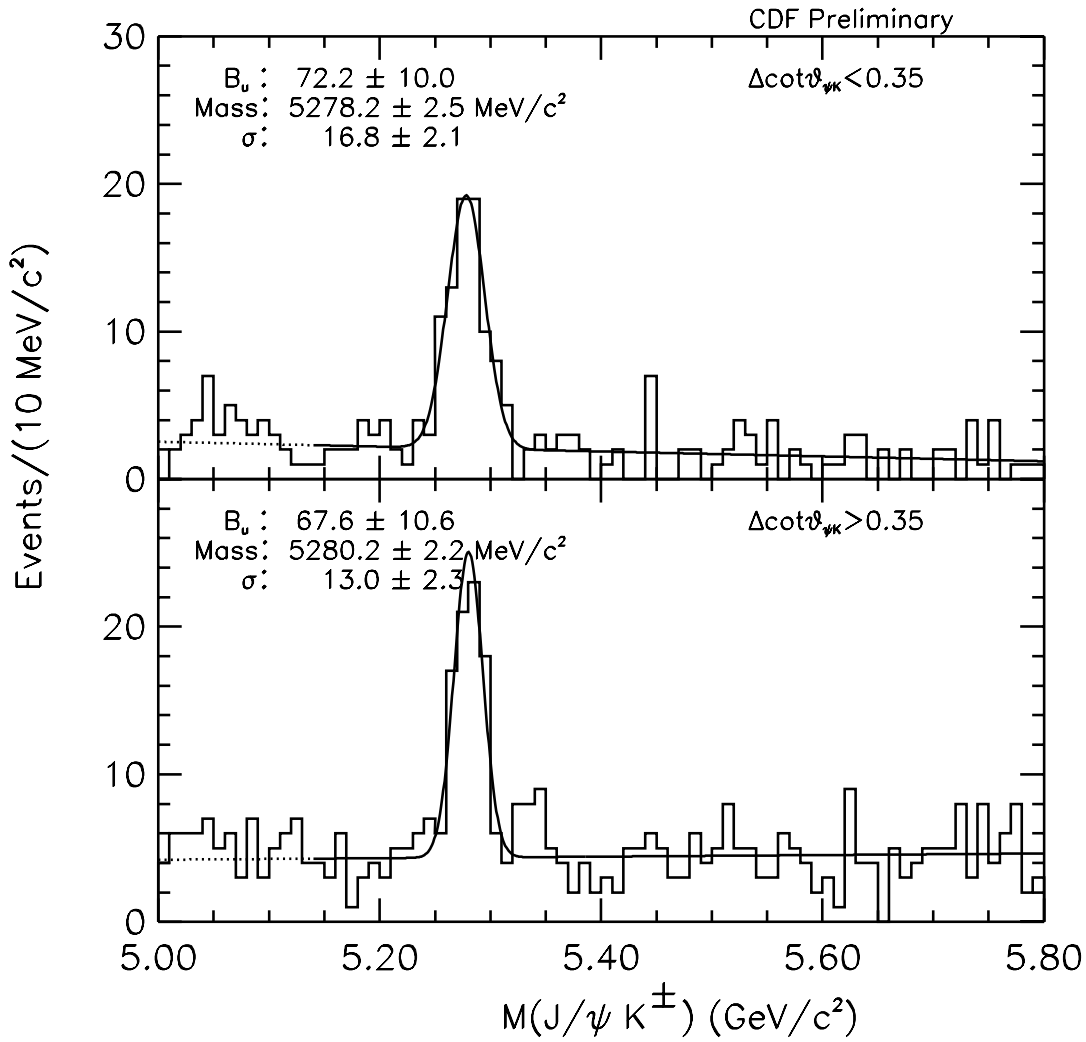

Figure 7.11: Reconstructed B^- mesons separated into two regions of $\Delta\cot\theta$ between the J/ψ and K.

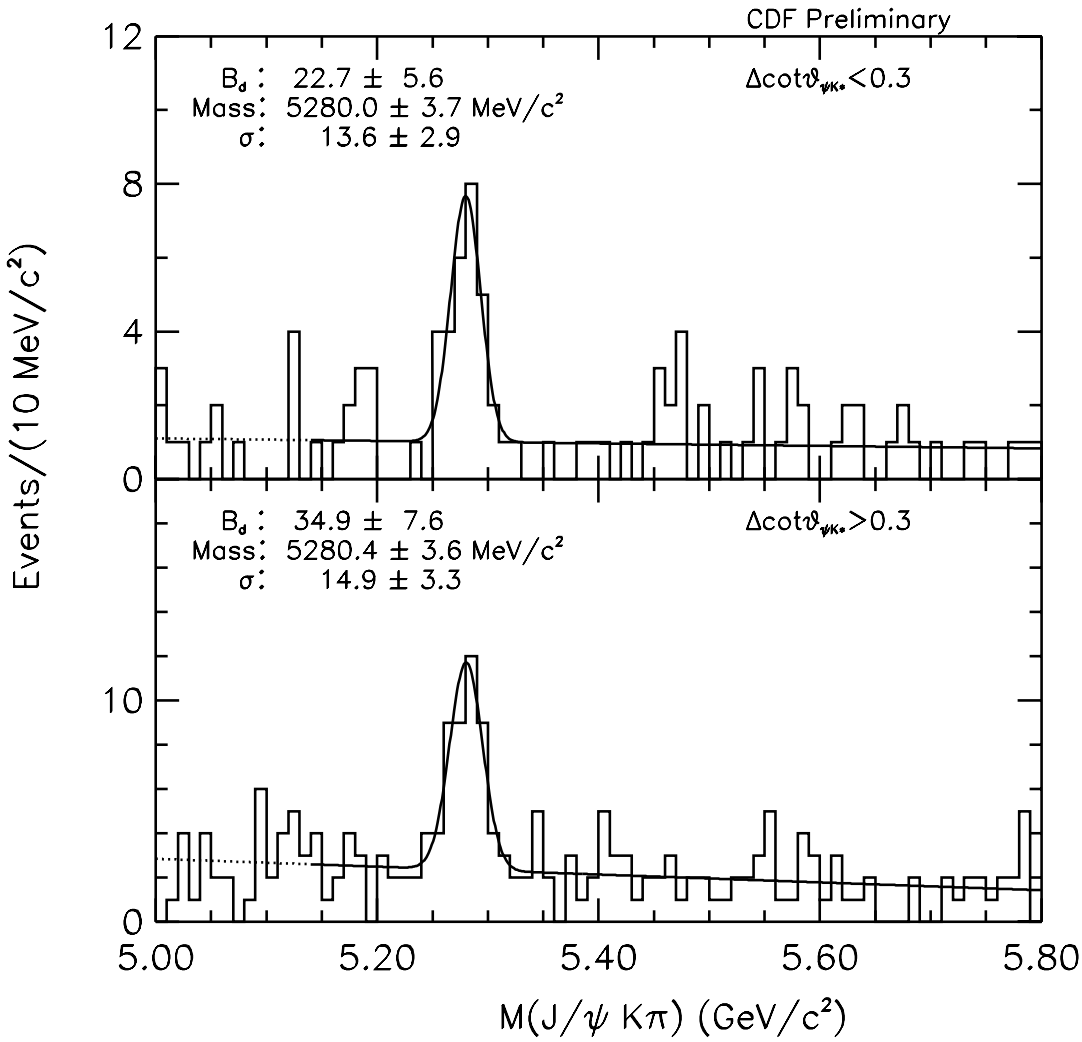

Figure 7.12: Reconstructed B^0 mesons separated into two regions of $\Delta\cot\theta$ between the J/ψ and K^*.

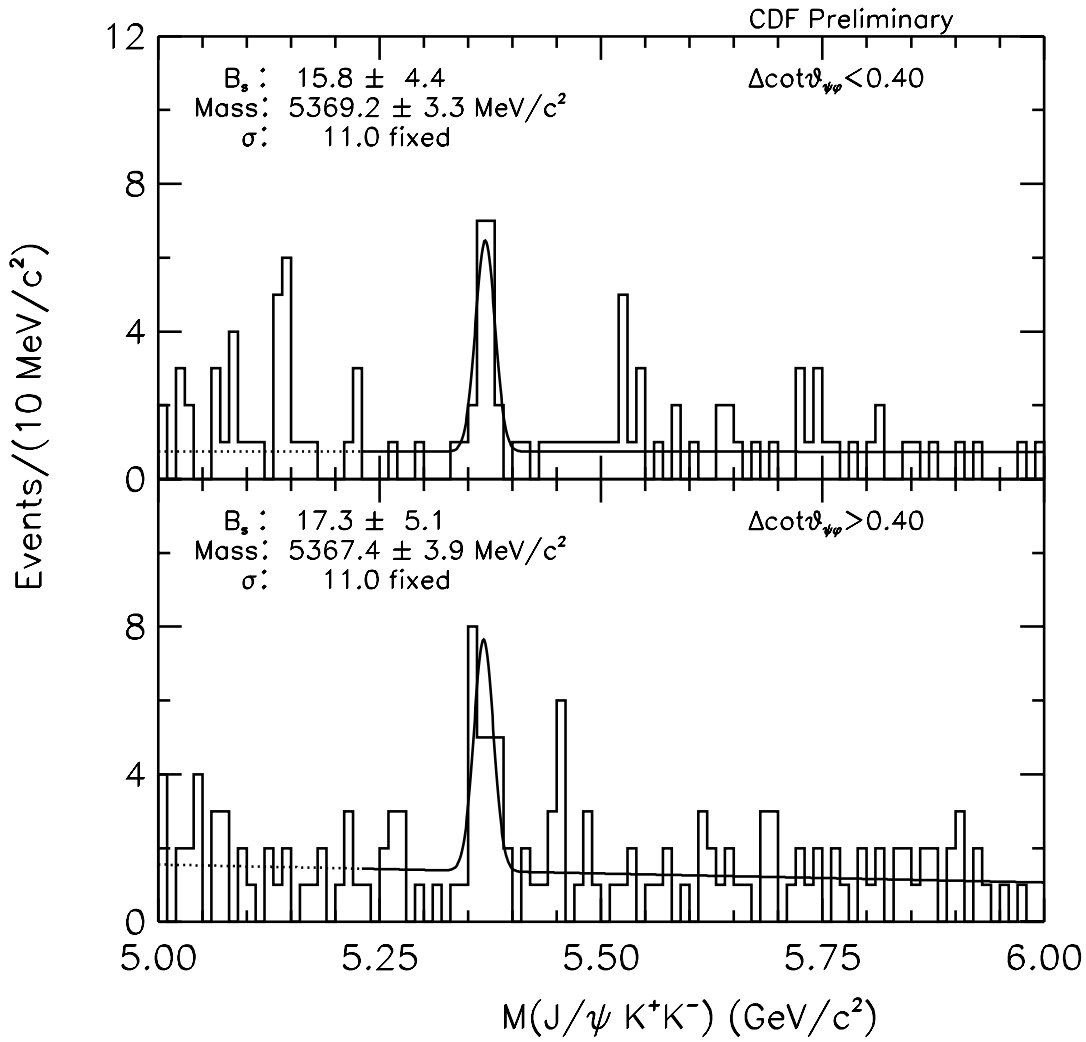

Figure 7.13: Reconstructed B_s^0 mesons separated into two regions of $\Delta\cot\theta$ between the J/ψ and ϕ.

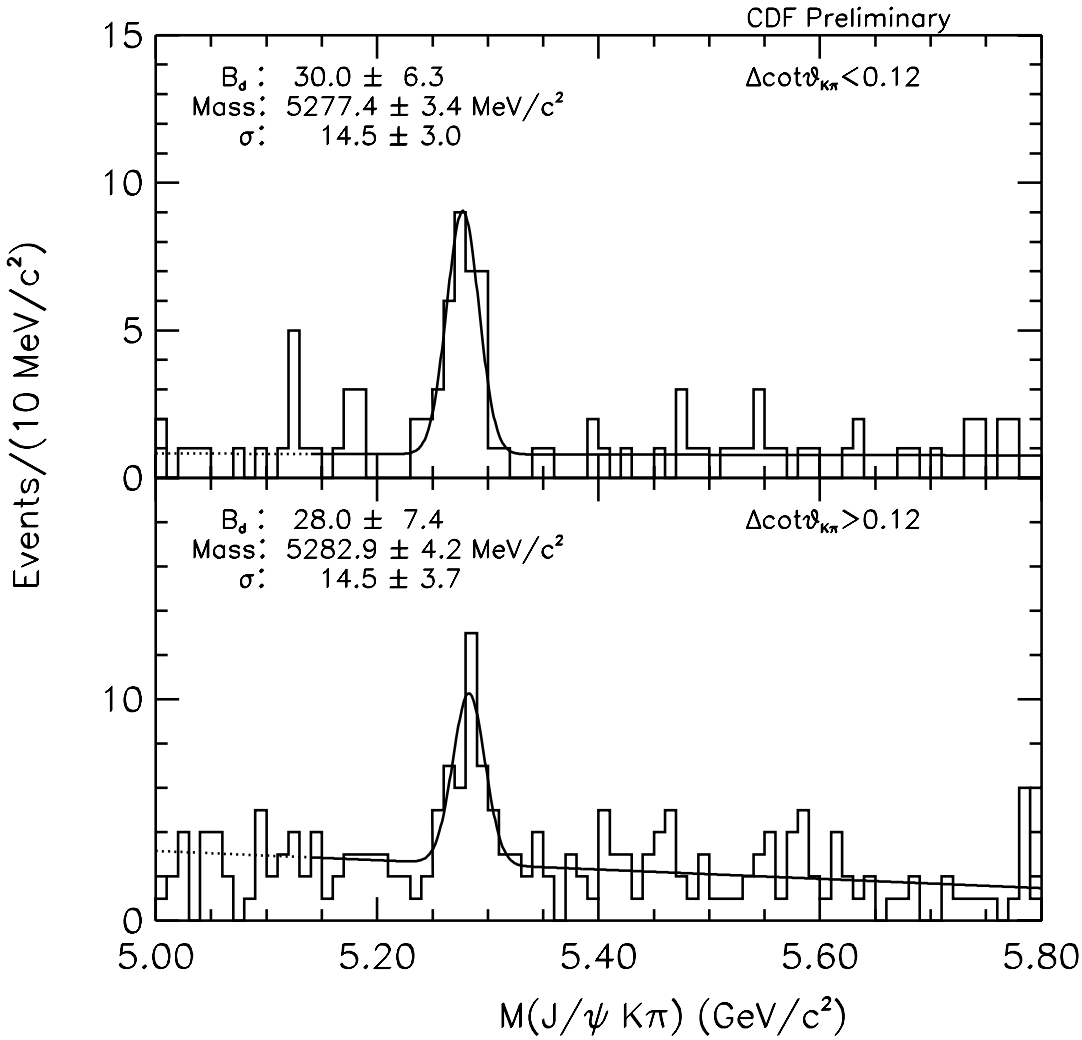

Figure 7.14: Reconstructed B^0 mesons separated into two regions of $\Delta\cot\theta$ between the K and π from the K^*.

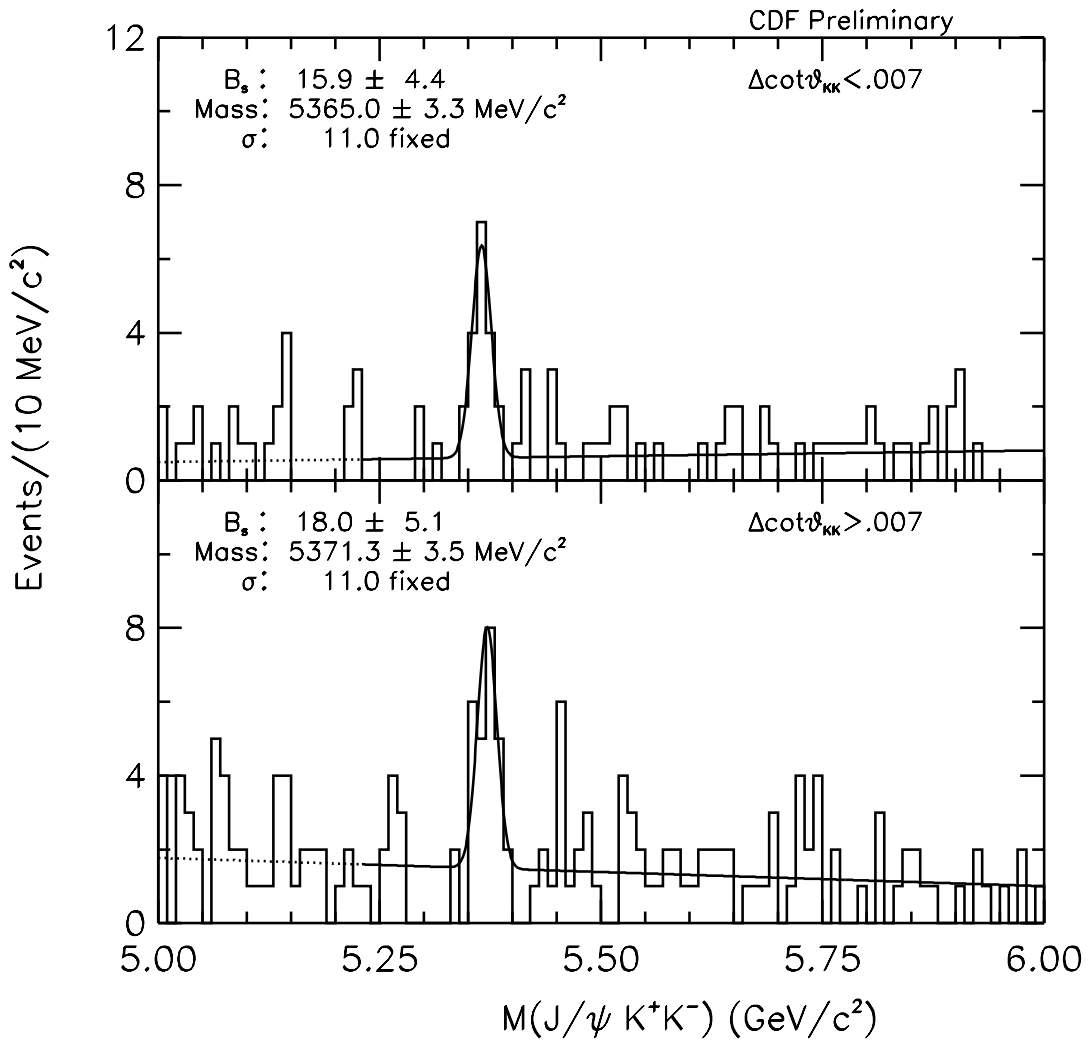

Figure 7.15: Reconstructed B_s^0 mesons separated into two regions of $\Delta\cot\theta$ between the two Ks from the ϕ.

7.8 Summary and Conclusions

Table 7.5 summarizes the systematic uncertainties in the mass determination of B mesons. The masses of the B^-, B^0, and B_s^0 mesons have been measured and

Systematic Effect	B^-	B^0	B_s^0
P_T Scale	1.3	1.2	1.1
Material Scale	0.4	0.6	0.6
Mass Fitting	0.4	0.9	1.2
Selection Criteria	1.5	1.5	2.8
Pointing Constraint	0.2	0.2	0.2
Covariance Matrix Scale	1.0	1.0	1.0
False Curvature	0.7	0.0	0.
$\Delta\cot\theta$	1.6	2.8	3.3
Total MeV/c^2	2.9	3.7	4.8

Table 7.5: Summary of the contributions to the systematic uncertainties in the B meson measured masses.

statistical and systematic uncertainties have been evaluated:

- $\mathrm{M}(B^-) = 5279.6 \pm 1.7$ (stat) ± 2.9 (syst) MeV/c^2
- $\mathrm{M}(B^0) = 5279.9 \pm 2.5$ (stat) ± 3.7 (syst) MeV/c^2
- $\mathrm{M}(B_s^0) = 5367.7 \pm 2.4$ (stat) ± 4.8 (syst) MeV/c^2

Chapter 8

Conclusions

The $J/\psi \rightarrow \mu^+ \mu^-$ sample of the 1992–1993 CDF data taking run has been used to reconstruct sizable quantities of exclusive B meson decays. The dimuon decay mode is triggerable and is expected to be B enriched. The decay modes $B^- \rightarrow J/\psi\ K^-$, $B^0 \rightarrow J/\psi\ K^*$, and $B_s^0 \rightarrow J/\psi\ \phi$ have been reconstructed. The reconstruction involves imposing a set of selection criteria that takes advantage of the kinematics of the decays and nonzero finite lifetime. The masses of the B mesons are measured by fitting the mass distributions which show significant signal above background after imposing the selection criteria.

The first sizable sample of fully reconstructed B_s^0 mesons has been obtained resulting in a precise mass measurement. The method of measuring the mass of a B meson results in agreement with the world average B^- and B^0 masses. This provides additional confidence that the technique may be applied to the B_s^0 case. Systematic uncertainties in the mass measurement have been evaluated for all three B mesons. These systematic effects include uncertainties associated with corrections of the P_T scale, alternative selection and fitting methods, and effects observable in the large $J/\psi \rightarrow \mu^+ \mu^-$ sample.

The results are given below:

- $M(B^-) = 5279.6 \pm 1.7\ (\text{stat}) \pm 2.9\ (\text{syst})\ \text{MeV}/c^2$
- $M(B^0) = 5279.9 \pm 2.5\ (\text{stat}) \pm 3.7\ (\text{syst})\ \text{MeV}/c^2$
- $M(B_s^0) = 5367.7 \pm 2.4\ (\text{stat}) \pm 4.8\ (\text{syst})\ \text{MeV}/c^2$

Clearly, it has been demonstrated that B physics can be done in a hadron collider environment. A Silicon Vertex detector has operated in such an environment and has contributed to the measurements presented in this dissertation. The large b production cross section at high energy hadron colliders is exploitable for proposed future measurements in B physics. Precise measurements of B meson

masses have been made with overall uncertainty considerably less than that of the theoretical predictions.

Bibliography

[1] H. Fritzsch, M. Gell-Mann, and H. Leutwyler, Phys. Lett. **B47**, 365 (1973).

[2] S. L. Glashow, Nucl. Phys. **22**, 579 (1961); S. Weinberg, Phys. Rev. Lett. **19**, 1264 (1967); A. Salam, *Elementary Particle Theory: Relativistic Groups and Analyticity* (Nobel Symposium No. 8), edited by W. Svartholm (Almqvist and Wiksell, Stockholm), 367 (1968).

[3] P. W. Higgs, Phys. Rev. Lett. **12**, 132 (1964); Phys. Rev. **145**, 1156 (1966); G. 't Hooft, Nucl. Phys. **B33**, 167 (1971); Nucl. Phys. **B35**, 167 (1971).

[4] CDF Collaboration, F. Abe *et al.*, "Evidence for Top Quark Production in $\overline{p}p$ Collisions at $\sqrt{s} = 1.8$ TeV," FERMILAB-PUB-94/097-E, submitted to Phys. Rev. D. (1994).

[5] J. J. Aubert *et al.*, Phys. Rev. Lett. **33**, 1404 (1974).

[6] J.-E. Augustin *et al.*, Phys. Rev. Lett. **33**, 1406 (1974).

[7] N. Cabibbo, Phys. Rev. Lett. **10**, 531 (1963).

[8] S. L. Glashow, J. Iliopoulos, and L. Maiani, Phys. Rev. **D2**, 1285 (1970).

[9] M. Kobayashi and K. Maskawa, Progr. Theor. Phys. **49**, 652 (1973).

[10] L. Wolfenstein, Phys. Rev. Lett. **51**, 1945, (1983).

[11] A. Ali, DESY-92-152 (1992).

[12] J. H. Christenson *et al.*, Phys. Rev. Lett. **13**, 138 (1964).

[13] M. L. Perl *et al.*, Phys. Rev. Lett. **35**, 1489 (1975).

[14] S. W. Herb *et al.*, Phys. Rev. Lett. **39**, 252 (1977).

[15] PLUTO Collaboration, Ch. Berger *et al.*, Phys. Lett **76B**, 243 (1978); C. W. Darden *et al.*, Phys. Lett. **76B**, 246 (1978); **78B**, 364 (1978).

[16] D. Andrews *et al.*, Phys. Rev. Lett. **44**, 219 (1980); G. Finocchiaro *et al.*, Phys. Rev. Lett. **45**, 222 (1980).

[17] S. Behrends *et al.*, Phys. Rev. Lett. **50**, 881 (1983).

[18] CLEO Collaboration, M. S. Alam *et al.*, "Exclusive Hadronic B Decays to Charm and Charmonium Final States," CLNS 94/1270 (1994).

[19] Particle Data Group, K. Hikasa *et al.*, Phys. Rev. D **45** V.6 (1992).

[20] F. Abe *et al.*, "Measurement of the B Meson and b Quark Cross-Sections in $\overline{p}p$ Collisions at $\sqrt{s} = 1.8$ TeV Using the Exclusive Decays $B^- \to J/\psi\ K^-$ and $B^0 \to J/\psi\ K^*$", FERMILAB-CONF-93/200-E (1993).

[21] Particle Data Group, K. Hikasa *et al.*, Phys. Rev. D **45** VII.150 (1992).

[22] P. Nason, S. Dawson, and R. K. Ellis, Nucl. Phys. **B303**, 608 (1988); **B327**, 49 (1989).

[23] A. Martin, R. Roberts, and J. Stirling, RAL-92-021 (1992); DTP/92/16 (1992).

[24] C. Peterson *et al.*, Phys. Rev. D**27**, 105 (1983); J. Chrin, Z. Phys. **C36**, 163 (1983).

[25] Particle Data Group, K. Hikasa *et al.*, Phys. Rev. D **45** III.79 (1992).

[26] C. S. Kim and A. D. Martin, Phys. Lett. **225B**, 186 (1989).

[27] M. Bauer, B. Stech, and M. Wirbel, Z. Phys. **C34**, 103 (1987).

[28] J. Bijnens and F. Hoogeveen, Phys. Lett. **225B**, 434 (1992); A. Deandrea *et al.*, Phys. Lett. **318B**, 549 (1993).

[29] K. Igi and S. Ono, Phys. Rev. D**32**, 232 (1985)

[30] W. Kwong and J. Rosner, Phys. Rev. D**44**, 212 (1991)

[31] R. P. Feynman, Phys. Rev. **56**, 340 (1939); H. Hellmann, *Einfuhrung in den Quantenchemic* (Deuticke Verlag, Leipzig, (1937).

[32] D. Y. Kim and S. N. Sinha, Phys. Rev. D**30**, 1944 (1984). S. Godfrey and N. Isgur, Phys. Rev. D**32**, 189 (1985); A. Martin, in *Heavy Flavors and High Energy Colllisions in the 1-100 TeV Range*, edited by A. Ali and L. Cifarelli, 141, (Plenum, New York, 1989).

[33] A. Duncan, E. Eichten *et al.*, "Masses and Decay Constants of Heavy-Light Mesons Using the Multistate Smearing Technique," FERMILAB-CONF-93/376-T (1993).

[34] UA1 Collaboration, H. C. Albajar *et al.*, Phys. Lett. **B186**, 247 (1987); CDF Collaboration, F. Abe *et al.*, Phys. Rev. Lett. **67**, 3351 (1991).

[35] DELPHI Collaboration, P. Abreu *et al.*, Phys. Lett.**B289**, 199 (1992); ALEPH Collaboration, D. Buskulic *et al.*, Phys. Lett. **B294**, 145 (1992); OPAL Collaboration, P. D. Acton *et al.*, Phys. Lett.**B295**, 357 (1992).

[36] CUSB Collaboration, J. Lee-Franzini *et al.*, Phys. Rev. Lett. **65**, 2947 (1990).

[37] DELPHI Collaboration, P. Abreu *et al.*, "Production Rate and Decay Lifetime Measurements of B_s^0 at LEP using D_s and ϕ Mesons," CERN-PPE-93-176 (1993), submitted to Z. Phys. **C** (1993); OPAL Collaboration, P. D. Acton *et al.*, Phys. Lett.**B295**, 357 (1992).

[38] ALEPH Collaboration, D. Buskulic *et al.*, Phys. Lett. **B311**, 425 (1993); ERRATUM **B316**, 631 (1993).

[39] CDF Collaboration, F. Abe *et al.*, Phys. Rev. Lett. **71**, 1685 (1993).

[40] In the CDF coordinate system, ϕ is the azimuthal angle, θ is the polar angle, and r is the radius from the proton beam axis (z-axis).

[41] C. Newman-Holmes, E. E. Schmidt, and R. Yamada, Nucl. Instrum. Methods Phys. Res., Sect. A **274**, 443 (1989).

[42] D. Amidei *et al.*, "The Silicon Vertex Detector of the Collider Detector at Fermilab', FERMILAB-PUB-94/024-E, submitted to Nucl. Instrum. Methods (1994).

[43] J. Skarha *et al.*, Proceedings IEEE 1991 Nuclear Science Symposium, Sante Fe, NM, November 1991. FERMILAB-CONF-92/111-E.

[44] F. Snider *et al.*, Nucl. Instrum. Methods Phys. Res., Sect. A **268**, 75 (1988).

[45] F. Bedeschi *et al.*, Nucl. Instrum. Methods Phys. Res., Sect. A **268**, 50 (1988).

[46] G. Ascoli *et al.*, Nucl. Instrum. Methods Phys. Res., Sect. A **268**, 33 (1988).

[47] F. DeJongh and R. Hans, "Level 1 and Level 2 Low P_T Central Muon Trigger Efficiencies for Run IA", CDF Note 1999.

[48] F. DeJongh, "Level 3 Dimuon Efficiency for Run IA", CDF Note 1984.

[49] S. Lammel, "Processing of Data from the 1992/93 Run, Part 1: Setup and Configuration of the Express–Stream 2 Production System," CDF Note 2144.

[50] CDF Collaboration, F. Abe *et al.*, "Measurement of the Antiproton-Proton Total Cross Section at $\sqrt{s} = 546$ and 1800 GeV," CDF Note 2051, to be submitted to Phys. Rev. D. The ratio of the real to imaginary part of the elastic scattering amplitude is assumed to be 0.15.

[51] D. Frei, "Multiple Scattering of Central Muons," CDF Note 1430.

[52] C. Anway-Wiese, "Offline Muon Matching Cuts," CDF Note 1986.

[53] W. M. Yao *et al.*, "Study of Improved Track Selection for b Tagging with SVX," CDF Note 2111.

[54] S. Vejcik, "A Measurement of the B Quark and Neutral B Meson Production Cross Sections in Proton-Antiproton Collisions at a Center of Mass Energy of 1.8 TeV," Ph.D. Thesis, The Johns Hopkins University, 1992.

[55] J. Marriner, "Secondary Vertex Fit with (optional) Mass Constraints and (optional) Pointing Constraints," CDF Note 1996.

[56] M. Bailey *et al.*, "Measurement of the B Meson and b Quark Cross-Sections Using the Exclusive Decays $B^- \to J/\psi\ K^-$ and $B^0 \to J/\psi\ K^*$," CDF Note 2516.

[57] R. Hans, "Polarization in $B^0 \to J/\psi\ K^*$," CDF Note 2518 and private communication.

[58] H. Wenzel, "Measurement of the Inclusive B-Lifetime Using J/ψ's at the CDF Experiment," Doktorarbeit, RWTH Aachen, Ph.D. Thesis, (1993); Phys. Rev. Lett. **71**, 3421, (1993).

[59] O. Schneider, A. Spies *et al.*, "A Measurement of the B^- and B^0 Lifetime Using Exclusive Decay Channels," CDF note 2345; FERMILAB-PUB-94/034-E, submitted to Phys. Rev. Lett. (1994).

[60] J. Hylen, private communication.

[61] R. Keup "The Momentum Scale in Run IA", CDF Note 2262.

[62] The PRL selection used a $\pm$ 80 MeV/c^2 window around the K^* mass. Studies using a Monte Carlo generated signal and combinatoric background from the data shows an increase in S^2/N from 130 to 156 if a $\pm$ 50 MeV/c^2 window is used. The Pt(B) $>$ 6 GeV/c requirement is added to the B_s^0 selection. Studies using Monte Carlo predict such a requirement is 99% efficient for signal. In the data, background is reduced by 25%.

[63] F. Bedeschi *et al.*, "Evaluation of the Resolution of the CTC and SVX," CDF Note 1939; J. Kroll, private communication.